

Molecular Motions of Water

The effect of charged and hydrophobic solutes

ISBN 978-90-77209-45-5

© 2010, Klaas-Jan Tielrooij

All rights reserved. No part of this publication may be reproduced, stored in a retrieval system or transmitted in any form or by any means, electronic, mechanical, photocopying, recording, scanning or otherwise, without the permission in writing of the author.

Cover design by Eva Janssens & Klaas-Jan Tielrooij. Front image: studies of water flow by Leonardo da Vinci, 1508-1509.

Molecular Motions of Water

The effect of charged and hydrophobic solutes

ACADEMISCH PROEFSCHRIFT

ter verkrijging van de graad van doctor
aan de Universiteit van Amsterdam
op gezag van de Rector Magnificus
prof. dr. D. C. van den Boom
ten overstaan van een door het college voor promoties
ingestelde commissie,
in het openbaar te verdedigen in de Agnietenkapel
op woensdag 15 december 2010, te 14:00 uur

door

Klaas-Jan Tielrooij

geboren te Eindhoven

PROMOTIECOMMISSIE

promotor: prof. dr. H.J. Bakker
copromotor: prof. dr. M. Bonn
overige leden: prof. dr. P.G. Bolhuis
prof. dr. D. Bonn
prof. dr. D. Frenkel
prof. dr. N. Agmon
prof. dr. L. Kuipers
dr. M.S. Pshenichnikov

Faculteit der Natuurwetenschappen, Wiskunde en Informatica

The work described in this thesis was performed at the FOM-*Institute for Atomic and Molecular Physics* (AMOLF), Science Park 104, 1098 XG Amsterdam, The Netherlands. This work is part of the research programme of the *Stichting Fundamenteel Onderzoek der Materie* (FOM), which is financially supported by the *Nederlandse Organisatie voor Wetenschappelijk Onderzoek* (NWO).

VOOR MIJN OUDERS

*Spetter, pieter, pater
Lekker in het water
Ga maar vast naar huis
Ik kom een druppel later*

(Herman van Veen)

THIS THESIS IS BASED ON THE FOLLOWING PUBLICATIONS:

- K.J. Tielrooij, M.J. Cox and H.J. Bakker: Effect of confinement on proton-transfer reactions in water nanopools.
Chem. Phys. Chem., 10:245-251 (2009). – Chapter 8
- K.J. Tielrooij, C. Petersen, Y.L.A. Rezus and H.J. Bakker: Reorientation of HDO in liquid H₂O at different temperatures: Comparison of first and second order correlation functions.
Chem. Phys. Lett., 471:71-74 (2009). – Chapter 5
- K.J. Tielrooij, R.L.A. Timmer, H.J. Bakker and M. Bonn: Structure dynamics of the proton in liquid water probed with terahertz time-domain spectroscopy.
Phys. Rev. Lett., 102:198303 (2009). – Chapter 7
- K.J. Tielrooij, D. Paparo, L. Piatkowski, H.J. Bakker and M. Bonn: Dielectric relaxation dynamics of water in model membranes probed by terahertz spectroscopy.
Biophys. J., 97:2484-2492 (2009). – Chapter 10
- K.J. Tielrooij, N. Garcia-Araez, M. Bonn and H.J. Bakker: Cooperativity in ion hydration.
Science, 328:1006-1009 (2010). – Chapter 6
- K.J. Tielrooij, J. Hunger, R. Buchner M. Bonn and H.J. Bakker: Influence of concentration and temperature on the dynamics of water in the hydrophobic hydration shell of tetramethylurea.
J. Am. Chem. Soc., 132:15671-15678 (2010). – Chapter 9
- K.J. Tielrooij, M. Bonn and H.J. Bakker: Water reorientation dynamics around ions studied with terahertz dielectric relaxation and femtosecond pump-probe spectroscopy.
To be submitted. – Chapter 6

OTHER PUBLICATIONS BY THE SAME AUTHOR:

- F.H.L. Koppens, C. Buizert, K.J. Tielrooij, I.T. Vink, K.C. Nowack, T. Meunier, L.P. Kouwenhoven and L.M.K. Vandersypen: Driven coherent oscillations of a single electron spin in a quantum dot.
Nature, 442:766-771 (2006).
- T. Meunier, K.-J. Tielrooij, I.T. Vink, F.H.L. Koppens, H.P. Tranitz, W. Wegscheider, L.P. Kouwenhoven and L.M.K. Vandersypen: High fidelity measurement of singlet-triplet state in a QD.
Phys. Stat. Sol. (b), 243:3855-3858 (2006).
- T. Meunier, I.V. Vink, L.H. Willems van Beveren, K.-J. Tielrooij, R. Hanson, F.H.L. Koppens, H.P. Tranitz, W. Wegscheider, L.P. Kouwenhoven and L.M.K. Vandersypen: Experimental signature of phonon-mediated spin relaxation.
Phys. Rev. Lett., 98:126601 (2007).
- D. Paparo, K.J. Tielrooij, H. Bakker and M. Bonn: Terahertz dielectric relaxation of biological water confined in model membranes made of lyotropic phospholipids.
Mol. Cryst. Liq. Cryst., 500:108-117 (2009).
- C. Petersen, K.-J. Tielrooij, and H.J. Bakker: Strong temperature dependence of water reorientation in hydrophobic hydration shells.
J. Chem. Phys., 130:214511 (2009).
- J.J.H. Pijpers, R. Ulbricht, K.J. Tielrooij, A. Osherov, Y. Golan, C. Delerue, G. Allan and M. Bonn: Assessment of carrier-multiplication efficiency in bulk PbSe and PbS.
Nature Phys., 5:811-814 (2009).
- R.L.A. Timmer, K.J. Tielrooij and H.J. Bakker: Vibrational Förster energy transfer between water and hydrated protons.
J. Chem. Phys., 132:194504 (2010).

CONTENTS

1	Introduction	11
1.1	Water	11
1.2	Aqueous systems	12
1.2.1	Ions in water	12
1.2.2	Protons in water	13
1.2.3	Amphiphilic molecules in water	15
1.3	Spectroscopy of water	15
1.4	Outlook	17
2	Theory: light matter interaction and reorientation	19
2.1	Electromagnetic waves	19
2.1.1	Without free charges	19
2.1.2	With free charges	22
2.2	Polarization in matter	22
2.2.1	Induced polarization	23
2.2.2	Orientational polarization	24
2.2.3	Non-linear polarization	26
2.2.4	Anisotropic polarization	31
2.3	Molecular reorientation	33
2.3.1	General	34
2.3.2	First order correlation function	35
2.3.3	Second order correlation function	36
3	Experimental techniques	37
3.1	Samples	37
3.2	Measurement techniques	38
3.2.1	Terahertz transmission spectroscopy	38
3.2.2	Infrared pump-infrared probe spectroscopy	39
3.2.3	Visible pump-infrared probe spectroscopy	41
3.2.4	Visible pump-visible probe spectroscopy	41
3.2.5	Auxiliary measurements	41
3.3	Experimental realizations	42
4	Data analysis	47
4.1	Terahertz measurements	47
4.1.1	Without calibration: using variable-thickness sample cell	47
4.1.2	With calibration: using sample and reference sample	49
4.2	Measurements in the visible and infrared	53

4.2.1	Isotropic data	53
4.2.2	Anisotropic data	56
5	Temperature dependence of water reorientation	59
5.1	Introduction	59
5.2	Experimental	61
5.3	Results and discussion	62
5.3.1	Isotropic signal	62
5.3.2	Anisotropic signal	64
5.4	Conclusion	67
6	Semi-rigid hydration and cooperativity in ion solutions	69
6.1	Introduction	69
6.2	Experiment and analysis	70
6.2.1	THz spectroscopy	70
6.2.2	fs-IR spectroscopy	73
6.3	Results	76
6.4	Semi-rigid hydration	77
6.5	Cooperativity	80
6.6	Temperature dependence	83
6.7	Conclusion and outlook	85
7	Structure and dynamics of the hydrated proton	87
7.1	Introduction	87
7.2	Experimental	88
7.3	Results and discussion	91
7.4	Discussion and conclusion	94
8	Proton transfer in water nanopools	97
8.1	Introduction	97
8.2	Experimental	98
8.3	Results	100
8.3.1	Steady-state fluorescence	100
8.3.2	Femtosecond visible pump-probe	101
8.3.3	Femtosecond midinfrared pump-probe	104
8.4	Discussion	106
8.5	Conclusion	109
9	Water dynamics in a hydrophobic hydration shell	111
9.1	Introduction	111
9.2	Experimental	113
9.3	Results and discussion	114
9.3.1	Concentration dependence	114
9.3.2	Temperature dependence	122
9.4	Conclusion	126

10 Water dynamics in DOPC lipid model membranes	127
10.1 Introduction	127
10.2 Experimental	128
10.2.1 Sample	128
10.2.2 Measurement techniques	129
10.3 Analysis	129
10.4 Results	132
10.4.1 Linear infrared spectra	132
10.4.2 Varying the hydration level	133
10.4.3 Varying the temperature	135
10.5 Discussion	136
10.5.1 Slow water	137
10.5.2 Bulk-like water	138
10.5.3 Fast water	138
10.6 Conclusion and outlook	139
Bibliography	141
Appendix: <i>When Scimon met Valery</i>	157
Summary	161
Samenvatting	165
Dankwoord/Acknowledgements	171

1 INTRODUCTION

1.1 WATER

Water molecules are among the most abundant molecules in the universe and exist of two out of the three most abundant elements: hydrogen and oxygen. Water is usually formed as a byproduct during star formation, where it immediately plays a role as coolant. On our planet, no other molecule is more abundant than water; it covers more than 70% of the earth's surface. Water is also present as vapor in the atmosphere, where it is the main contributor to the greenhouse effect, which makes the earth's average temperature significantly higher than it would be without any atmosphere. All known forms of life depend on water (the human body, for instance, consists for ~ 70 % of water). Not surprisingly, the importance of water was recognized already in the ancient worlds: water was considered one of the main classical elements by the Babylonians, the Chinese, the Japanese, the Greeks and the Romans, and in Hinduism and Buddhism. More surprising is that the role of water in biology is only recently regaining scientific appreciation, after a period where "scientists publish models of biological molecules [...] in bright colors and place them against a plain, black background" [9]: The role of water is viewed increasingly as that of an active constituent instead of that of a mere solvent.

A water molecule consists of two hydrogen atoms and one oxygen atom, forming H_2O . This molecule contains two covalent OH bonds that take up two of the four sp^3 hybridized electron pairs. This leaves two lone pairs that can take part in hydrogen bonds between the oxygen atom of one water molecule and the hydrogen atom(s) of one or two neighboring molecules, in the case of pure water. In water, the hydrogen bond strength is weaker than the covalent bond strength: the hydrogen bond strength is about 12 kJ/mol, while the thermal energy is about 4 kJ/mol at room temperature. In Fig. 1.1, we illustrate the dipole moment of a water molecule, which results from its v-shape, and show the typical tetrahedral hydrogen bonding of a water molecule with its neighbors. The ability of water to form up to four hydrogen bonds per water molecule explains many of the 67 presently known anomalies of water [33]. Some of these anomalies are commonly encountered, such as the lower density of ice compared to liquid water, which makes ice float on water. Hydrogen bonding thus lies at the heart of the complex and rich physical and chemical properties of water that occur despite the simple molecular composition of water. One important property of water is its ability to break and form hydrogen bonds very rapidly, leading to continuous rearrangements of the liquid. This

is associated with water reorientation, which occurs on picosecond (ps) time scales and is the main subject of this thesis. Moreover, since water reorientation depends on the direct environment of a water molecule, e.g. through Coulombic interactions and hydrogen bonding, the reorientation dynamics are an excellent probe for elucidating the effect of different solutes on water.

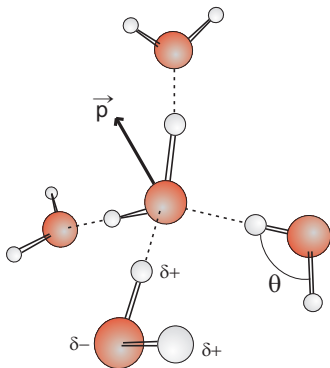


FIGURE 1.1. A water molecule with its dipole moment \vec{p} , surrounded by four hydrogen-bonded water molecules. The dipole moment and hydrogen bonds (dashed lines) arise due to the different partial charges δ^+ and δ^- on the H-atoms and the O-atoms. The H-O-H angle of a water molecule is $\theta \approx 104^\circ$.

1.2 AQUEOUS SYSTEMS

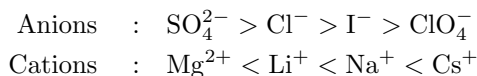
Despite its omnipresence, water rarely occurs in its pure form. About 97% of the earth's water consists of oceans, i.e. seawater that contains about 0.5 mol/kg of the ions sodium and chloride (Na^+ and Cl^-), and about ten times less magnesium and sulfate (Mg^{2+} and SO_4^{2-}). The same is true in biology: the cell's cytoplasm contains up to 0.4 mol/kg of macromolecules, such as proteins, which thereby occupy 5-40% of the total volume [42]. The interplay between water and species that are commonly found in its environment is therefore of great interest. We highlight three examples of aqueous systems that are of particular relevance for this thesis, namely (i) ions, (ii) protons and (iii) amphiphiles in water.

1.2.1 IONS IN WATER

Due to its polar nature, water is an excellent solvent for ions. Around ions, water molecules tend to orient their dipoles such that they screen the electric field of the ions. This way, water molecules prevent the long-range attraction between positive ions (cations) and negative ions (anions), which enhances the

solubility [9].

Besides seawater, there are many more systems where the interaction between ions and water plays a role, for instance in atmospheric aerosols (small particles in the atmosphere, made up of liquid and/or solids). Moreover, ions play an important role in biology, e.g. for signal transduction and controlling the cell volume. Furthermore, electrolyte solutions of ions in water can serve as a model system for large polyelectrolyte biomolecules, such as DNA and proteins. Finally, it is known that adding certain ions to solutions of biomolecules can significantly change the properties of these solutions. For example, the solubility of proteins depends strongly on the ions that are present in the solution. This effect is highly ion-specific and the origin of the Hofmeister series, which dates back to the late 19th century [57, 78]. An (incomplete) ordering of the strength of the effect of ions on a biomolecular solution, is given as:



Here, ions on the left are typically strongly hydrated, whereas ions on the right are typically weakly hydrated. Here, the degree of hydration indicates the extent to which water molecules around these ions are affected in their structure and dynamics. It turns out that strongly hydrated anions and weakly hydrated cations lead to increased surface tension, decreased hydrocarbon solubility, aggregation effects (salting out) and an increased protein stability. These ion-specific interactions are commonly encountered in many different systems. However at present they are not well understood on a molecular level [78, 101, 166]. It is especially not clear whether the effects are due to direct interactions between ions and (bio)molecular solutes or mediated through effects on the water solvent.

1.2.2 PROTONS IN WATER

Solvated protons form a special class of charged species in water, since water contains protons itself, thereby allowing for protons to be taken up by the water solvent (see Fig. 1.2). Regular ions do not form a covalent bond and only negative ions can form a hydrogen bond with a surrounding water molecule. A proton, however, can form a covalent bond with a water molecule, forming a hydronium ion H_3O^+ , and a hydrogen bond with another water molecule. This is very likely related to the anomalously high conductivity of protons in water, which is more than five times larger than the conductivity of ions of similar or smaller size than the hydronium ion [1, 16, 168]. The details of the conduction mechanism of protons are currently under extensive theoretical and experimental investigation, as mentioned in Ref. [160].

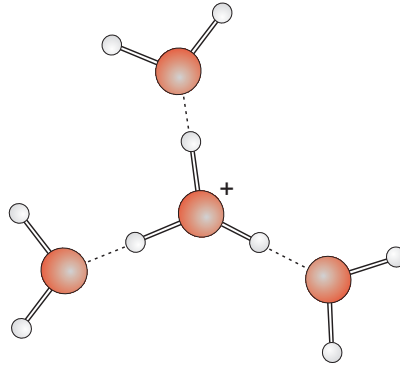


FIGURE 1.2. A proton in water, forming a hydronium ion H_3O^+ , surrounded by three hydrogen-bonded water molecules. This structure is thought to be rather planar, in contrast to the three-dimensional structure of pure water [9].

Protons in water are obviously related to all acid-base reactions that occur throughout nature. Most organisms only have a very narrow range of acidities in which they can survive, usually around a (neutral) pH of 7. However, locally, the acidity in organisms can be quite high. This is for instance the case in the mitochondria, which are organelles in eukaryotic cells that have the function to store potential energy and supply chemical energy for the cell. Mitochondria consist of an outer membrane and an inner membrane, where the intermembrane space has a much higher acidity (approaching a pH of 4) than the cytoplasm (with a pH of ~ 7.5). This creates a potential that forms the basis for energy storage. When protons are allowed to flow from the intermembrane space to the cytoplasm, presumably through proton channels, their potential energy is transferred to chemical energy stored in ATP, the cell's fuel [159].

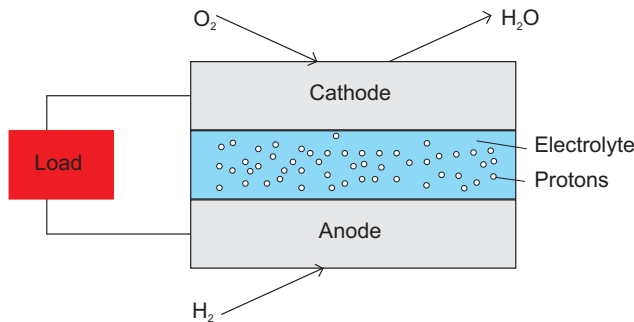


FIGURE 1.3. Schematic of the operation of a proton exchange fuel cell. The reaction at the anode is $\text{H}_2 \rightarrow 2\text{H}^+ + 2\text{e}^-$ and at the cathode: $\frac{1}{2}\text{O}_2 + 2\text{H}^+ + 2\text{e}^- \rightarrow \text{H}_2\text{O}$.

Besides in biology, protons in water also play a role in proton exchange membrane fuel cell applications. These fuel cells transform chemical energy to electrical energy through an electrochemical reaction of hydrogen and oxygen (see Fig. 1.3). Hydrogen and oxygen are used as fuel, whereas the end product is water. The operation requires protons to travel from the anode (where H_2 is split into two protons and two electrons) through an electrolyte membrane to the cathode (where H_2O is formed from the protons, the electrons and oxygen). The electrons do not pass through the electrolyte membrane and create an external electrical current.

1.2.3 AMPHIPHILIC MOLECULES IN WATER

Amphiphilic molecules are molecules that are partly polar and partly non-polar, which gives them a hydrophilic and a hydrophobic character. Such molecules give rise to the hydrophobic effect, i.e. the tendency of water and hydrophobes to segregate. This effect is the cause for interesting and ubiquitous phenomena, such as the assembly of large structures, e.g. bilayer membranes, reverse micelles and vesicles (Fig. 1.4). Furthermore, hydrophobic collapse is the cause of protein folding. However, according to a 2005 paper, "only recently have theoretical developments begun to explain and quantify many features of this phenomenon" [31].

Common amphiphiles are found in detergents and cell membranes, which consist of lipids: molecules with a hydrophilic head group and one or more hydrophobic tails, usually hydrocarbon chains. Small amphiphiles typically contain a polar group and one or more hydrocarbon groups, such as methyl groups. All proteins contain a number of hydrophobic groups, which makes hydrophobic interaction relevant to protein functioning, which is very important in biology.

1.3 SPECTROSCOPY OF WATER

Water is colorless^a and transparent, at least for visible light (wavelength between 390 and 780 nm or between 770 and 385 THz). However, electromagnetic radiation at both ends of the visible spectrum can be absorbed by water. At longer wavelengths, there are intramolecular modes, such as the OH-stretch vibration (absorbing at 3 μm or 100 THz) and the bend vibrations of water, followed by intermolecular modes, such as hydrogen-bond stretching (which absorbs at 55 μm or 5.4 THz) and hydrogen-bond bending. At even longer wavelengths, there are rotational motions (with a dielectric loss peak centered

^aDue to a number of vibrational overtones and combination bands that occur in the red part of the visible spectrum and due to increased scattering of blue light compared to red light, water has a very slight blue color [22].

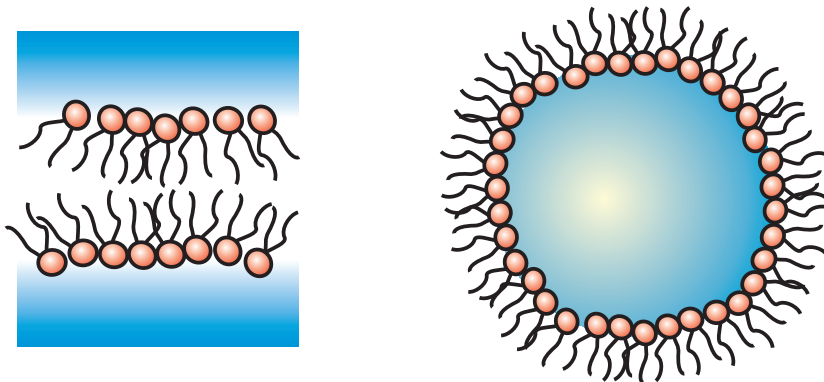


FIGURE 1.4. The left figure shows a lipid bilayer membrane; the right figure shows a reverse micelle.

at 15 mm or 20 GHz). At the other end of the visible spectrum, i.e. at shorter wavelengths, electronic transitions and ionization processes (e.g. photodissociation at 125 nm or 2400 THz) are present. Figure 1.5 shows these types of dynamics and how they fit into the general spectrum of electromagnetic radiation.

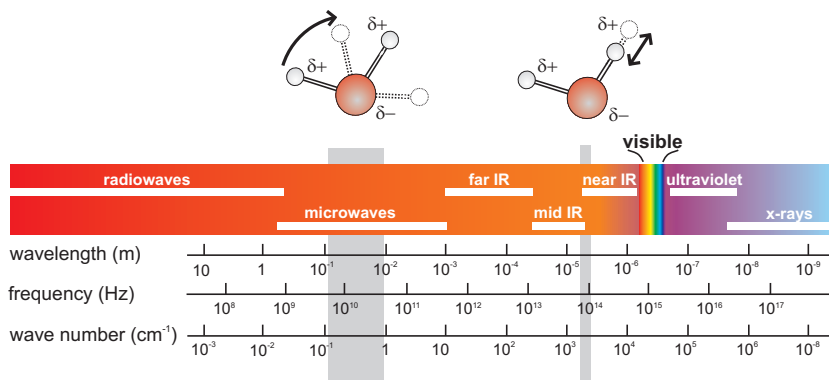


FIGURE 1.5. The electromagnetic spectrum with the reorientation of water molecules in the microwave range and the intramolecular stretch mode of water in the mid-infrared region.

In this thesis, we are interested in the molecular processes that occur in aqueous solutions. We specifically study the picosecond reorientation dynamics of water molecules in different environments, which we monitor in two ways. First of all, we study the optical properties of aqueous solutions in the THz range, where we are directly sensitive to water reorientation. This is done with a THz time-domain transmission setup, where THz pulses are created

and the time-dependent electric field of these pulses is detected. From these measurements we obtain the complex dielectric function, whose frequency dependence is determined by the reorientation dynamics of water. Secondly, we vibrationally tag water molecules, whose reorientation can then be followed directly in time. This is done by performing pump-probe spectroscopy, where the pump and probe pulses are resonant with the intramolecular stretch vibration of water molecules in the sample. Due to the polarization of the pump pulse, an anisotropic distribution of excited molecules is created. As a result of reorientation, this distribution becomes isotropic, which occurs with a time scale that represents the reorientation dynamics. Given the short time scales at which the reorientation of water takes place, our experiments require very short pulses, typically with a duration of ~ 100 femtoseconds (fs), positioning our experiments in the category of ultrafast spectroscopy.

1.4 OUTLOOK

This thesis discusses measurements on the ultrafast dynamics of aqueous solutions. Chapter 2 gives a theoretical basis for light-matter interactions and molecular reorientation. The concepts of light-matter interactions lie at the basis of Chapter 3, where the spectroscopic experiments that were performed are described. Chapter 4 subsequently discusses how the experimental results are analyzed and connected to the physics and chemistry of the systems under study. The rest of the thesis deals with the measurements on different aqueous solutions. In Chapter 5, we study energy relaxation and water reorientation of neat water. In Chapter 6, we examine different solvated ions and their effect on water dynamics. Then, the dynamical properties of hydrated protons are examined (Chapter 7), followed by proton transfer in water nanopools (Chapter 8). Finally, chapters 9 and 10 are concerned with two directly biologically relevant systems: a partly hydrophobic molecule in water and a model membrane, respectively.

2 THEORY: LIGHT MATTER INTERACTION AND REORIENTATION

In this chapter we describe the theoretical concepts that lie at the basis of the experimental techniques that are used, and the physical phenomena that are studied in this thesis. Starting with how electromagnetic waves interact with matter and free charges, we turn to different polarizations in matter: induced and orientational polarizations that lead to resonance and relaxation phenomena, respectively; and nonlinear and anisotropic polarizations. This chapter finishes with a theoretical description of angular diffusion of molecules and the experimental probing of these dynamics.

2.1 ELECTROMAGNETIC WAVES

This thesis deals with systems (aqueous solutions) that are studied with spectroscopic techniques. In order to understand the outcome of a spectroscopic measurement and to relate it to physical properties of the system under study, one needs to first understand how light interacts with the system. We will therefore discuss how electromagnetic waves travel through a medium without free charges, followed by a medium with free charges.

2.1.1 WITHOUT FREE CHARGES

Light can be described as an electromagnetic (EM) wave, which obeys Maxwell's equations

$$\begin{aligned} \text{(a)} \quad \vec{\nabla} \cdot \vec{D} &= 0 & \text{(c)} \quad \vec{\nabla} \times \vec{E} + \frac{\partial \vec{B}}{\partial t} &= 0 & \text{(2.1)} \\ \text{(b)} \quad \vec{\nabla} \cdot \vec{B} &= 0 & \text{(d)} \quad \vec{\nabla} \times \frac{\vec{B}}{\mu_0} - \frac{\partial \vec{D}}{\partial t} &= 0 \end{aligned}$$

These equations hold for any nonmagnetic medium without free charges. Here \vec{E} is the electric field, \vec{B} the magnetic field, \vec{D} the dielectric displacement and

μ_0 the vacuum permeability. Furthermore $\vec{\nabla} \cdot \vec{f}$ takes the divergence of \vec{f} and $\vec{\nabla} \times \vec{f}$ takes the curl of \vec{f} .

The dielectric displacement $\vec{D} = \epsilon_0 \hat{\epsilon}$, with ϵ_0 the vacuum permittivity and $\hat{\epsilon}$ the complex permittivity, takes into account the electric field that is generated by a polarization \vec{P} . This polarization arises since bound charges of opposite sign experience a force in opposite direction, under the influence of an electric field. In neutral atoms this will lead to slight displacements of the charges (the electrons and nuclei) and hence induced dipoles; in molecules with a permanent dipole, this will lead to rotations of the molecules that will align their dipoles with the electric field.

By taking the curl of Eq. 2.1c and substituting Eqs. 2.1a and 2.1d, it follows for the electric field that

$$\nabla^2 \vec{E}(\vec{r}, t) = \mu_0 \epsilon_0 \frac{\partial^2 \hat{\epsilon} \vec{E}(\vec{r}, t)}{\partial t^2} , \quad (2.2)$$

which is called the wave equation. Here $\vec{r} = (\vec{x}, \vec{y}, \vec{z})$ is the space coordinate and t is time. We will solve this equation in the Fourier domain with wave vector \vec{k} and angular frequency ω , instead of \vec{r} and t . The Fourier transform \mathcal{F} of a function $f(\vec{r}, t)$ is^a

$$F(\vec{k}, \omega) = \mathcal{F}(f(\vec{r}, t)) = \int_{-\infty}^{\infty} \int_{-\infty}^{\infty} f(\vec{r}, t) e^{i(\vec{k} \cdot \vec{r} - \omega t)} d\vec{r} dt . \quad (2.3)$$

The dielectric displacement \vec{D} and polarization \vec{P} are related by

$$\vec{D}(\omega) = \epsilon_0 \vec{E}(\omega) + \vec{P}(\omega) = \epsilon_0 \hat{\epsilon}(\omega) \vec{E}(\omega) , \quad (2.4)$$

where, $\hat{\epsilon} = \epsilon' - i\epsilon''$ is the complex permittivity, which relates the polarization \vec{P} to the applied electric field \vec{E} . This equation holds for linear, isotropic media; the case of non-linear media is discussed in Section 2.2.3 and the case of anisotropic media, where the permittivity becomes a tensor, is discussed in Section 2.2.4. Taking the Fourier transform on both sides of the wave equation (Eq. 2.2) leads to the dispersion relation for the wave vector

$$k(\omega) = \sqrt{\omega^2 \mu_0 \epsilon_0 \hat{\epsilon}(\omega)} . \quad (2.5)$$

A general solution to the wave equation for the electric field is

^aThe Fourier transform can be defined alternatively with opposite sign of the exponent, which would change the sign of the imaginary part of the complex refractive index and dielectric function.

$$E(\vec{r}, t) = \int_{-\infty}^{\infty} E_0(\omega) e^{i(\omega t - \vec{k}(\omega) \cdot \vec{r})} d\omega , \quad (2.6)$$

where \vec{k} points in the direction of wave propagation and obeys the dispersion relation of Eq. 2.5 and the frequency components are given by

$$E_0(\omega) = \int_{-\infty}^{\infty} E(\vec{r} = \vec{0}, t) e^{-i\omega t} dt . \quad (2.7)$$

Compared to EM waves in vacuum, light passing through a medium travels with a different speed (refraction) and can be attenuated (absorption). The effect of attenuation comes from the imaginary part of the complex refractive index, which is connected to the complex dielectric permittivity through

$$\hat{n}(\omega) \equiv n(\omega) - i\kappa(\omega) \equiv \frac{|\vec{k}(\omega)|c}{\omega} = \frac{\sqrt{\epsilon_0 \hat{\epsilon}(\omega) \mu_0}}{\sqrt{\epsilon_0 \mu_0}} = \sqrt{\hat{\epsilon}(\omega)} . \quad (2.8)$$

Here, n is the refractive index and κ the extinction coefficient. Using the complex refractive index \hat{n} , the EM wave in the x -direction can be rewritten as

$$E(x, t) = \int_{-\infty}^{\infty} E_0(\omega) e^{i\omega(t - \hat{n}x/c)} d\omega = \int_{-\infty}^{\infty} E_0(\omega) e^{i\omega(t - nx/c)} \cdot e^{-\omega\kappa x/c} d\omega . \quad (2.9)$$

Clearly, the imaginary part of the complex refractive index leads to an exponential decay of the amplitude of the EM wave. By substituting $\alpha(\omega) \equiv 2\kappa(\omega)\omega/c$, with $\alpha(\omega)$ the frequency-dependent absorption coefficient, Eq. 2.9 yields the Lambert-Beer law

$$\frac{I}{I_0} = \frac{E(x, t)E^*(x, t)}{E(x=0, t)E^*(x=0, t)} = \int_{-\infty}^{\infty} e^{-2\omega\kappa(\omega)x/c} d\omega = \int_{-\infty}^{\infty} e^{-\alpha(\omega)x} d\omega . \quad (2.10)$$

Here I is the intensity of the EM wave after a sample and I_0 the intensity before the sample. Measuring these macroscopic intensities - or better, the EM waves $\vec{E}(\vec{r}, t)$ itself before and after the sample - provides information on how the sample affects the wave through $\hat{n}(\omega)$ or equivalently $\hat{\epsilon}(\omega)$. The latter can then be related to the polarization in the sample, which arises from microscopic processes. In Section 2.2, we will have a closer look at the different origins of the frequency dependence of the polarization in the system and the implications for the propagated EM waves.

2.1.2 WITH FREE CHARGES

In many systems, not only bound charges, but also free charges, such as free electrons or ions, are present. These charges lead to a conductivity term σ that needs to be included as a source in the Maxwell equations

$$\begin{aligned}
 \text{(a)} \quad \vec{\nabla} \cdot \vec{D} &= 0 & \text{(c)} \quad \vec{\nabla} \times \vec{E} + \frac{\partial \vec{B}}{\partial t} &= 0 \\
 \text{(b)} \quad \vec{\nabla} \cdot \vec{B} &= 0 & \text{(d)} \quad \vec{\nabla} \times \frac{\vec{B}}{\mu_0} - \frac{\partial \vec{D}}{\partial t} &= \mu_0 \sigma \vec{E} .
 \end{aligned}
 \tag{2.11}$$

These Maxwell equations, which hold for any non-magnetic medium with free charges, lead to EM waves that obey the following dispersion relation

$$\vec{k}(\omega) = \sqrt{\omega^2 \mu_0 \epsilon_0 \hat{\epsilon}(\omega) - i \omega \mu_0 \sigma} , \tag{2.12}$$

This dispersion relation differs from the result for a medium without free charges (Eq. 2.5) by the substitution

$$\hat{\epsilon} \rightarrow \hat{\epsilon} + \frac{\sigma}{i \omega \epsilon_0} . \tag{2.13}$$

This means that the imaginary part of the dielectric function ϵ'' contains an extra conductivity term $\sigma/(\omega \epsilon_0)$, which leads to an increase in the absorption of a sample due to the presence of free charges, which take energy from the field of the EM wave.

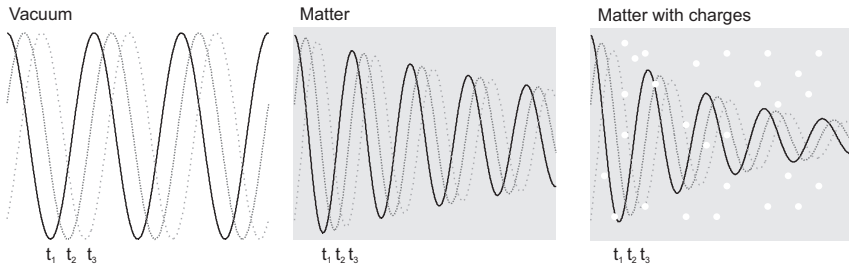


FIGURE 2.1. Linearly polarized, monochromatic plane waves at three different times, as they travel trough vacuum, matter without and matter with free charges.

2.2 POLARIZATION IN MATTER

In the previous section, the polarization \vec{P} that originates from microscopic processes in the system, was linked to the complex dielectric function $\hat{\epsilon}$ through:

$\vec{P} = \epsilon_0(\hat{\epsilon}(\omega) - 1)\vec{E}$. We saw that the complex dielectric function, which can be experimentally determined using techniques as will be described in Chapter 3, describes how an EM wave propagates through a system. In this section, we will discuss the microscopic processes that give rise to the polarization and how the frequency dependence of the dielectric function can provide information on these microscopic processes.

In two limiting cases, the motions of charges in a system can be described as *resonance* or *relaxation* processes, corresponding to *induced* polarization \vec{P}_{ind} and *orientational* polarization \vec{P}_{μ} , respectively. After discussing these two microscopic processes that give rise to polarizations, we discuss non-linear polarization and polarizations in anisotropic media. These types of polarizations are of great importance for the experimental methods that this thesis is based on.

2.2.1 INDUCED POLARIZATION

To calculate the frequency-dependent dielectric properties associated with the induced polarization, we consider a charge in a harmonic potential that restores the motion of the charge, and include a damping term, which originates from interaction of the system with the environment. The displacement \vec{r} of N particles with charge q , due to an electric field $\vec{E}(t)$, leads to an induced polarization $\vec{P}_{\text{ind}} = -Nq\vec{r}$. Newton's second law of motion then gives

$$\frac{d^2\vec{r}}{dt^2} + \gamma\frac{d\vec{r}}{dt} + \frac{C\vec{r}}{m} = -\frac{q}{m}\vec{E}(t) \quad , \quad (2.14)$$

where γ is the damping constant and C the binding constant of the harmonic potential and m is the particle's mass. Solving this equation for \vec{r} in the Fourier domain yields

$$\vec{P}_{\text{ind}}(\omega) = -Nq\vec{r} = \frac{Nq^2\vec{E}(\omega)}{m(\omega_0^2 - \omega^2 + i\gamma\omega)} = \epsilon_0(\hat{\epsilon}(\omega) - \epsilon_{\infty})\vec{E}(\omega) \quad . \quad (2.15)$$

Here, we have defined the natural frequency $\omega_0 = \sqrt{\frac{C}{m}}$, which is the angular frequency that is associated with the energy of a transition between two states in the harmonic potential. A weaker restoring force (smaller C) means a more shallow harmonic potential and a lower frequency ω , which means that light of lower photon energy is required to drive the oscillator. Eq. 2.15 yields the complex frequency-dependent permittivity of the system as a result of the induced polarization (see Fig. 2.2)

$$\hat{\epsilon}(\omega) = \frac{(\epsilon_s - \epsilon_{\infty})\omega_0^2}{(\omega_0^2 - \omega^2 + i\gamma\omega)} + \epsilon_{\infty} \quad , \quad (2.16)$$

where we have used $\epsilon_s = \lim_{\omega \rightarrow 0} \hat{\epsilon}$ and $\epsilon_\infty = \lim_{\omega \rightarrow \infty} \hat{\epsilon}$. The term $(\epsilon_s - \epsilon_\infty)\omega_0^2$ defines the cross section of the mode. The damping constant γ determines the width of the resonance. An example of a mode that leads to induced polarization is the OH-stretch mode of a water molecule, where the H-atom is displaced with respect to the O-atom. The restoring force is determined by the strength of the covalent OH bond.

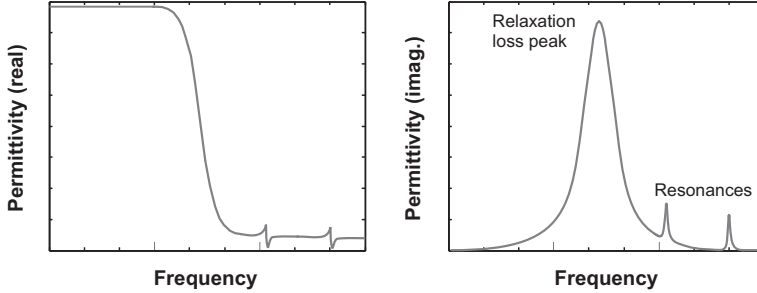


FIGURE 2.2. The real and imaginary part of the complex permittivity $\hat{\epsilon}$ as a function of frequency, for a system with one relaxation mode obeying Eq. 2.20 and two resonance modes that both obey Eq. 2.16.

2.2.2 ORIENTATIONAL POLARIZATION

Orientalional polarization is usually associated with the reorientation of permanent dipoles in a system, such as the permanent dipoles of water molecules, which leads to a relaxation mode. The static polarization as a result of the reorientation of permanent dipoles driven by an electric field is given by

$$\vec{P}_{\mu,s} \propto \epsilon_0 \rho \langle \vec{\mu} \rangle \approx \epsilon_0 \rho \frac{\mu^2}{3k_B T} \vec{E} , \quad (2.17)$$

where, ρ is the dipole density, $\langle \vec{\mu} \rangle$ is the value of the permanent dipole vector $\vec{\mu}$ averaged over all orientations, k_B is the Boltzmann constant and T the temperature. The proportionality comes from the fact that the molecular dipole experiences a field different from the applied field \vec{E} , which is called the local field effect. The approximation comes from considering the average orientation of a dipole, under the influence of a directing field \vec{E} , weighted according to Boltzmann's law, and holds for the limit $\vec{\mu} \cdot \vec{E} \ll k_B T$, i.e. where the electric field energy is smaller than the thermal energy. In the case of large electric fields, polarization terms that are of higher order in \vec{E} can appear (see Section 2.2.3).

By driving the system with an oscillating electric field, it is possible to determine the frequency dependence of the orientation polarization. If the frequency of the directing field is low, the dipoles orient in phase with the field. However at higher frequencies, the dipoles start lagging behind (see Fig. 2.3). Assuming no history dependence of the orientational polarization, \vec{P}_μ follows a first order differential equation

$$\frac{d\vec{P}_\mu}{dt} = -\frac{1}{\tau_{\text{reor}}}\vec{P}_\mu(t) , \quad (2.18)$$

where, τ_{reor} is a time constant that indicates how fast the permanent dipoles respond to a step in the electric field (see Fig. 2.3). Fourier transforming Eq. 2.18 and rearrangement yields

$$\vec{P}_\mu(\omega) = \frac{\vec{P}_{\mu,s}}{1 + i\omega\tau_{\text{reor}}} , \quad (2.19)$$

where $\vec{P}_{\mu,s}$ is the static orientational polarization ($\lim_{\omega \rightarrow 0} \vec{P}_\mu$). The frequency-dependent orientation polarization $\vec{P}_\mu(\omega)$ leads to the dielectric relaxation equation (see Fig. 2.2)

$$\hat{\epsilon}(\omega) = \frac{\epsilon_s - \epsilon_\infty}{1 + i\omega\tau_{\text{reor}}} + \epsilon_\infty , \quad (2.20)$$

where, ϵ_s is the static permittivity of a sample and ϵ_∞ is the high frequency limit or unrelaxed permittivity ($\lim_{\omega \rightarrow \infty} \hat{\epsilon}$). The dielectric strength is given by $S = \epsilon_s - \epsilon_\infty$. Eq. 2.20 can also be seen as the limit of Eq. 2.16, where $\gamma/\omega_0 \gg \omega/\omega_0$, i.e. the case where the damping rate is much larger than the restoring rate and the frequency is not too high.

Since the frequency-dependent dielectric function $\hat{\epsilon}(\omega)$ can be determined experimentally, Eq. 2.20 makes it possible to determine a microscopic property of the sample: the reorientation time constant τ_{reor} . If a system has more than one reorientation time, each time is associated with a similar term as the first one in Eq. 2.20. The reorientation of water dipoles in a bulk water sample exhibits two relaxation processes and hence the dielectric function reads [46, 68, 138–140, 186]

$$\hat{\epsilon}(\omega) = \frac{S_1}{1 + i\omega\tau_D} + \frac{S_2}{1 + i\omega\tau_2} + \epsilon_\infty . \quad (2.21)$$

Here, the time constant τ_D is known as the Debye time, which is about 8 ps. The second process has a much smaller relaxation strength and a time constant of 250 fs, which corresponds to THz frequencies. Adding species such as ions

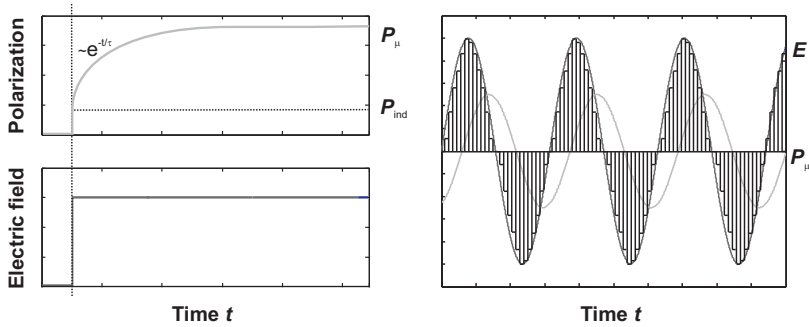


FIGURE 2.3. The left figure show the polarization response to a step in the electric field, where the *induced* polarization follows the field more rapidly than the *orientational* polarization, which grows in with a delay. For an oscillating electric field, this yields a polarization that lags behind with respect to the electric field, as shown in the right figure.

or amphiphiles to water might result in additional reorientation time scales and hence additional relaxation terms. Furthermore, it is possible that certain water molecules no longer respond to an external electric field, e.g. due to the interaction with the electric field of an ion. This leads to a smaller orientational polarization and is hence called depolarization.

2.2.3 NON-LINEAR POLARIZATION

GENERAL In the beginning of this chapter, we introduced the polarization, which was taken to be proportional to the electric field, $\vec{P} = \epsilon_0(\hat{\epsilon} - 1)\vec{E}$ or $\vec{P} = \epsilon_0\chi\vec{E}$, using the susceptibility χ . It is however possible that the polarization is no longer linear with the electric field, which is most apparent for strong electric fields (for instance when the approximation in Eq. 2.17 is no longer valid). The polarization can then be expanded into

$$\vec{P}(\omega) = \epsilon_0(\chi\vec{E}(\omega) + \chi^{(2)}\vec{E}\vec{E}(\omega) + \chi^{(3)}\vec{E}\vec{E}\vec{E}(\omega) + \dots) , \quad (2.22)$$

where $\chi^{(2)}$ and $\chi^{(3)}$ are the second- and third-order susceptibility. The polarization now consists of a linear component that scales with χ and a non-linear component \vec{P}^{NL} that contains higher order susceptibilities. \vec{P}^{NL} can be a source for new EM fields at different frequencies. To determine what kind of electromagnetic waves occur due to higher order polarizations \vec{P}^{NL} , the Maxwell equations from Eq. 2.1 are used with the following dielectric displacement: $\vec{D} = \epsilon_0\vec{E} + \epsilon_0\hat{\epsilon}\vec{E} + \vec{P}^{NL}$. This gives

$$\begin{aligned}
 \text{(a)} \quad \vec{\nabla} \cdot \vec{D} &= 0 & \text{(c)} \quad \vec{\nabla} \times \vec{E} + \frac{\partial \vec{B}}{\partial t} &= 0 & (2.23) \\
 \text{(b)} \quad \vec{\nabla} \cdot \vec{B} &= 0 & \text{(d)} \quad \vec{\nabla} \times \vec{B} - \mu_0 \epsilon_0 \frac{\partial \hat{\epsilon} \vec{E}}{\partial t} &= \frac{\partial \vec{P}^{\text{NL}}}{\partial t} .
 \end{aligned}$$

The addition of the source term in Eq. 2.23d leads to the wave equation

$$\nabla^2 \vec{E} - \mu_0 \epsilon_0 \frac{\partial^2 \hat{\epsilon} \vec{E}}{\partial t^2} = \mu_0 \frac{\partial^2 \vec{P}^{\text{NL}}}{\partial t^2} . \quad (2.24)$$

From this equation it is clear that the higher order polarization terms P^{NL} are source terms that lead to the creation of electromagnetic waves. These waves will have a certain frequency ω_s and wavevector \vec{k}_s . To determine which frequencies are created, consider an electric field from two waves \vec{E}_1 and \vec{E}_2

$$\vec{E} = \vec{E}_1 + \vec{E}_2 = \vec{E}_{1,0}(t) e^{i(\omega_1 t - \vec{k}_1 \cdot \vec{r})} + \vec{E}_{2,0}(t) e^{i(\omega_2 t - \vec{k}_2 \cdot \vec{r})} + \text{c.c.} , \quad (2.25)$$

where c.c. means complex conjugate. The two EM waves are allowed to have time-dependent amplitudes, to make the treatment applicable to continuous wave and to pulsed cases. In the latter case, the slowly varying envelope approximation (SVEA) is required, which states that the optical period must be shorter than the pulse duration. If the electromagnetic wave \vec{E} travels through a medium with a nonzero $\chi^{(2)}$ (only in non-centrosymmetric media), the second term of Eq. 2.22 yields the second order polarization with all combinations of the incoming frequencies $\omega_s = \pm\omega_1 \pm \omega_2$ and wavevectors $\vec{k}_s = \pm\vec{k}_1 \pm \vec{k}_2$

$$\begin{aligned}
 \vec{P}^{(2)} &= \chi^{(2)} \vec{E} \vec{E} & (2.26) \\
 &= \chi^{(2)} (\vec{P}(\omega_s = 0)) & \text{(OR)} \\
 &+ \vec{P}(\omega_s = 2\omega_1) & \text{(SHG)} \\
 &+ \vec{P}(\omega_s = 2\omega_2) & \text{(SHG)} \\
 &+ 2\vec{P}(\omega_s = \omega_1 + \omega_2) & \text{(SFG)} \\
 &+ 2\vec{P}(\omega_s = \omega_1 - \omega_2) & \text{(DFG)} .
 \end{aligned}$$

The second order polarization contains terms with different frequencies, leading to newly created EM waves with the following frequencies: $\omega = 0$ (OR, optical rectification); $2\omega_1$ and $2\omega_2$ (SHG, second harmonic generation); $\omega_1 + \omega_2$ (SFG, sum frequency generation); and $\omega_1 - \omega_2$ (DFG, difference frequency generation), as shown in Fig. 2.4.

ANISOTROPIC MEDIA AND PHASE MATCHING Of the different waves in Eq. 2.26, only the ones for which the phase-matching condition is met, are created efficiently. The phase-matching condition for a sum-frequency process,

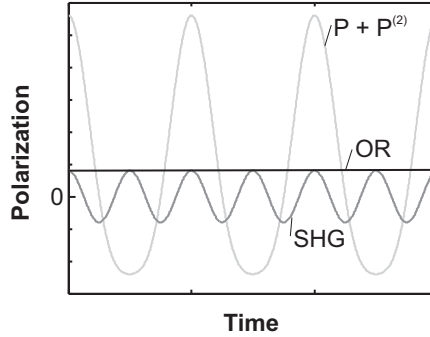


FIGURE 2.4. The polarization response to an oscillating electric field, in the case of second order non-linear polarization and $\omega_1 = \omega_2$.

for instance, reads $\vec{k}_s = \vec{k}_1 + \vec{k}_2$. When this condition is met, the created wave $\vec{E}_s(\vec{k}_s, \omega_s)$ maintains a fixed phase relation with respect to the non-linear polarization and energy can flow most efficiently to the created wave from the incident waves $\vec{E}_1(\vec{k}_1, \omega_1)$ and $\vec{E}_2(\vec{k}_2, \omega_2)$, which have a fixed phase relation with respect to the non-linear polarization. This condition is usually not met, since EM waves with different frequencies typically experience different refractive indices (due to relaxations and resonances in the medium). However, there are special nonlinear crystals that have a non-zero higher order susceptibility and that show (uniaxial) birefringence. A uniaxial birefringent crystal is a special case of an anisotropic medium. In an anisotropic medium, the susceptibility χ (and thus the permittivity and the refractive index) is a second rank tensor that describes the polarizations in the x , y or z -direction that arise due to the electric fields in the x , y and z -direction

$$[P_x, P_y, P_z] = \epsilon_0 \chi_{ij} [E_x, E_y, E_z] . \quad (2.27)$$

It is typically possible to define a coordinate system, the principal axis system, for which the susceptibility tensor is diagonal, containing only the terms χ_{xx} , χ_{yy} and χ_{zz} . In the case of a uniaxial crystal, $\chi_{xx} = \chi_{yy}$. This means that a uniaxial birefringent crystal has two distinct susceptibilities, or equivalently refractive indices n_o and n_e along different axes of the crystal. Hence, in a certain direction, it is possible to tune the refractive index that light experiences between n_o and n_e by tuning the crystal orientation. If the incident waves with \vec{E}_1 and \vec{E}_2 are polarized in a different direction than the created wave \vec{E}_s , the refractive indices of these waves can be tuned such that phase-matching between incoming and created waves is achieved. This method is used in many of the nonlinear optical conversion steps that will be described in Chapter 3.

NON-RESONANT $\chi^{(2)}$: THZ CREATION The creation of a THz pulse in a ZnTe nonlinear crystal is an example of a non-resonant $\chi^{(2)}$ process. Here, non-resonant (also called non-dispersive) means that the incident and outgoing waves are not resonant with a transition in the medium (corresponding to a negligible frequency dependence of the refractive index). To create THz radiation, a pump pulse with light of frequency ω_p is incident on a ZnTe crystal

$$\vec{E}_p(\vec{r}, t) = \vec{E}_0(t)e^{i(\omega_p t - \vec{k}_p \cdot \vec{r})} + \text{c.c.} \quad (2.28)$$

Here, the amplitude $\vec{E}_0(t)$ describes a pulse with a certain ultrashort duration, which means that \vec{E}_p contains a bandwidth of frequencies, centered at ω_p . It is now possible that difference frequency mixing occurs of different frequencies within the bandwidth of the pump pulse, e.g. $\omega_{p,i}$ and $\omega_{p,j}$. This leads to a second order optical rectification polarization term (assuming no dispersion for $\chi^{(2)}$ around frequency $\omega_{p,i} - \omega_{p,j}$)

$$P_{\text{OR}}^{(2)}(t) = \chi^{(2)}(\omega_{p,i} - \omega_{p,j})|E_p(t)|^2. \quad (2.29)$$

By using light with $\omega_p = 800$ nm and a pulse duration of 150 fs, the second order polarization $\vec{P}_{\text{OR}}^{(2)}$ leads in the far field to an EM pulse E_{THz} with THz frequencies and a time profile that is the second time derivative of $\vec{P}_{\text{OR}}^{(2)}$ (see Fig 2.5). Many experiments described in this thesis were done using THz pulses, created as described above.

RESONANT $\chi^{(3)}$: PUMP-PROBE SPECTROSCOPY Another important type of experiment used throughout this thesis is pump-probe spectroscopy, which can be described as a case of a resonant $\chi^{(3)}$ process. In this case, the pulses are resonant with a transition in the medium. This allows for the creation of a population in an excited state (and an associated polarization) with - in our systems - a longer lifetime than the duration of the incoming pulses, in contrast to a non-resonant polarization that only occurs during the temporal overlap of the incoming pulses. The excited state lifetime can be a typical subject of interest in pump-probe spectroscopy. In a pump-probe experiment, there are two pulses, the pump and probe pulse, and the pump-induced change in absorption $\Delta\alpha$ of a sample is monitored. This is done by measuring the probe absorption in the absence and the presence of the pump pulse.

Consider an electric field that contains two pulses with slowly varying amplitudes: the pump pulse \vec{E}_{pump} and the probe pulse \vec{E}_{probe} , where the latter is delayed with respect to the former by a delay time τ

$$\vec{E}(\vec{r}, t) = \vec{E}_{\text{pump},0}(t + \tau)e^{i(\omega_1 t - \vec{k}_1 \cdot \vec{r})} + \vec{E}_{\text{probe},0}(t)e^{i(\omega_2 t - \vec{k}_2 \cdot \vec{r})} + \text{c.c.} \quad (2.30)$$

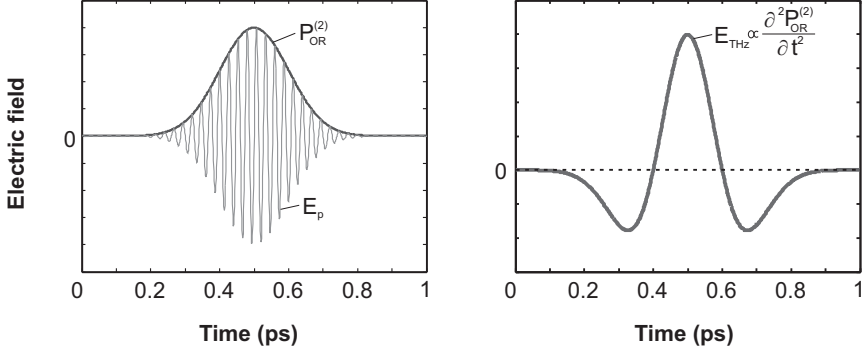


FIGURE 2.5. The left figure shows the electric field of a pulse of 800 nm light with the pulse envelope, which has the same shape as the second order polarization created through optical rectification $P_{OR}^{(2)}$. This polarization creates dipole radiation, whose electric field in the far field is a single-cycle THz pulse E_{THz} , shown in the right figure.

These pulses will give rise to a radiated field \vec{E}_{rad} , which is proportional to the third-order polarization and which can have the same wave vector as the probe pulse: $\vec{k}_s = \vec{k}_1 - \vec{k}_1 + \vec{k}_2 = \vec{k}_2$, if there are two conjugated field interactions with the pump pulse and one field interaction with the probe pulse. The radiated field from the third order polarization can interfere with the (linear) probe pulse \vec{E}_{probe} (sometimes referred to as the local oscillator), which also has wave vector \vec{k}_2 . Constructive interference corresponds to a negative induced absorption (bleaching) and destructive interference to a positive induced absorption, as measured in the direction of the probe pulse (self-heterodyned detection).

In our experiments, we measure the pump-induced difference in absorption $\Delta\alpha(\omega)$ of the sample under study, by measuring in the direction of the probe light. The pump-induced absorption change is

$$\begin{aligned} \Delta\alpha(\omega, \tau) &\equiv 1 - \frac{I(\omega, \tau)}{I_0(\omega)} = 1 - \frac{|\vec{E}_{probe}(\omega) + \vec{E}_{rad}(\omega, \tau)|^2}{|\vec{E}_{probe}(\omega)|^2} \quad (2.31) \\ &\propto \frac{Im\{\vec{E}_{probe}(\omega)\vec{P}^{(3)}(\omega, \tau)\}}{|\vec{E}_{probe}(\omega)|^2}, \end{aligned}$$

where the imaginary part comes from the fact that we are interested in absorption (rather than refraction), which is given by the imaginary part of the refractive index (see Eq. 2.10) and hence by the imaginary part of $\chi^{(3)}$, with which the polarization $\vec{P}^{(3)}$ scales. The third order polarization $\vec{P}^{(3)}$ is given by

$$\begin{aligned} \vec{P}^{(3)}(\omega, \tau) &= \chi^{(3)}(\omega, \tau) \vec{E}_{\text{pump}}(\omega) \vec{E}_{\text{pump}}^*(\omega) \vec{E}_{\text{probe}}(\omega) \\ &\propto S(\omega) T(\tau) \vec{E}_{\text{pump}}(\omega) \vec{E}_{\text{pump}}^*(\omega) \vec{E}_{\text{probe}}(\omega) . \end{aligned} \quad (2.32)$$

Here we have made the simplification that the pump and probe pulses are very short (such that they can be represented by delta functions) and that the system first has two interactions with the pump pulse and then – after a delay τ – an interaction with the probe pulse. The response function $T(\tau)$ describes the dynamics of the excited state relaxation, for instance $T(\tau) = e^{-\tau/T_1}$ for an excited state that exponentially decays with a relaxation time T_1 . The function $S(\omega)$ describes the line shape of the excited state, for instance $S(\omega) = \frac{T_2^{-1}}{(\omega - \omega_0)^2 + T_2^{-2}}$ for a Lorentzian line shape with a dephasing time T_2 .

The microscopic origin of $\vec{P}^{(3)}(\omega, \tau)$ is shown in Fig. 2.6, for the case where the probe pulse comes later in time than the pump pulse and where the system contains three energy levels (these are not unique, since the pump interactions can proceed in different orders). There are contributions from stimulated emission, ground state bleach, and the $1 \rightarrow 2$ transition. In Chapter 3, a typical pump-induced absorption signal is shown, for the case where the $0 \rightarrow 1$ and the $1 \rightarrow 2$ transition occur at different center frequencies, due to an anharmonic potential that leads to different binding constants C_i for the different transitions (see Fig. 3.3).

In the case of temporal overlap of the pump and probe pulses, there are additional resonant contributions to $\vec{P}^{(3)}$ (e.g. due to pump-probe-pump field interactions) as well as non-resonant interactions that affect that signal (e.g. the optical Kerr effect). These artifacts can be ignored at later delay times τ . By varying τ , the relaxation dynamics of the system, represented by the response function $T(\tau)$, are monitored. After a long delay τ , the response function $T(\tau)$ has decayed to zero and the detected electric field in the direction $\vec{k} = \vec{k}_s$ is the probe pulse in the absence of the pump. This gives a pump-induced absorption $\Delta\alpha$ that is zero, as is clear from Eqs. 2.31 and 2.32.

2.2.4 ANISOTROPIC POLARIZATION

In the previous section, we briefly discussed anisotropic media, with a focus on uniaxial birefringent crystals and their use for phase matching. In this section, we discuss two cases of *field-induced* anisotropy in media with their applications: non-resonant $\chi^{(2)}$ for THz detection and resonant $\chi^{(3)}$ for polarization-resolved pump-probe spectroscopy.

NON-RESONANT $\chi^{(2)}$: THz DETECTION To detect THz radiation, a THz pulse is overlapped with a second pulse in a ZnTe crystal. The second pulse with frequency ω_0 is short compared to the THz pulse and is used for heterodyned

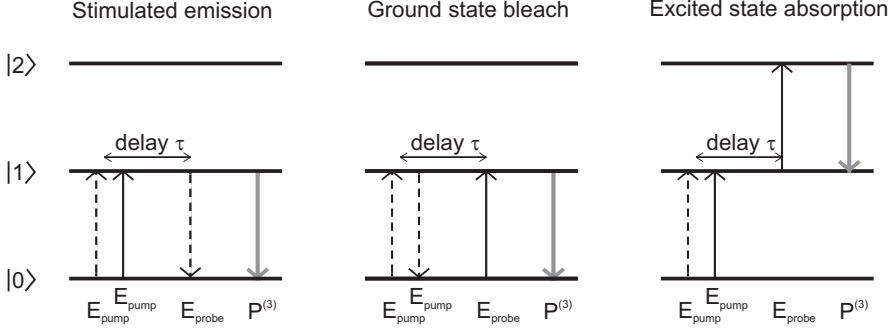


FIGURE 2.6. The wave mixing energy level diagrams showing the three different microscopic processes that cause a macroscopic $P^{(3)}$ for which the probe field E_{probe} interaction occurs after the two pump field E_{pump} interactions. The field radiated by this polarization interferes with the linear probe pulse, giving rise to negative (stimulated emission and ground state bleach) or positive ($1 \rightarrow 2$ absorption) pump-induced absorption $\Delta\alpha$. In this figure, upwards (downwards) arrows indicate absorption (emission) of a photon from the interacting field. Straight (dashed) arrows indicate that the field acts on the ket (bra), in the density matrix formalism where $|a\rangle\langle a|$ represents a population in state $|a\rangle$ and $|a\rangle\langle b|$ is a coherence between the states $|a\rangle$ and $|b\rangle$. These diagrams are simplifications of the Feynman diagrams as can be found in Ref. [113].

detection of the quasi-static electric field of the THz pulse. The following field is incident on the ZnTe crystal

$$\vec{E}(t) = \vec{E}_0(t + \tau)e^{i(\omega_0 t - \vec{k}_0 \cdot \vec{r})} + \vec{E}_{\text{THz}}(t) , \quad (2.33)$$

where τ is the time delay between the detection pulse with frequency ω_0 and the THz pulse with $\omega = 0$. The THz pulse is represented by a pulse envelope only (the SVEA does not apply here). The electric field of the THz pulse has an effect on the position of the atoms of the crystal, such that the crystal becomes birefringent (due to the symmetry group of ZnTe, which is $\bar{4}3m$). This is clear from the non-resonant second order polarization that is created in the crystal

$$\vec{P}^{\text{NL}} = \chi_{ijk}^{(2)}(\omega = \omega_0 + 0)\vec{E}_0(\omega_0)\vec{E}_{\text{THz}}(0) . \quad (2.34)$$

This polarization leads to an effective susceptibility at frequency ω_0 , which depends on the THz electric field strength: $\chi_{ijk}^{\text{eff}} = \chi^{(1)} + 2\chi_{ijk}^{(2)}\vec{E}_{\text{THz}}$. The third-rank tensor $\chi_{ijk}^{(2)}$ describes which polarization components arise due to which electric field components of the waves \vec{E}_0 and \vec{E}_{THz} and can lead to an effective refractive index that is different for different field directions. If the

probe pulse has electric field components in two of these differing directions, one of these components will be delayed with respect to the other, changing the polarization of the probe pulse. If the incoming probe wave has a linear polarization, the outgoing wave will be elliptical, where the ellipticity depends linearly on the strength of the electric field of the THz pulse. Therefore, measuring the ellipticity as function of delay τ yields the electric field of the THz pulse as a function of time.

RESONANT $\chi^{(3)}$: POLARIZATION-RESOLVED PUMP-PROBE SPECTROSCOPY In addition to excited state relaxation, there can be rotational relaxation in a system, for instance due to reorientation of excited molecules. This process can be monitored using polarization-resolved pump-probe spectroscopy. In a polarization-resolved pump-probe experiment, the pump-induced absorption change is measured for pump and probe polarization parallel $\Delta\alpha_{\parallel}$ and perpendicular $\Delta\alpha_{\perp}$. An optical transition between a ground state $|\psi_0\rangle$ and an excited state $|\psi_1\rangle$ is most efficient when the polarization and transition dipole moment are parallel, which comes from the coupling term, as expressed in Fermi's golden rule

$$\Gamma_{0\rightarrow 1} \propto \cos^2 \theta \left| \langle \psi_0 | \hat{\mu} | \psi_1 \rangle \right|^2 \delta(\omega \pm \omega_{0\rightarrow 1}) , \quad (2.35)$$

where $\Gamma_{0\rightarrow 1}$ is the transition rate and θ is the angle between the polarization of the electric field and the transition dipole moment $\langle \psi_0 | \vec{\mu} | \psi_1 \rangle$.

Due to this dependence on θ , directly after pump excitation, i.e. at short delay τ , an anisotropic distribution of excited states is created. This will result in different microscopic response functions $T_{\parallel}(\tau)$ and $T_{\perp}(\tau)$ and hence different pump-induced absorptions $\Delta\alpha_{\parallel}$ and $\Delta\alpha_{\perp}$. After rotational relaxation has finished, the excited states are isotropically distributed and the two response functions will be equal: $T_{\parallel}(\tau \rightarrow \infty) = T_{\perp}(\tau \rightarrow \infty)$. This means that the response functions are delay-time dependent tensors, whose time evolution reflects both excited state relaxation and molecular reorientation processes.

2.3 MOLECULAR REORIENTATION

Since most of the chapters of this thesis are concerned with the reorientational dynamics of (water) molecules, we will discuss the process of angular diffusion. We also discuss how molecular reorientation can be measured, in particular with dielectric relaxation spectroscopy and polarization-resolved pump-probe spectroscopy.

2.3.1 GENERAL

The process of angular diffusion is described by the following differential equation

$$\nabla_{\vec{r}}^2 f = \frac{1}{D} \frac{\partial f}{\partial t} , \quad (2.36)$$

where $f(\theta, \phi, t)$ is the probability distribution function for a molecule to have an orientation (θ, ϕ) at time t ; D is the rotational diffusion constant and $\nabla_{\vec{r}}$ is the partial differential operator in spherical coordinates. Due to the axial symmetry in the relevant experimental cases, the observed angular diffusion does not depend on changes in the orientation with respect to the angle ϕ (see Fig. 2.7). Using separation of variables (time and space), we can write the solution to Eq. 2.36 as

$$f = \sum_l P^{(l)}(\theta) a^{(l)}(t) , \quad (2.37)$$

with the Legendre polynomials $P^{(l)}$ of rank l and $a^{(l)}$ a function that describes the temporal evolution. Eq. 2.36 for each rank l becomes

$$\nabla_{\vec{r}}^2 P^{(l)} a^{(l)} = -l(l+1) P^{(l)} a^{(l)} = \frac{1}{D} \frac{\partial P^{(l)} a^{(l)}}{\partial t} , \quad (2.38)$$

where

$$P^{(l=1)}(x) = x \quad , \quad P^{(l=2)}(x) = 3x^2 - 1, \dots . \quad (2.39)$$

The Legendre polynomials contain information on the geometry of the system and are functions of $x = \cos \theta$. With respect to the time dependence, Eq. 2.38 leads to exponentially decaying orientational probability distribution functions

$$a^{(l)} = e^{-t/\tau_{\text{reor}}^{(l)}} \quad \text{with} \quad \tau_{\text{reor}}^{(l)} = \frac{1}{Dl(l+1)} . \quad (2.40)$$

Here, $\tau_{\text{reor}}^{(l)}$ is the reorientation time that depends on the rank. The reorientation time of rank 1 is thus three times larger than the reorientation time of rank 2.

The time-dependent distribution function of the molecular orientation $P^{(l)}(t)$ of a dipole \vec{p} is closely related to the correlation function $C^{(l)}(t)$ of rank l , where

$$C^{(l)}(t) \propto \langle P^{(l)}[\vec{p}(0) \cdot \vec{p}(t)] \rangle . \quad (2.41)$$

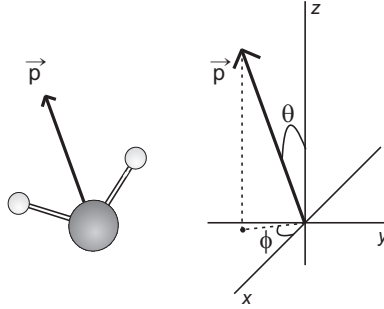


FIGURE 2.7. The geometry of a (water) molecule with dipole vector \vec{p} in a coordinate system with angles θ and ϕ .

Here, $\langle \dots \rangle$ represents a statistical average. For short delays t , the orientation of a molecule at time t is almost identical to the orientation at $t = 0$; at long delays, the orientation at time t is not correlated with the orientation at $t = 0$. The decay time of $C^{(l)}(t)$ is identical to the time constant $\tau_{\text{reor}}^{(l)}$. Since the correlation functions can be measured as a function of time, these measurements make it possible to determine the corresponding reorientation times.

2.3.2 FIRST ORDER CORRELATION FUNCTION

In Section 2.2.2, we saw that orientational polarization leads to the dielectric relaxation equation (Eq. 2.20) with reorientation time τ_{reor} . According to statistical mechanical calculations [20], the response function is proportional to the first order correlation function of the molecular dipole vector \vec{p}

$$F_{\vec{p}}(t) \propto C^{(1)}(t) = \langle \vec{p}(0) \cdot \vec{p}(t) \rangle = \langle \cos \theta(t) \rangle . \quad (2.42)$$

Since this is equal to the first order Legendre polynomial of $\cos \theta$, this means that the reorientation time τ_{reor} that occurs in the dielectric relaxation equation (Eq. 2.20) is the first order reorientation time of the dipoles in the sample $\tau_{\text{reor}}^{(1)}$. Here, the external electric field that creates the orientational polarization is assumed to be polarized in the z -direction (see Fig. 2.7). An experiment that determines the complex dielectric function as a function of frequency $\hat{\epsilon}(\omega)$ is called a dielectric relaxation experiment and can yield the first order reorientation time scale(s) of the molecular dipoles in the system. In a number of chapters in this thesis dielectric relaxation measurements in the THz regime are presented.

2.3.3 SECOND ORDER CORRELATION FUNCTION

Besides dielectric relaxation measurements, this thesis also describes the results of polarization-resolved pump-probe measurements. These measurements are also sensitive to orientational relaxation, as shown in Section 2.2.4, where the difference between pump-induced absorption for pump and probe polarization parallel and perpendicular $\Delta\alpha_{\parallel} - \Delta\alpha_{\perp}$ was found to depend on the delay time τ between arrival of the pump and probe pulse. The decay of this signal is also influenced by excited state relaxation, which is removed by defining the anisotropy

$$R(\tau) = \frac{\Delta\alpha_{\parallel} - \Delta\alpha_{\perp}}{\Delta\alpha_{\parallel} + 2\Delta\alpha_{\perp}} , \quad (2.43)$$

where the denominator is known as the isotropic signal, which only contains the excited state relaxation dynamics. The factor 2 originates from the fact that there are two directions perpendicular to the pump polarization (x and y) and only one parallel (z). Here it is assumed that the pump pulse creates an induced polarization in the z -direction (see Fig. 2.7), giving rise to an initial distribution of excited molecules that is proportional to $\cos^2\theta$. It can be shown that the decay of the anisotropy $R(\tau)$ is proportional to the second order correlation function

$$R(\tau) \propto C^{(2)}(t) = \langle P^{(2)}[\vec{p}(0) \cdot \vec{p}(t)] \rangle . \quad (2.44)$$

Therefore the decay of the anisotropy yields the second order reorientation time of the excited molecules in the sample $\tau_{\text{reor}}^{(2)}$. This reorientation time is determined for a number of aqueous solutions throughout this thesis. In some chapters, a comparison is made between the results from first order dielectric relaxation measurements and second order polarization-resolved pump-probe measurements.

It is possible to define an angle, the magic angle, where the second order Legendre polynomial of $\cos\theta$ is zero: $3\cos^2\theta - 1 = 0 \rightarrow \theta = \arccos\frac{1}{\sqrt{3}} = 54.7^\circ$. Hence at the magic angle there is no dependence of the probed signal on reorientation dynamics. Therefore - even though an anisotropic distribution of excited molecules could be created - randomization of the orientation of the excited molecules does not lead to a change in the probed signal. Hence, only the isotropic contributions, i.e. due to the lifetime of the excitation, remain.

References

This chapter is largely based on the following books:

Introduction to Electrodynamics [50], *Theory of Electric polarization, Vol. 1* [19], *Theory of Electric polarization, Vol. 2* [20], *Nonlinear Optics* [21] and *Principles of Nonlinear Optical Spectroscopy* [113].

3 EXPERIMENTAL TECHNIQUES

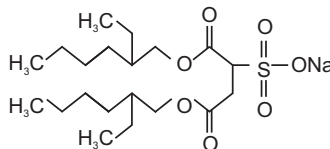
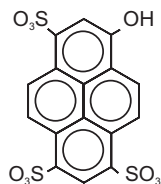
In this chapter we describe the samples on which the measurements in this thesis were performed. Subsequently, we give a general description of the measurement techniques that were used, followed by the experimental realization of these techniques.

3.1 SAMPLES

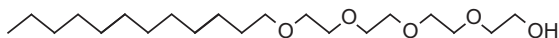
All samples that are described throughout this thesis have in common that they contain water, for which we used purified (Millipore) water. The substances that we solvated in water for the different measurements were used as purchased. For the measurements in Chapter 5, neat water (4% D₂O in H₂O) was examined. In Chapters 6 and 7, we used solutions containing the salts NaCl, KCl, CsCl, LiCl, NaClO₄, NaI, Cs₂SO₄, Mg(ClO₄)₂, LiI, MgCl₂, Na₂SO₄ and MgSO₄; and the acids HCl, HClO₄ and HI (all from Sigma Aldrich). In Chapter 8, we studied the photoacid 8-hydroxy-1,3,6-pyrenetrisulfonic acid (HPTS) inside a water nanopool, i.e. a reverse micelle formed by either the ionic surfactant sodium dioctyl sulfosuccinate (AOT) in isooctane apolar solvent or the non-ionic surfactant polyoxyethylene(4)lauryl ether (BRIJ-30) in cyclohexane apolar solvent (all chemicals purchased from Sigma Aldrich). The chemical structures of these molecules are shown in Fig. 3.1A-C. In Chapter 9 we describe measurements on mixtures of water with the amphiphilic molecule 1,1,3,3-Tetramethylurea (TMU, >99% purity, purchased from Sigma Aldrich), shown in Fig. 3.1D. Finally, in Chapter 10 we examine stacked lipid bilayers with different hydration levels, consisting of the lipid 1,2-Dioleoyl-*sn*-Glycero-3-Phosphocholine (DOPC, purchased from Avanti Polar Liquids), shown in Fig. 3.1E.

The different aqueous solutions were contained between windows or in a cuvette of a material that is transparent to light of the wavelength used in the specific measurement: Infrasil Quartz in the case of THz measurements and CaF₂ in the case of mid-infrared and visible measurements. To make sure that enough light was transmitted to be detected, an optical path length between 25 and 250 μm was used. In some cases, the sample cells were equipped with a Peltier element to be able to vary the temperature.

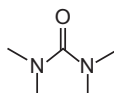
- A HPTS** (Photoacid, Ch. 8) **B AOT** (Anionic surfactant, Ch. 8)



- C BRIJ-30** (Non-ionic surfactant, Ch. 8)



- D TMU** (Molecule with hydrophobic groups, Ch. 9)



- E DOPC** (Lipid for model membrane, Ch. 10)

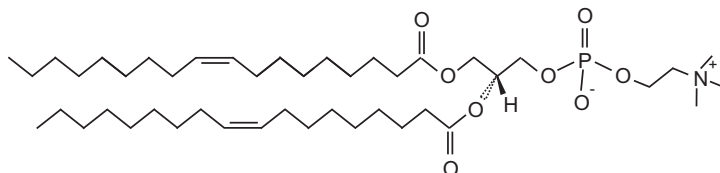


FIGURE 3.1. Chemical structures of relevant molecules.

3.2 MEASUREMENT TECHNIQUES

The measurements that are described in this thesis were recorded using the experimental techniques described in the following.

3.2.1 TERAHERTZ TRANSMISSION SPECTROSCOPY

In the terahertz time-domain transmission setup, an optical terahertz pulse (duration ~ 3 ps) is created and detected with high temporal resolution (< 150 fs), as explained in Sections 2.2.3 and 2.2.4. If the terahertz pulse propagates through a medium, it can experience refraction and absorption, the former leading to a delay of the pulse and the latter to a decrease in amplitude of the pulse, with respect to a pulse propagating through air, see Fig. 3.2. Therefore, the comparison of the transmission of THz pulses through air and through a sample enables the determination of the complex refractive index of the sample $\hat{n} = n - i\kappa$, where n is the refractive index and κ the extinction coefficient. The

THz pulse that is measured in the time domain contains frequency components in the region 0.2-1.6 THz. Hence, taking the Fourier transform makes it possible to determine the refractive index of the sample as a function of frequency $\nu = \frac{\omega}{2\pi}$ in this range. In the case of polar liquids, it is most convenient to describe the material properties in terms of the complex dielectric function $\hat{\epsilon} = \epsilon' - i\epsilon'' = \hat{n}^2$. For polar liquids, $\hat{\epsilon}$ shows a marked frequency dependence, which is caused by dielectric relaxation phenomena, i.e. processes related to reorientations of dipoles, as described in Section 2.2. Since water molecules have a permanent dipole moment, this technique is highly suitable for our studies to learn about the reorientation processes in aqueous solutions. This technique was used for the measurements in Chapters 6, 7, 9 and 10.

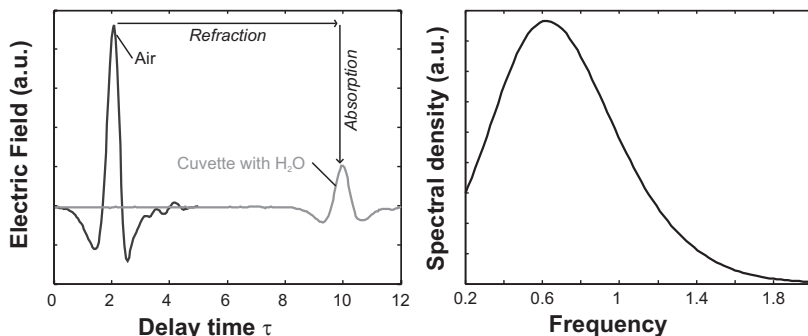


FIGURE 3.2. The electric field as a function of time for a THz pulse transmitted through air and a THz pulse transmitted through a cuvette filled with water. The pulses are clearly delayed and attenuated due to refraction and absorption, respectively, but also have a somewhat different shape, indicating a frequency dependence of the dielectric properties of water. The spectral density of the pulse through air is shown in the right figure as a function of frequency ν .

3.2.2 INFRARED PUMP-INFRARED PROBE SPECTROSCOPY

Infrared pump-infrared probe spectroscopy is used to probe directly the reorientation of water molecules in time. In this one-color pump-probe technique, the pump and probe pulses have the same wavelength. Here we use infrared pulses that are resonant with the OD-stretch mode of partially diluted water (4% D₂O in H₂O) to avoid resonant (Förster) energy transfer between excited stretch vibrations (for details, see Chapter 4). The pump pulse excites the OD-stretch mode and the probe pulse examines the pump-induced changes in absorption $\Delta\alpha$, which is the difference in absorption by a sample that was excited by the pump light and the absorption by an unexcited sample. As discussed in Section 2.2.3, $\Delta\alpha$ contains three contributions: induced absorption of the 1 \rightarrow 2 transition, a reduced absorption of the 0 \rightarrow 1 transition (bleach) and

stimulated emission of the $1 \rightarrow 0$ transition (see Fig. 3.3). The pump-induced change in absorption does not live indefinitely, but is limited by the vibrational lifetime of the OD-stretch vibration. This results in the decay of $\Delta\alpha$ as a function of time t . The decay of $\Delta\alpha(t)$, however, also depends on the polarization of the pump pulse with respect to the probe pulse. The pump pulse will preferentially excite water molecules with their OD-stretch transition dipole moment along the direction of the polarization of the pump pulse, resulting in an anisotropic initial distribution of excited molecules. These excited water molecules randomize their orientation as a function of time, leading eventually to an isotropic distribution. By probing $\Delta\alpha(t)$ for pump and probe pulses with parallel polarizations $\Delta\alpha_{\parallel}$ and with perpendicular polarizations $\Delta\alpha_{\perp}$, we can construct the anisotropy $R(t)$, whose decay reflects the reorientation of water molecules, as shown in Chapter 2. Details on constructing $R(t)$ are given in Section 2.3.3. Polarization-resolved infrared pump-infrared probe spectroscopy was conducted for the measurements in Chapters 5, 6 and 7.

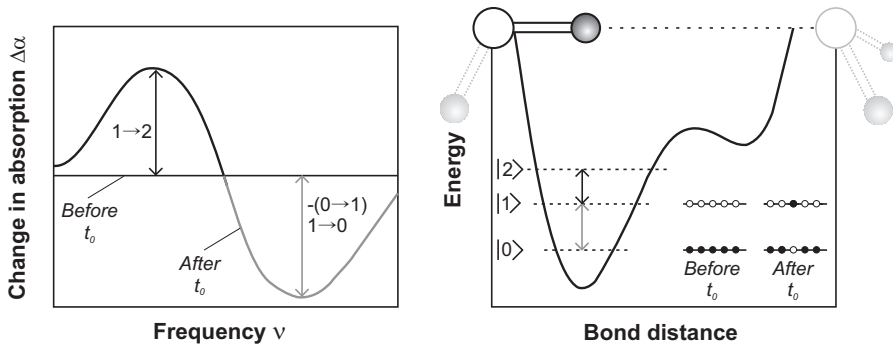


FIGURE 3.3. The left figure is a schematic representation of a typical pump-probe spectrum before pump excitation at time zero (t_0) and after t_0 for the water OD-stretch region. In the right figure, the potential energy for the OD bond distance of a water molecules is shown with the ground state and the two first excited states. Also a hydrogen-bonded neighboring water molecule is shown. Before t_0 all water molecules have their OD-stretch mode in the vibrational ground state $|0\rangle$. After t_0 , some water molecules have their OD-stretch mode promoted to the first excited state $|1\rangle$. As a result, the probe pulse measures induced absorption from the first to the second excited state, leading to a positive $\Delta\alpha$. Molecules in the first excited state can also decay to the ground state by stimulated photon emission, leading to a negative $\Delta\alpha$. Additionally, since there are fewer molecules to excite from $|0\rangle$ to $|1\rangle$ after t_0 than before t_0 , the $0 \rightarrow 1$ absorption is smaller (bleach), also leading to a negative $\Delta\alpha$. If the potential energy for the OD-bond distance would be perfectly harmonic, the frequencies of the $0 \rightarrow 1$ and the $1 \rightarrow 2$ transition would be the same and $\Delta\alpha(\omega) \equiv 0$. However, the potential energy landscape is anharmonic and can be described by e.g. the Lippincott-Schröder model [7, 94]. Due to this anharmonicity, the induced absorption is spectrally separated from the bleach and the stimulated emission.

3.2.3 VISIBLE PUMP-INFRARED PROBE SPECTROSCOPY

In visible pump-infrared probe spectroscopy, the pump pulses have a wavelength in the visible regime, while the probe pulses are in the infrared regime. This typically means that the sample under study undergoes an *electronic* transition upon interaction with the pump pulse and the effect of this on *vibrational* modes is studied. In our studies, we use this technique to study, as a function of pump-probe delay time, the release of a proton from a molecule. To study these dynamics, we take the photoacid HPTS, which upon electronic excitation with 400 nm light becomes very acidic, resulting in the release of a proton. The dynamics of this process can then be followed in time through the vibrational modes of the HPTS molecule, some of which are associated with the molecule in the acidic form (with the proton still attached) and with the molecule in the basic form (with the proton fully donated to the water solvent). There are also vibrational modes associated with the proton itself that can be monitored as a function of time. This technique is employed in Chapter 8.

3.2.4 VISIBLE PUMP-VISIBLE PROBE SPECTROSCOPY

In addition to monitoring vibrational modes after an electronic excitation, we also monitor changes in the electronic modes through visible pump-visible probe spectroscopy. We apply this technique to the photoacid molecule HPTS to examine the electronic changes that occur while a proton is being released from the molecule to the solvent. To this end, we use a pump pulse of 400 nm and a so-called white light probe that covers a range of colors in the visible regime. In a variant of this technique, we block the probe pulse and measure the time-integrated fluorescence of the molecule after pump excitation. We use the technique of visible pump-visible probe (and the fluorescence measurement technique) in Chapter 8.

3.2.5 AUXILIARY MEASUREMENTS

In addition to the techniques described above, we use two standard optical transmission measurement setups to examine the absorptive properties of our samples: a double beam spectrometer in the mid-infrared range (Perkin-Elmer 881) and a spectrometer in the UV-Visible range (Jasco V530). Finally (see Chapter 9), we measured the dielectric properties of samples between 200 MHz and 50 GHz with guided electromagnetic waves that were electronically created and detected by an Agilent E8364B vector network analyzer. These waves were propagated through an open-ended coaxial cable attached to the sample. From the complex reflection coefficient we obtained the dielectric properties of the sample in this frequency range. These measurements were done in the group of prof. R. Buchner at the University of Regensburg (Germany).

3.3 EXPERIMENTAL REALIZATIONS

This section describes the experimental realizations of the measurement techniques as described above. The following 4 figures provide a schematic overview of the different setups, explained in detail in the captions.

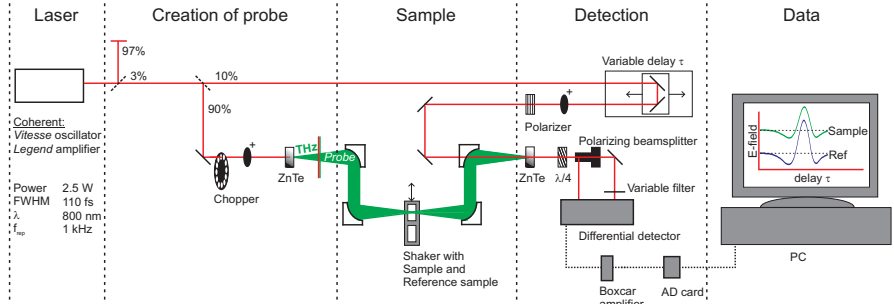


FIGURE 3.4. *Terahertz probe setup.* A small fraction of the laser output is split into two branches: one to generate THz pulses and one to detect the THz pulses. In the THz generation branch, the 800 nm light ($\sim 70 \mu\text{J}$ per pulse) is loosely focused in a ZnTe crystal ((110) orientation, 1 mm thick), where THz pulses with a duration of ~ 3 ps are generated through optical rectification, as described in Section 2.2.3 and Fig. 2.5. After filtering out the remaining 800 nm light, the THz beam is first collimated and then focused by parabolic mirrors. A mechanical device (shaker) is used to position two cuvettes (with an optical path length of $103 \pm 0.5 \mu\text{m}$) alternatively in the THz focus - one containing the sample and one the reference sample that is used for calibration. This mechanical device has a duty cycle of 4 seconds: it averages the transmission through the sample for one second; then it has one second to move to the position where the reference sample is in the focus; after this, the average transmission through the reference sample is measured during one second; and finally it has one second to move back. The transmitted THz pulses are collimated and focused in a second ZnTe crystal. Here, also the 800 nm pulses from the sampling branch are focused after passing through a delay line. The electric field of the THz pulses induces a birefringence in the ZnTe crystal, which causes the 800 nm sampling pulses to change their polarization from linear to slightly elliptical, as explained in Section 2.2.4. The 800 nm sampling pulses are then sent through a $\lambda/4$ plate (to enhance the sensitivity to the THz induced birefringence) and then the s and p polarization components are separated by a polarizing beam splitter. The intensities of these components are subsequently measured by a differential detector with balanced diodes. The 800 nm light from the sampling beam passes through a variable delay line, which is used to record the quasi-instantaneous electric field of the THz pulses as a function of delay time τ . A 500 Hz chopper before THz generation blocks every other laser shot for active background subtraction. With a Boxcar amplifier (Stanford Research Systems SR250) and AD card THz pulses that are transmitted through the sample and through the reference sample, are recorded.

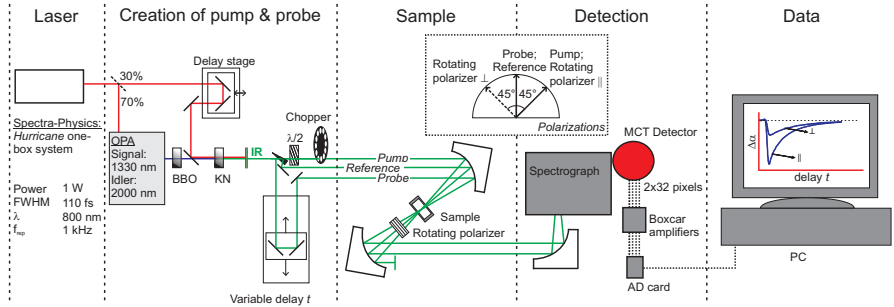


FIGURE 3.5. *Infrared pump-infrared probe setup.* Part of the 800 nm light from the laser is used to pump a white-light seeded OPA (Spectra-Physics). The resulting idler pulses, with a wavelength of 2000 nm, are doubled in a BBO crystal and the resulting pulses with a wavelength of 1000 nm are then passed through a KNbO_3 (KN) crystal, simultaneously with the remaining 800 nm light from the laser. Through difference-frequency mixing, infrared light with a wavelength of $4 \mu\text{m}$ (corresponding to a frequency of 2500 cm^{-1} or 75 THz) is created. After passing through a long wave pass filter, the infrared light ($\sim 4 \mu\text{J}$) then passes through a wedged CaF_2 window, where the transmitted light ($\sim 95\%$) is used as the pump; the light reflected at the front is used as the probe; and the light reflected at the back is used as the reference. The pump polarization is then rotated by 45° with respect to the probe and reference using a $\lambda/2$ plate and focused in the sample (contained between two CaF_2 windows separated by a spacer with a thickness around $25 \mu\text{m}$) using a parabolic mirror. The pump beam passes through a 500 Hz chopper in order to increase the sensitivity towards pump-induced changes in the absorption of the sample. The probe light passes through a variable delay line, before being focused on the same spot in the sample as the pump light. With the delay line, the timing can be tuned such that the probe arrives before (t negative) or after the pump pulse (t positive). The reference beam, used to correct for pulse to pulse intensity fluctuations, is focused at a different spot in the sample. After passing through the sample, the pulses pass through a polarizer, which rotates between two positions: selecting the polarization component of the probe that is parallel to the pump polarization or the polarization component of the probe that is perpendicular to the pump polarization. The probe and reference beams are spectrally dispersed through a grating in a spectrograph and detected with a 2×32 pixel liquid-nitrogen cooled HgCdTe (MCT) detector (Infrared Associates). After integration of typically a few hundred laser shots in Boxcar amplifiers, the data contains the pump-induced change in absorption $\Delta\alpha(t, \nu)$ of the sample at each frequency pixel ν for different time delays t for the two polarizations \parallel and \perp .

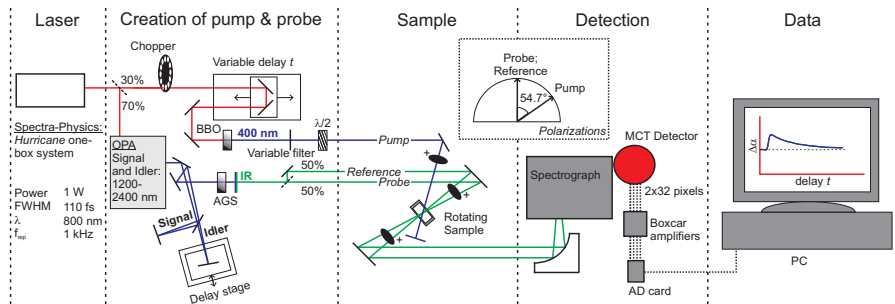


FIGURE 3.6. *Visible pump-infrared probe setup.* About 30% of the output of the laser is used for the visible pump branch, where the 800 nm light is frequency doubled in a BBO crystal ($\theta = 29^\circ$, 2 mm thick) to create 400 nm pump pulses. The polarization is then set at magic angle with respect to the probe light with a $\lambda/2$ plate, ensuring that only isotropic signals are measured. The pump (attenuated to $\sim 1 \mu\text{J}$) is then focused in the sample that is mounted in a rotating sample holder to avoid photodegradation. The sample is held between two CaF_2 windows separated by a teflon spacer with a thickness of 100-200 μm . The probe pulses are tunable infrared pulses with a wavelength between 8 and 2.7 μm (approximately $1250\text{-}3700 \text{ cm}^{-1}$ or 40-110 THz). These are created by using the remaining 800 nm light (70% of the laser output) to pump a white-light seeded OPA (Spectra-Physics). The resulting signal (1200-1600 nm) and idler pulses (1600-2400 nm) are separated and then overlapped in time and space in a AgGaS_2 (AGS) nonlinear crystal to create infrared light through difference-frequency mixing. The infrared light is subsequently split in two equal parts, that serve as the probe pulse and the reference pulse that is used to compensate for pulse intensity fluctuations. The probe beam is focused on the same spot in the sample as the pump, whereas the reference beam is focused at a slightly different spot. The relative time delay t between the pump and probe pulses is tuned using a variable delay line. A 500 Hz chopper in the pump branch is used to be sensitive only to pump-induced changes in the absorption of the sample $\Delta\alpha$. The frequency-dependent absorption changes are measured using the same detection scheme as in the infrared pump-infrared probe setup (Fig. 3.5).

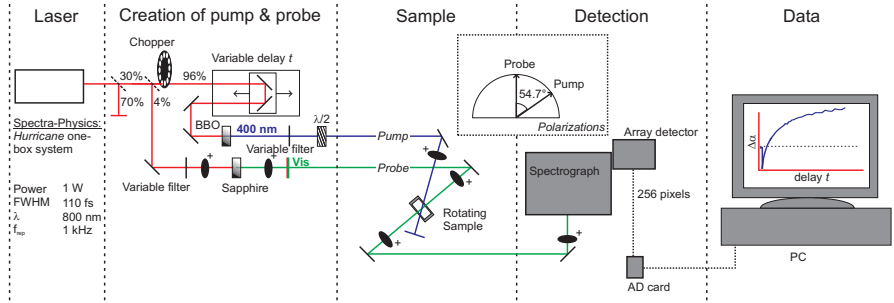


FIGURE 3.7. *Visible pump-visible probe setup.* The generation of the pump beam in this setup is identical to that in the visible pump-infrared probe setup. To generate visible continuum probe pulses, $\sim 1 \mu\text{J}$ of the 800 nm light of the probe branch is focused into a 3 mm thick z-cut sapphire substrate to generate a broadband continuum of wavelengths ranging from over 1000 nm to just below 400 nm. These pulses are focused on the same spot in the sample as the pump pulses. The sample and sample holder are the same as in the visible pump-infrared probe setup. The probe pulses are spectrally dispersed with a grating-based spectrograph (Acton) and detected with a home-built diode array detector. By passing the pump beam through a variable delay line and a 500 Hz chopper, the probe pulses are sensitive to the pump-induced absorption changes $\Delta\alpha$ of the sample as a function of pump-probe delay time t for a range of probe frequencies (typically 400-700 nm).

4 DATA ANALYSIS

In this chapter we describe the methods that were used to analyze the data obtained with the experimental techniques from the previous chapter. For the THz time-domain transmission measurements we distinguish the case where we use a variable-thickness sample cell, and the case where we measure two samples quasi-simultaneously, where the reference sample is used for calibration. We discuss the analysis for the pump-probe measurements in the visible and infrared, focusing first on the isotropic signals and then on the anisotropic signals.

4.1 TERAHERTZ MEASUREMENTS

In the terahertz measurements, we measure the time evolution of the electric field $E(\tau)$ of the pulse, which gives information on both amplitude and phase changes that occur in the sample. This allows the determination of the frequency-dependent complex dielectric function $\hat{\epsilon}(\omega)$. The extraction procedure will be described in the following two sections, where we deal with the analysis for two types of terahertz transmission measurements: without calibration and with calibration of the dielectric response of the sample under study.

4.1.1 WITHOUT CALIBRATION: USING VARIABLE-THICKNESS SAMPLE CELL

In the THz time-domain spectroscopy experiments, the presence of the sample leads to a reduction of the THz pulse amplitude (absorption) and to a temporal shift of the THz pulse (refraction). These two quantities can be determined for all the spectral components contained in the THz pulse and can be directly related to the frequency-dependent complex refractive index, $\hat{n}(\omega) = n(\omega) - i\kappa(\omega)$, of the sample. In principle, a comparison of the Fourier transforms of the THz temporal traces with and without the sample provides the frequency-dependent refractive index $\hat{n}(\omega)$. The extraction of $\hat{n}(\omega)$ of the sample is, however, complicated by the fact that the sample is contained within a sample cell with windows that also affect the THz wave. We can extract the complex refractive index through measurements at varying sample thickness d [73] and thereby isolating the sample response from the window response. With this approach, the

reference is the sample itself and the contribution of the cell windows is directly corrected for. The time-domain data is converted to the frequency domain to obtain the frequency-dependent complex refractive index, using

$$n(\omega) = \frac{\phi(\omega, d + \delta d) - \phi(\omega, d)}{\omega \delta d} \times c = \frac{\Delta \phi(\omega)}{\omega \delta d} \times c, \quad (4.1)$$

$$\kappa(\omega) = \frac{\ln E(\omega, d) - \ln E(\omega, d + \delta d)}{\omega \delta d} \times c = \frac{\Delta \ln E(\omega)}{\omega \delta d} \times c, \quad (4.2)$$

where we calculate the frequency-dependent real and imaginary part of the refractive index, respectively. Here, we use the Fourier transform of the electric field $E(\omega)$ and the phase of the THz pulse $\phi(\omega)$; δd is the change in thickness between two subsequent measurements and c is the speed of light in vacuum. As is apparent from these equations, the phase change $\Delta \phi(\omega)$ and the change in the natural logarithm of the electric field $\Delta \ln E(\omega)$ depend linearly on δd for a given frequency, with a slope proportional to n and κ , respectively. Therefore, at each frequency a linear model can be used for describing the experimental results in order to extract n and κ as shown in Fig. 4.1 for some selected frequencies. We use the variable-thickness method of extracting $\hat{\epsilon}(\omega)$ for the measurements in Chapter 10 and for the temperature-dependent measurements in Chapter 9.

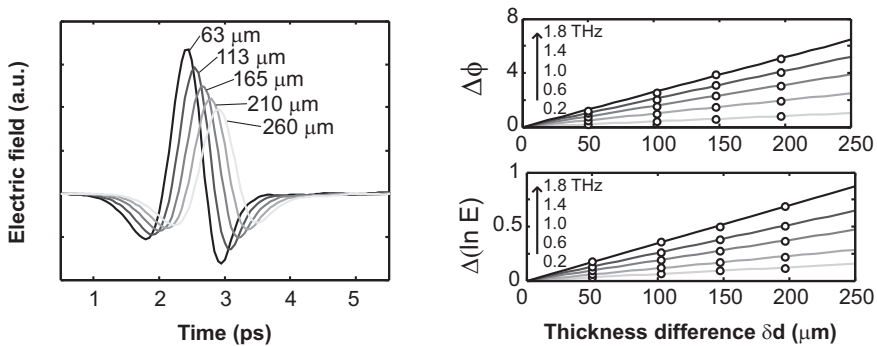


FIGURE 4.1. The left figure shows the transmitted THz pulses through samples of different thicknesses. The right figure shows the calculated $\Delta \phi$ and $\Delta(\ln E)$ as a function of difference in sample thickness δd .

4.1.2 WITH CALIBRATION: USING SAMPLE AND REFERENCE SAMPLE

The analysis of the data from the THz dielectric relaxation measurements with calibration of the dielectric response requires two steps:

1. *Extraction*: Translating the transmitted electric field of the THz pulses, measured as a function of time, to a complex frequency-dependent dielectric function of the sample and the reference sample;
2. *Calibration and modeling*: Using the reference sample with known dielectric properties to calibrate and model the dielectric function of the sample.

EXTRACTION To extract the dielectric function of a liquid sample that is contained in a cuvette, we need three measurements: (*A*) the transmitted THz pulse through air $E_{\text{air}}(\tau)$, (*B*) the transmitted pulse through an empty cuvette $E_{\text{cuv}}(\tau)$ and (*C*) the transmitted pulse through a cuvette containing a sample $E_{\text{sam}}(\tau)$. These measurements are each done for two positions of a mechanical device (shaker): left **L** and right **R**, where in step (*C*) one cuvette contains the sample and the other cuvette the reference sample that is used for calibration (see Fig. 4.2). The measurements for the positions **L** and **R** are always done consecutively (within the shaker duty cycle of 4 seconds) to reduce the effect of THz intensity and temperature fluctuations that occur on time scales longer than 4 seconds. We use the measurements through air (*A*) and through the cuvettes (*B*) to establish the dielectric properties of the cuvettes and subsequently the measurements through the cuvettes (*B*) and the samples (*C*) to obtain the dielectric properties of the samples.

The analysis is done in the frequency domain, after Fourier transformation of the THz time-domain pulses, yielding $E_{\text{air}}(\omega)$, $E_{\text{cuv}}(\omega)$ and $E_{\text{sam}}(\omega)$. The Fourier transform (mathematically) decomposes a THz pulse that contains frequencies between 0.2 and 1.6 THz into a set of harmonic waves with a fixed frequency, out of which we usually pick 32 to carry out the analysis on. In order to proceed, we need to know how a harmonic wave is affected when it passes through a system with certain dielectric properties. First of all, the wave propagation through a medium is different than through air due to refraction and absorption, as shown in Chapter 2. Furthermore, unlike when the wave passes through air, when it passes through a cuvette it experiences transitions between different media (air \rightarrow quartz \rightarrow air/sample \rightarrow quartz \rightarrow air, Fig. 4.3) that all give rise to transmitted and reflected fields. All these effects can be taken into account using the wave propagation factor p_i and the Fresnel transmission t_{ij} and reflection r_{ij} coefficients

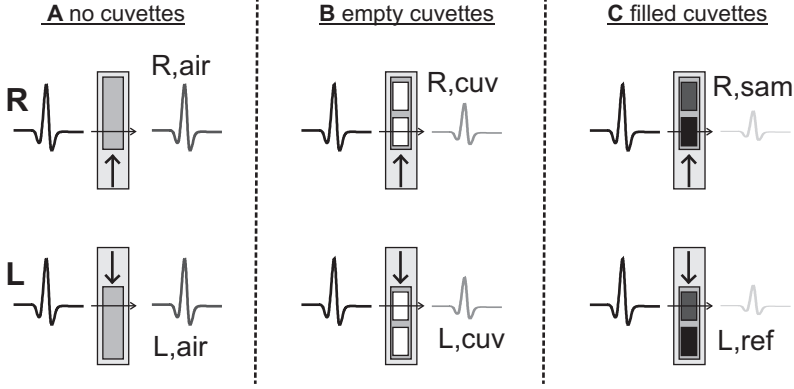


FIGURE 4.2. Schematic overview of the THz transmission measurement procedure. In step A, we measure the transmission through air for the two sample positions (**R** and **L**). In step B, we measure the transmission through the left and right cuvette (both cuvettes empty) and in step C, we measure the transmission through the left cuvette filled with a reference sample and the right cuvette filled with the sample.

$$p_i = e^{-i\hat{n}_i\omega L_i/c} \quad (4.3)$$

$$t_{ij} = \frac{2\hat{n}_i}{\hat{n}_i + \hat{n}_j} \quad (4.4)$$

$$r_{ij} = \frac{\hat{n}_j - \hat{n}_i}{\hat{n}_i + \hat{n}_j}, \quad (4.5)$$

where \hat{n}_i and \hat{n}_j are the complex refractive indices of the mediums i and j and L_i the thickness of medium i . It is convenient to consider propagation through 5 mediums (air–quartz–sample–quartz–air, for the filled cuvette). We find that when we start with a THz field $E_0(\omega)$, the transmission through air is given by

$$E_{\text{air}}(\omega) = E_0(\omega) \cdot p'_1 p'_2 p'_3 p'_4 p'_5, \quad (4.6)$$

with the prime denoting air, as all mediums consist of air.

In the case of transmission through a cuvette, we take into account the wave propagation, all interface transmissions and also multiple reflections between the windows (see Fig. 4.3) in the sample chamber between the cuvette windows. This yields

$$E_{\text{cuv}/\text{sam}}(\omega) = E_0(\omega) \cdot p'_1 t_{12} p_2 t_{23} \frac{p_3}{1 + r_{23} r_{34} p_3^2} t_{34} p_4 t_{45} p'_5, \quad (4.7)$$

where 1 and 5 represent air, 2 and 4 represent quartz windows and medium 3 contains either air or the sample.

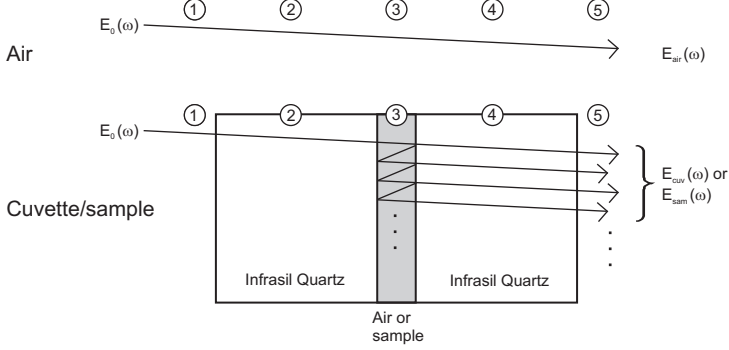


FIGURE 4.3. Schematic of the transmission of waves through air and through a cuvette, filled with air or with sample. The multiple reflections in the cuvette chamber lead to the terms $1 - r_{23}r_{34}p_3^2 + r_{23}^2r_{34}^2p_3^4 - r_{23}^3r_{34}^3p_3^6 + \dots$, which converges to $\frac{1}{1+r_{23}r_{34}p_3^2}$.

The extraction procedure continues by finding the unknown complex refractive index of the cuvette windows \hat{n}_{cuv} for a number of frequencies $\omega = \omega_k$ by minimizing $\left[\frac{E_{cuv}(\omega_k)}{E_{air}(\omega_k)} \right]_{calc.} - \left[\frac{E_{cuv}(\omega_k)}{E_{air}(\omega_k)} \right]_{meas.}$. When comparing the measurement through air and through an empty cuvette, the known parameters are the thicknesses of the cuvette windows (L_2 and L_4) and the refractive index of air ($n_{1,3,5} = 1$). Subsequently, the unknown complex refractive index of the sample is found by minimizing $\left[\frac{E_{sam}(\omega_k)}{E_{cuv}(\omega_k)} \right]_{calc.} - \left[\frac{E_{sam}(\omega_k)}{E_{cuv}(\omega_k)} \right]_{meas.}$. Here, the known parameters are the thickness of the cuvette chamber L_3 and the extracted complex refractive index of the cuvette windows \hat{n}_{cuv} . We used two cuvettes, for the positions **L** and **R**, that had a sample chamber thickness that was accurately determined by spectrophotometric interference (Starna Scientific, $d = 103 \pm 0.5 \mu\text{m}$). In measurement step *C*, a sample and a reference sample were measured, meaning that our analysis (after squaring the complex refractive index) yields the complex frequency-dependent dielectric functions of the sample $\hat{\epsilon}_{sam}(\omega)$ and the reference sample $\hat{\epsilon}_{ref}(\omega)$.

To get an indication of the accuracy of the THz technique and the extraction procedure, we have measured two identical samples of pure liquid H_2O , each contained in one of the cuvettes during measurement step *C* (positions **L** and **R**). The results for $\hat{n}_{R,\text{H}_2\text{O}}$ and $\hat{n}_{L,\text{H}_2\text{O}}$ are shown in Fig. 4.4. From this measurement we can conclude that the extracted refractive index is accurate to $<0.5\%$. Although the two samples are in excellent agreement with each other, it is still possible that the absolute refractive indices suffer from a systematic error. This could be caused by fluctuations in intensity or temperature that

could occur in between different times of the variable delay line that scans the THz pulse or in between the measurement steps *A*, *B* and *C*. It could also be caused by imperfections in alignment of the optical setup or the cuvettes (which could affect the effective cuvette chamber thickness that a THz pulse experiences). To account for these systematic errors, we always measure two samples, one of which has known dielectric properties and is used for calibration.

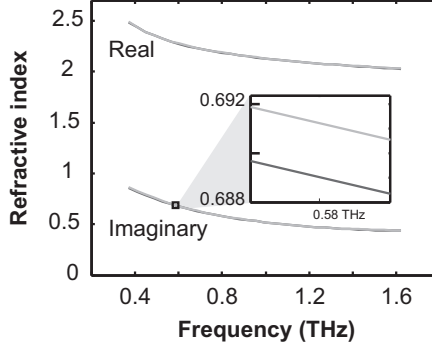


FIGURE 4.4. Extracted frequency-dependent complex refractive index for two samples of pure water. The inset shows a blowup to examine the accuracy, demonstrating that the relative uncertainty in the extracted refractive index is better than 0.5%.

CALIBRATION AND MODELING To obtain the calibrated dielectric properties of a sample, we first model the dielectric function of the reference sample. The reference is usually pure liquid water, for which we use a double-Debye dielectric relaxation model (see Chapter 2)

$$\epsilon_{\text{ref}}(\omega) = \frac{\epsilon_s - \epsilon_1}{1 + i\omega\tau_D} + \frac{\epsilon_1 - \epsilon_2}{1 + i\omega\tau_2} + \epsilon_\infty, \quad (4.8)$$

where the first and second term represent the two dielectric relaxation processes with relaxation strengths $S_1 = \epsilon_s - \epsilon_1$ and $S_2 = \epsilon_1 - \epsilon_2$ respectively, and time constants τ_D (the Debye time) and τ_2 . To compensate for insufficient frequency coverage of the THz setup, we fix the static dielectric constant ϵ_s to its literature value and fit the other parameters. We then construct the calibrated dielectric response of the reference sample $\hat{\epsilon}'_{\text{ref}}(\omega)$ by substituting the literature value for the Debye relaxation time τ'_D , instead of the experimentally determined τ_D . This allows us to find the calibration factors $C(\omega) = \frac{\hat{\epsilon}'_{\text{ref}}(\omega)}{\hat{\epsilon}_{\text{ref}}(\omega)}$. Finally, we construct the calibrated dielectric response of the sample according to $\hat{\epsilon}'_{\text{sam}}(\omega) = C(\omega) \cdot \hat{\epsilon}_{\text{sam}}(\omega)$.

In a variant of this calibration procedure, we do not construct a calibrated dielectric response, but use the Debye time that was found in the reference sample directly in the modeling of the other sample. We use this method if we are interested in extracting a calibrated value of ϵ_s (or equivalently S_1) for the sample under study. The procedure starts with the same modeling of the reference sample as before: with ϵ_s fixed to its literature value. In the fitting of the sample, we then also use Eq. 4.8, but now fix the Debye relaxation time to the value found in the reference sample. This yields the calibrated static dielectric constant ϵ'_s of the sample. The explicit assumption in this procedure is that the reference sample has the same Debye relaxation time as the sample under study. It follows from the literature that the effect of salts on the Debye relaxation time is small and has negligible dependence on the type of salt [24–26, 34, 175, 176], justifying this assumption for comparing different salt solutions of similar concentrations.

4.2 MEASUREMENTS IN THE VISIBLE AND INFRARED

The analysis of the pump-probe measurements in the visible and infrared is substantially different from the terahertz time-domain transmission measurements. In contrast to the terahertz measurements, in the infrared and visible measurements we do not resolve the time evolution of the optical field and measure only the time-integrated field intensity, meaning that phase changes are lost. As a result, we need a grating that disperses the different frequency components to extract spectral information. For the analysis of the different pump-probe measurements, we make a distinction between isotropic and anisotropic signals, where the latter only applies to the polarization-resolved infrared pump-infrared probe technique. In the visible pump-infrared probe and visible pump-visible probe, the pump and probe pulses are at magic angle ($\theta = 54.7^\circ$) with respect to each other, to be only sensitive to excited state relaxation.

4.2.1 ISOTROPIC DATA

We measure the pump-induced absorption $\Delta\alpha$ as a function of frequency ν and pump-probe delay time t

$$\Delta\alpha(t, \nu) = -\ln \left[\frac{I_{\text{probe}}(t, \nu)/I_{\text{ref}}(\nu)}{I_{\text{probe},0}(\nu)/I_{\text{ref},0}(\nu)} \right], \quad (4.9)$$

where, $I(t, \nu)$ is the intensity of the transmitted infrared probe light at frequency ν after pump-probe delay t ; the subscripts *probe* and *ref* refer to the probe and reference pulse, respectively; and the subscript 0 refers to measurement shots where the pump pulse was blocked by the 500 Hz chopper. As the reference pulse has no overlap with the pump pulse, it is clear that fluctuations

in the intensity of the probe light are compensated for by dividing through the intensity of the transmitted reference pulse. In the visible pump-visible probe measurements, where the induced absorptions are typically much larger, we do not make use of a reference pulse.

We are usually interested in the temporal evolution of different spectra that we can assign to different states of our system. As in Chapter 2, we only consider the case where the pump-probe delay time t is larger than the duration of the pump-probe cross-correlation. This means that we can ignore resonant and non-resonant $\chi^{(3)}$ contributions that only occur during pump-probe overlap. In some cases, different molecular states have very different spectra that are well-separated. In that case, the temporal evolution of those states can easily be determined. This is the case for our visible pump-infrared probe measurements. In these measurements, we can extract dynamics with time scales between approximately 200 fs and 1 ns. The lower limit is given by the cross-correlation between the pump and probe pulses that each have a duration of ~ 150 fs; the upper limit is given by the length of the variable delay line (~ 1 ns).

In many cases, the different molecular states have overlapping spectra, making it necessary to deconvolve these spectra in order to obtain their separate dynamics. Since our data contains noise, it is useful if some a priori knowledge exists on the system, e.g. from additional measurements. Naturally, it also helps if the different states have very different temporal evolutions. We discuss two cases: one where we assume that the system evolves from the state that is excited by the pump to an intermediate state and then to a final state (*cascading model*), and one where we assume that the system contains two species, which decay to two different final states (*parallel model*). The cascading model applies to the infrared pump-infrared probe measurements, where energy that resides initially in the excited OD-stretch mode, decays to an intermediate state, presumably a bending mode, leading to a shifted OD-stretch ground state spectrum. Subsequently, the energy ends up as heat, leading to the OD-stretch ground state spectrum of a slightly heated sample. The parallel model applies to the visible pump-visible probe measurements, where two different molecular species are present.

The two cases correspond to the energy diagrams as shown in Fig. 4.5. In the case of the cascading model, we find the following solution for $\Delta\alpha$ after solving the set of differential equations that describes the system

$$\begin{aligned} \Delta\alpha(t, \nu) &= S'(\nu) + S(\nu) \cdot e^{-k_1 t} + \left(\frac{S^*(\nu)k_1 - S'(\nu)k_2}{k_2 - k_1} \right) \cdot e^{-k_1 t} \quad (4.10) \\ &+ \left(\frac{S'(\nu)k_1 - S^*(\nu)k_1}{k_2 - k_1} \right) \cdot e^{-k_2 t} . \end{aligned}$$

Here, the transient spectra S , S^* and S' belong to the situation, where the

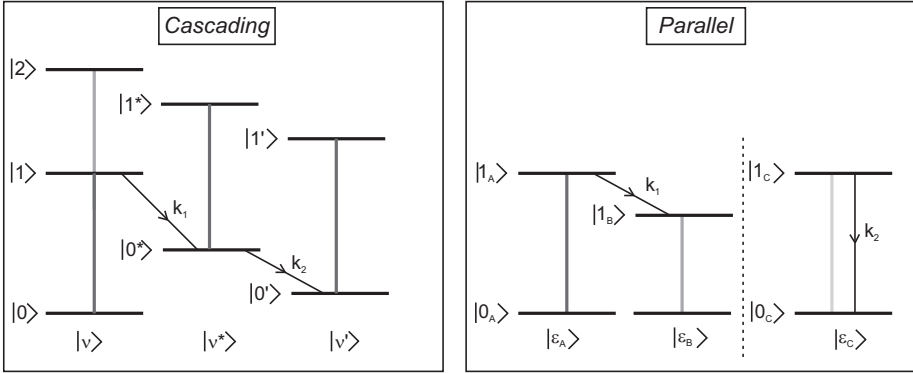


FIGURE 4.5. The energy diagram belonging to the cascading model with vibrational states $|\nu\rangle$ and the parallel model with electronic states $|\epsilon\rangle$, with the corresponding rate constants.

OD-stretch vibration resides in the excited state $|\nu_1\rangle$, the OD-stretch ground state while the energy resides in the intermediate state $|\nu_0^*\rangle$ and the OD-stretch ground state while the energy turned into heat $|\nu_0'\rangle$, respectively; and k_1 and k_2 are the relaxation rates for the OH-stretch vibration and the intermediate state, respectively. The occurrence of the transient spectra S^* and S' in Eq. 4.10 means that although the OD-stretch vibration has relaxed and the energy is in different modes, the OD-stretch mode is still affected, since otherwise the pump-induced change in absorption would be zero. For the heated end state this is clear, since the heated sample has a blue shifted OD-stretch absorption, which will result in a difference between the absorption of the excited sample and the unexcited sample. For the intermediate state, this means that the modes that have taken up the energy (presumably bend vibrations and librations) influence the cross section or absorption frequency of the OD-stretch vibration.

In the case of the parallel model, we obtain the following solution

$$\Delta\alpha(t, \nu) = S_B(\nu) + [S_A(\nu) - S_B(\nu)] \cdot e^{-k_1 t} + S_C(\nu) \cdot e^{-k_2 t}, \quad (4.11)$$

where the transient spectra S_A , S_B and S_C now correspond to three different electronic states of the molecule, which in the case of the photoacid HPTS are: the acidic form ROH $|\epsilon_A\rangle$, the basic form RO⁻ $|\epsilon_B\rangle$ and the acidic form while interacting with the environment ROH_{int.} $|\epsilon_C\rangle$, respectively; and k_1 and k_2 are the acid-base conversion rate (for the excited state) and the quenching rate, respectively. In the case where the molecule quenches, the excited state is lost and the molecule is back in its ground state, with no pump-induced change in absorption. Therefore we do not assign a transient spectrum to this state. In these measurements, the lifetime of the excitation is generally much longer (nanoseconds) than the dynamics that we are examining (tens of picoseconds),

so we are not concerned with excitation relaxation. Furthermore, heating of the sample is not sufficient to affect the electronic states.

These analytical solutions can now be compared to the experimental data to obtain the spectra and rate constants that best describe the data. The procedure is as follows:

1. Start with first guesses for the rate constants k_1 and k_2 ;
2. For each frequency pixel $\nu = \nu_i$, fit the measured absorption change to $\Delta\alpha(t, \nu_i)$ from Eq. 4.10 or Eq. 4.11 with fixed rate constants to obtain the amplitudes S_i , S_i^* and S_i' or $S_{A,i}$, $S_{B,i}$ and $S_{C,i}$;
3. Calculate the error-weighted, absolute difference in calculated and measured absorption change (summed over frequency and time) and repeat step 1 and 2 with different rate constants until the difference is minimized.

This procedure yields the best fitting spectra and rate constants, given the model. In the case of our measurements with a visible pump, these are the end results and a physical interpretation can be given for the spectra and the rate constants. In the case of the polarization-resolved infrared pump-infrared probe measurements, these results are the first step of the analysis, where we use the model of the isotropic data to determine how the heat signal grows in. Subsequently, we calculate the heat-corrected data, which are then used to extract the anisotropic signals.

4.2.2 ANISOTROPIC DATA

The analysis of the anisotropic data from the infrared pump-infrared probe measurements, can be done after the analysis of the isotropic data. The ingrowing heat spectrum (S' in Eq. 4.10), which we take to be isotropic, is subtracted from the experimental data with the appropriate time dynamics, to give the heat corrected pump-induced change in absorption. This is done for the two separate measurements with pump and probe polarizations mutually parallel and perpendicular and gives: $\Delta\alpha'_{\parallel}(t)$ and $\Delta\alpha'_{\perp}(t)$. These heat-corrected absorption changes are then used to construct the anisotropy $R(t)$ as a function of pump probe delay time t

$$R(t) = \frac{\Delta\alpha'_{\parallel}(t) - \Delta\alpha'_{\perp}(t)}{\Delta\alpha'_{\parallel}(t) + 2\Delta\alpha'_{\perp}(t)} . \quad (4.12)$$

The denominator in this equation is equal to the isotropic signal, i.e. the rotation-independent signal.

In pure water, the energy that resides in a stretch vibration can efficiently be transferred to a neighboring stretch vibration through resonant Förster

energy transfer (<100 fs [183]). This accepting stretch vibration will have a different orientation than the donating vibration and thus resonant Förster energy transfer leads to a randomization of the initial anisotropic distribution of excited vibrations. In diluted samples (4% D_2O in H_2O), the excited OD-stretch vibrations are more isolated, since they are surrounded by many OH groups, leading to a larger average distance between the OD groups and a much more inefficient resonant energy transfer [123]. Therefore, in the infrared pump-infrared probe measurements, we use these diluted systems, which has the additional benefit that the vibrational lifetime is longer. In pure water, the isotropic signal decays in a few hundred femtoseconds [93, 96], whereas in diluted systems (4% D_2O in H_2O) the lifetime is about 1.8 ps [134]. The longer lifetime allows the determination of the anisotropy dynamics over a longer time range. A final advantage of the dilution is that the amount of energy that is dumped in the system is distributed over a larger volume, which means that there is less heating of the sample.

For typical samples where we use diluted water (4% D_2O in H_2O), the anisotropy enables us to follow in time the reorientation of vibrationally tagged (OD-excited) HDO molecules. This makes this technique very suitable for studying water reorientation dynamics. The main advantage of this technique is the explicit sensitivity for the reorientation of water molecules in the system. The time window, where we can extract the anisotropy, ranges up to 10 ps after the pump excitation, making it mainly suitable for extracting reorientation time scales that are within this window.

5 TEMPERATURE DEPENDENCE OF WATER REORIENTATION

We study the temperature dependence of the molecular reorientation of HDO molecules in H₂O with polarization-resolved femtosecond mid-infrared pump-probe spectroscopy. With this technique we measure the decay time of the second order correlation function of the molecular reorientation. We find that the reorientation time changes from 4.8 ± 0.3 ps at 1 °C to 0.97 ± 0.05 ps at 70 °C. We compare the measurements with literature results of terahertz time-domain spectroscopy, where the Debye reorientation time is measured. From this comparison we obtain the ratio between the macroscopic Debye reorientation time and the first order microscopic reorientation time.

5.1 INTRODUCTION

The many anomalies of water find their origin in the structural arrangement of water, where water molecules form a connected network through hydrogen bonds. This network is not static, since molecular rearrangements take place continuously, typically on a picosecond (10^{-12} s, ps) timescale. The reorientation of liquid water involves three distinct processes. First of all, there is very fast 'single molecule' rotation that occurs for a very small fraction of undercoordinated water molecules, i.e. molecules that have very few or no hydrogen bonds [186]. The second process is formed by the ultrafast librational motions of the OH groups that keep the hydrogen bonds intact [43, 80]. This process occurs on an ultrafast timescale (< 200 fs [43, 109]) and leads to a partial ($\sim 20\%$) orientational scrambling. Recently, the temperature dependence of this librational contribution to the reorientation of liquid water was investigated in Ref. [109], where it was found that the relative contribution due to librational reorientation depends on the hydrogen bond strength, and that this dependence increases with temperature. The third process that can occur is the collective reorganization of the hydrogen-bond network, which involves the transient breaking and reformation of hydrogen bonds. In this Chapter, we focus our attention on this reorientation process. Numerical simulations recently showed that this reorientation of water molecules occurs in large-amplitude angular jumps (see Fig. 5.1), with a distribution of jump angles that is centered around 50° [81, 83]. This jump model differs from the previously commonly accepted

picture of subsequent small-amplitude angular rearrangements, known as the diffusion model.

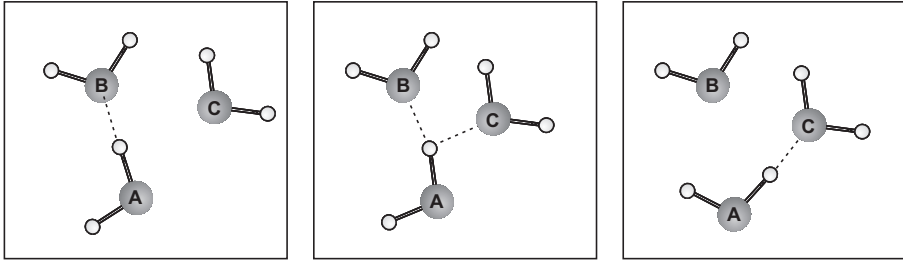


FIGURE 5.1. The molecular mechanism of water reorientation, following a jump mechanism (see Ref. [81]). After the approach of molecule **C** towards the hydrogen-bonded molecules **A** and **B** (left figure), a bifurcated state is formed, where molecule **A** is hydrogen-bonded both to molecule **B** and to molecule **C** (middle figure). After a large angle molecular jump, water molecule **A**, which was originally bonded to molecule **B**, is now bonded to molecule **C**.

Different experimental techniques have been employed to measure reorientation times of water molecules, like GHz dielectric relaxation (DR) [23], terahertz time-domain spectroscopy (THz-TDS) [139], nuclear magnetic resonance (NMR) [85, 97], optical Kerr-effect spectroscopy (OKE) [182] and femtosecond vibrational pump-probe spectroscopy (fs-IR) [109, 134, 157, 161]. Depending on how the observable is related to the angle between field and molecular dipole, these techniques are sensitive to the first or second order dipole correlation function [20]. DR and THz-TDS measurements probe the decay of

$$C^{(1)}(t) = \langle P^{(1)}[\vec{M}(0) \cdot \vec{M}(t)] \rangle \propto e^{-t/\tau_D} , \quad (5.1)$$

with $P^{(1)}[x]$ the first order Legendre polynomial in x , $M(t)$ the total dipole moment of the system at time t and τ_D the Debye relaxation time. The brackets $\langle \dots \rangle$ denote averaging of equilibrium initial conditions for the system, including angular displacement. The *macroscopic* Debye time τ_D is related to the *microscopic* first order molecular reorientation time $\tau_r^{(1)}$. Fs-IR, NMR and OKE probe the decay of

$$C^{(2)}(t) = \langle P^{(2)}[\vec{\mu}_i(0) \cdot \vec{\mu}_i(t)] \rangle \propto e^{-t/\tau_r^{(2)}} , \quad (5.2)$$

where $P^{(2)}[x]$ is the second order Legendre polynomial in x , $\vec{\mu}_i(t)$ is the dipole moment of the i th molecule at time t and $\tau_r^{(2)}$ denotes the second order reorientation time.

We use polarization-resolved femtosecond mid-IR vibrational pump-probe spectroscopy (fs-IR) to measure the second order orientational relaxation time

of HDO molecules in liquid H₂O solvent at temperatures from 1 to 70 °C. We compare our results for $\tau_r^{(2)}$ with literature values of τ_D from THz-TDS measurements [139] for H₂O for a similar temperature range. From this comparison we obtain the ratio between the macroscopic Debye time and the microscopic first order reorientation time. This ratio is a measure for the amount of dipole-dipole correlation between different water molecules and local field effects.

5.2 EXPERIMENTAL

We measure the decay of the anisotropy of the OD-stretch vibration of HDO dissolved in H₂O with polarization-resolved pump-probe spectroscopy. This technique uses two ultrafast infrared pulses (duration <150 fs), where the first (pump) pulse excites the OD-stretch vibration of a subset of HDO molecules. Mainly OD groups that are aligned in the same direction as the polarization of the pump pulse are excited. After a variable delay, a second (probe) pulse measures the number of excited OD groups. This is done for probe polarization parallel with respect to the pump polarization and probe polarization perpendicular to the pump polarization. The normalized difference between the parallel and perpendicular signal is the anisotropy parameter, whose time dependence reflects the orientational decay of the vibrationally tagged water molecules.

The fs-IR setup (see Chapter 3, Fig. 3.5) that is used for measurements of molecular reorientation dynamics employs a commercial Ti:sapphire regenerative amplified laser system (Spectra-Physics Hurricane) that delivers 800 nm pulses with a duration of ~ 110 fs with an energy of 1 mJ at a rate of 1 kHz. Part of this light is used to pump a white-light seeded optical parametric amplifier (OPA) based on a β -barium borate (BBO) crystal. The idler signal output from the OPA, with a wavelength of 2 μm , is frequency doubled in a second BBO crystal to 1 μm and then difference-frequency mixed with the remaining 800 nm light in a potassium niobate crystal (KNB). This produces ~ 5 μJ of 4 μm (2500 cm^{-1} , resonant with the OD-stretch vibration) light with a pulse duration of ~ 150 fs.

The pump-probe experiment is conducted by sending part of the 4 μm light into the pump branch and part into the probe branch of the set-up. Both pump and probe pulses are focused onto the same spot in the sample. Every other pump pulse is blocked by a 500 Hz chopper, so that every consecutive probe pulse either experiences an excited or a non-excited sample. The difference between these consecutive signals gives the pump-induced change in absorption of the sample $\Delta\alpha$. A reference pulse that is focused on a different spot on the sample allows compensation for fluctuations in the probe intensity. The absorption of the probe and reference pulses is measured with a 2×32 liquid-nitrogen cooled mercury-cadmium-telluride (MCT) array spectrometer

(Infrared Associates), resulting in $\Delta\alpha(\nu)$. A delay stage that controls the relative delay between pump and probe pulse is used to monitor the dynamics of the pump-induced change in absorption $\Delta\alpha(\nu, t)$, where t is the pump-probe delay time.

To measure reorientation dynamics, a $\lambda/2$ -plate is placed in the pump path in combination with a motor-controlled polarizer in the probe path after the sample. This makes it possible to detect the induced absorption for a probe polarization parallel to the pump polarization ($\Delta\alpha_{\parallel}$) and the signal measured with a probe polarization perpendicular to the pump ($\Delta\alpha_{\perp}$). We use $\Delta\alpha_{\parallel}$ and $\Delta\alpha_{\perp}$ to construct the isotropic signal, which is independent of reorientation: $\Delta\alpha_{\text{iso}} = \frac{1}{3}(\Delta\alpha_{\parallel} + 2\Delta\alpha_{\perp})$. We also construct the anisotropic signal or anisotropy, which is independent of vibrational energy relaxation: $R = (\Delta\alpha_{\parallel} - \Delta\alpha_{\perp})/3\Delta\alpha_{\text{iso}}$. $R(t)$, where t is time, is proportional to the second order orientational correlation function $R(t) = \frac{2}{5}C^{(2)}(t)$. The exponential decay rate of $R(t)$ gives the second order reorientation time $\tau_r^{(2)}$ (see also Section 2.3).

The sample is a solution of 8% HDO in H₂O solvent (4% D₂O in H₂O). We use an isotopically diluted sample to avoid the decay of the anisotropy as a result of Förster energy transfer between the stretch vibrations, which quickly randomizes the orientation (<100 fs [183]). The study of the anisotropy of the OD vibration of HDO:H₂O has the advantage over the study of the OH vibration of HDO:D₂O that the vibrational relaxation of the OD vibration is slower (1.8 ps [75]) than that of the OH vibration (750 fs, [185]). The anisotropy dynamics can thus be measured over a longer time interval for the OD vibration than for the OH vibration. A shorter lifetime would introduce more noise to the anisotropic signal at a shorter pump-probe delay time. The sample is placed between CaF₂ windows that are separated by a 25 μm spacer. The sample cell is mounted in a temperature controlled sample holder with a Peltier element that allows cooling and heating.

5.3 RESULTS AND DISCUSSION

5.3.1 ISOTROPIC SIGNAL

To obtain the anisotropy dynamics of the excitation, the measured data $\Delta\alpha_{\parallel}$ and $\Delta\alpha_{\perp}$ have to be corrected for the time-dependent thermalization signal, as described in detail in Section 4.2.1. The time dynamics of this contribution to the signal can be obtained from a detailed investigation of the isotropic signal. In Fig. 5.2, the isotropic pump-induced absorption spectrum $\Delta\alpha_{\text{iso}}(\nu, t)$ is shown for a number of pump-probe delay times for temperatures of 10 °C (**A**) and 60 °C (**B**). The dip centered at $\sim 2500 \text{ cm}^{-1}$ is due to the bleach of the $0 \rightarrow 1$ transition of the OD-stretch vibration and stimulated emission from the first excited state. All data are modeled with the cascading energy relaxation

model as described in Section 4.2.1 and Ref. [134]. In this model, the energy from the OD-stretch vibration is transferred through an intermediate state (presumably a bending mode) to a thermal end level (lower energy modes). The model contains two global fit parameters: τ_1 (first excited state OD stretch \rightarrow intermediate state) and τ_2 (intermediate state \rightarrow thermal end state). A least square fit is conducted for the whole spectrum at each delay time to find the two timescales. The fits to the data using this model are shown in Fig. 5.2 (solid lines). The quality of the fits is evident and the same over the entire temperature range, indicating that the vibrational relaxation mechanism is temperature-independent.

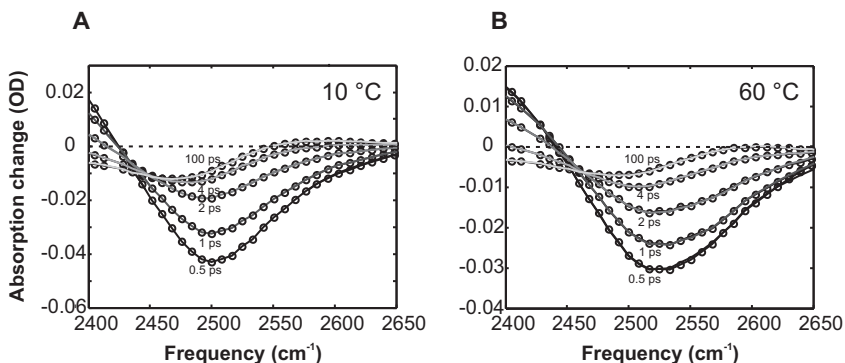


FIGURE 5.2. Pump-induced absorption spectrum $\Delta\alpha(\nu, t)$ at different delay times (0.5, 1, 2, 4 and 100 ps) for 10 °C (A) and 60 °C (B). The solid lines are fits to the model. A broadening is observed at higher temperature in accordance with linear absorption spectra.

The fit parameters, τ_1 and τ_2 , are determined for all temperatures. In Fig. 5.3 the values of these parameters are presented as a function of temperature. The value of τ_1 increases for increasing temperature, an effect that has also been observed for pure liquid water [95] and HDO in D₂O [185]. The slowing down of vibrational energy relaxation in pure H₂O and in HDO:D₂O with temperature is likely due to the decrease of the spectral overlap between the overtone of the bending mode and the excited stretch mode for increasing temperatures [87]. The decrease in spectral overlap is mainly caused by a blue shift of the stretch vibration for higher temperatures, which is in turn the result of a decrease in hydrogen bond strength [116]. For the OD-stretch vibration of HDO in H₂O, a similar blue shift of the stretch frequency occurs [37]. In the case of HDO:H₂O vibrational energy relaxation will follow a different relaxation path, since the overtone of the bending mode has a higher frequency than the OD stretch. The relaxation path for HDO:H₂O likely involves relaxation to the fundamental bend mode and additional excitation of lower energy modes, such as librations or hydrogen-bond stretching [39, 134]. The shift to higher frequencies of

the OD-stretch vibration with increasing temperature increases the energy gap to the bending mode, which likely forms the origin of the observed increase of τ_1 .

After the relaxation is complete, the energy of the pump pulse thermalizes, leading to an increase of the sample temperature by about 1 °C. The spectrum observed at large delays (see Fig. 5.2 at a pump-probe delay time of 100 ps) represents the difference of the absorption at this elevated temperature and the absorption at the initial temperature (no pump excitation). We have measured the linear absorption spectra for a wide range of temperatures and verified that the frequency dependence of the thermal end level is in correspondence with the difference in the linear spectra of the elevated and initial temperature (see Fig. 5.4).

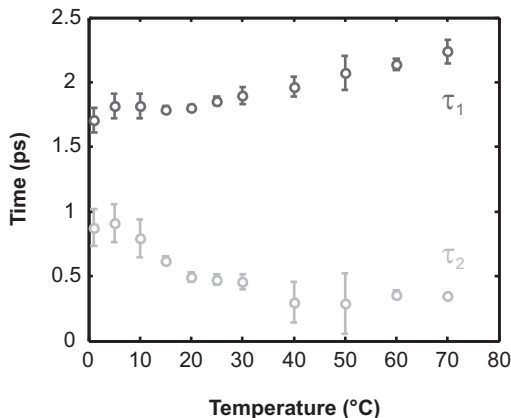


FIGURE 5.3. The values for τ_1 and τ_2 that were found using the fitting procedure (error bars represent 95 % confidence intervals). Upon increasing the temperature, τ_1 increases, whereas τ_2 decreases.

The timescale τ_2 represents the time constant of the relaxation of the intermediate state to low energy modes. In Fig. 5.3 it can be seen that τ_2 becomes shorter for increasing temperature, which implies that there is an increased coupling of the intermediate level to lower frequency modes with increased temperature [115].

5.3.2 ANISOTROPIC SIGNAL

In Fig. 5.5, the anisotropic decay data are shown for six different temperatures (5, 15, 30, 40, 50 and 70 °C). The signal for each temperature is averaged

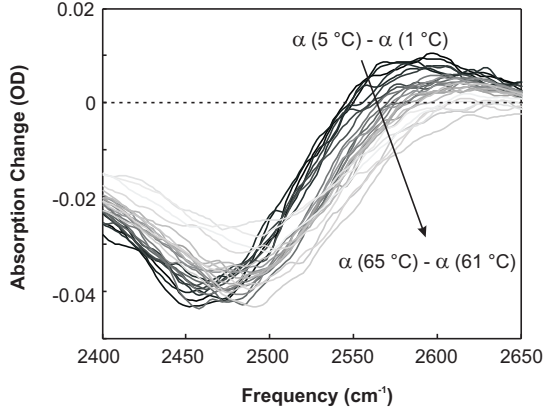


FIGURE 5.4. The difference between linear spectra taken at temperature $T + 4$ °C and linear spectra at temperature T for T between 1 and 61 °C. We estimated that our pump excitation dumps an amount of energy in the system to increase the temperature by about 1 °C. The differential spectrum from our pump-probe measurements is therefore in good quantitative agreement with the results from the linear spectra at different temperatures.

between 2475 and 2525 cm^{-1} . Clearly the anisotropy decays faster with increasing temperature. The anisotropy decays are fit to a mono-exponential function, resulting in a reorientation time $\tau_r^{(2)}$ that decreases from 4.8 ± 0.3 ps at 1 °C to 2.6 ± 0.1 ps at room temperature to 0.97 ± 0.05 ps at 70 °C. Here, we do not take into account the orientational dynamics that occur in the first 200 fs (Förster transfer and librational motion). The observation of a decreasing orientational relaxation time for an increasing temperature agrees well with earlier observations using DR [23], THz-TDS [139] and NMR [85,97] (see Fig. 5.6).

The observed speedup by a factor of 5 in the temperature range from 1 to 70 °C thus indicates a strong increase of the hydrogen-bond dynamics. This speedup can be explained from the overall weakening of the hydrogen bonds.

We compare our (second order, microscopic) fs-IR reorientation data with (first order, macroscopic) THz-TDS measurements for H_2O by Rønne and Keiding [139]. In an ideal first order correlation experiment one would measure the first order molecular correlation function $C_{i,i}^{(1)}(t) = \langle P^{(1)}[\vec{\mu}_i(0) \cdot \vec{\mu}_i(t)] \rangle$. However since THz-TDS measures the correlation function of the total dipole moment of the system \vec{M} , additional cross-correlation terms show up: $C_{i,j}^{(1)}(t) = \langle P^{(1)}[\vec{\mu}_i(0) \cdot \vec{\mu}_j(t)] \rangle$ (see also Eq. 5.1), where i and j represent different molecules. Due to these cross-correlations, (THz) dielectric relaxation measurements probe

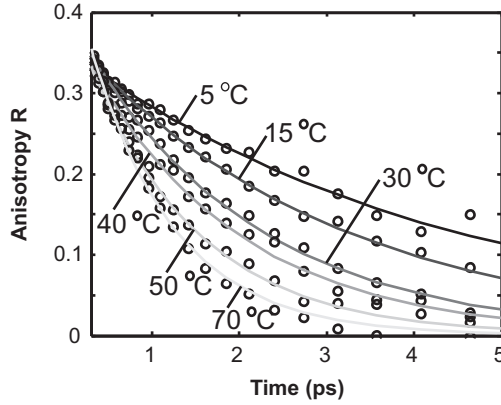


FIGURE 5.5. The decay of the anisotropy vs. pump-probe delay time for different temperatures (5, 15, 30, 40, 50 and 70 °C), showing a clear decrease in reorientation time for higher temperature. The lines are mono-exponential fits to the data and yield the second order reorientation time $\tau_r^{(2)}(T)$.

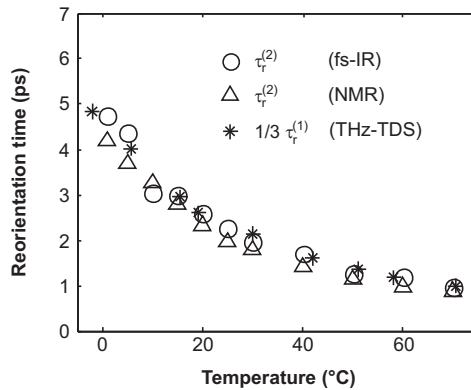


FIGURE 5.6. The reorientation time as a function of temperature, as measured with fs-IR, THz-TDS (from Ref. [139]) and NMR (from Ref. [97]).

the macroscopic τ_D instead of the microscopic $\tau_r^{(1)}$. The amount of dipole-dipole correlation determines the ratio between τ_D and $\tau_r^{(1)}$. This ratio is furthermore determined by local field effects: The microscopic electric field that a water molecule experiences might be different from the applied macroscopic electric field. We use the following equation to extract the ratio

$$\kappa = \frac{\tau_r^{(1)}}{\tau_D} = \frac{\tau_r^{(1)}}{\tau_r^{(2)}} \cdot \frac{\tau_r^{(2)}}{\tau_D} . \quad (5.3)$$

Here we use our experimental data for $\tau_r^{(2)}$ and literature data for τ_D from Ref. [139]. The ratio $\tau_r^{(1)}/\tau_r^{(2)}$ is known from literature and has a value ranging from 2.5 - assuming reorientation behavior according to the jump model - to 3.0 - assuming diffusive reorientation [81]. The results are shown in Fig. 5.7 and give experimental evidence that the contribution of cross-correlation terms and local field effects is not very strong in neat water. We find a value of $\kappa = 0.74 - 0.94$, where the former represents the case of large-angular jump reorientation and the latter the case of diffusive reorientation. These values include a 3% uncertainty contribution that has been estimated from our experimental data. Theory and simulation have resulted in similar values of $\kappa \approx 0.9$ [20, 177] and ~ 0.7 [48], but also smaller values have been found such as 0.5 [83] or ~ 0.125 [6].

Many physical properties of water show an anomalous temperature dependence, examples of which are the density, viscosity and specific heat. In Fig. 5.7, the ratio $\kappa = \tau_r^{(1)}/\tau_D$ is determined for the whole temperature range. It can be seen that the ratio is not temperature-dependent. We further observe that the ratio, where diffusive reorientation is assumed, and the ratio, where large-angular jump reorientation is assumed, are well-separated. This is a strong indication that the reorientation mechanism is not temperature-dependent, in accordance with recent simulation results [83]. It also confirms that the decay time of the correlation function as measured by fs-IR spectroscopy corresponds to the same collective reorientation process as is probed by (THz) dielectric relaxation measurements.

5.4 CONCLUSION

We used polarization-resolved femtosecond mid-IR pump-probe spectroscopy to measure the second order reorientation time of HDO molecules in liquid H₂O over a temperature range between 1 and 70 °C. In the isotropic (reorientation-free) data we see an increase of the relaxation time constant τ_1 and a decrease in the thermalization time constant τ_2 . The anisotropic (relaxation-free) data show a fivefold decrease in reorientation time between 1 and 70 °C.

We compare the second order reorientation time $\tau_r^{(2)}$ with THz time-domain spectroscopy measurements of τ_D from Ref. [139]. These time constants are associated with the same collective reorientation process of hydrogen-bonded water molecules. From this comparison, we find that the ratio $\tau_r^{(2)}/\tau_D$ does not depend on temperature, which indicates that the reorientation mechanism does not change with temperature. The ratio $\kappa = \tau_r^{(1)}/\tau_D$ lies between 0.74 and

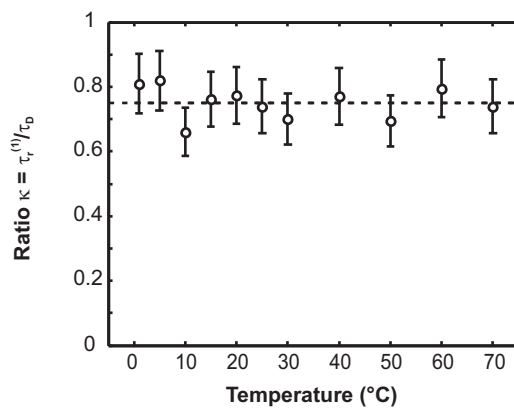


FIGURE 5.7. The temperature dependence of the ratio $\tau_D/\tau_r^{(1)}$, assuming large-angular jump reorientation.

0.94, which points towards a fairly weak effect of the dipole-dipole correlations of water molecules and local field effects on the Debye relaxation time τ_D in neat water.

6 SEMI-RIGID HYDRATION AND COOPERATIVITY IN ION SOLUTIONS

Despite prolonged scientific efforts to unravel the effects of ions on the structure and dynamics of water, many open questions remain, in particular concerning the spatial extent of this effect (how many water molecules are affected) and the origin of ion-specific effects. A combined terahertz and femtosecond infrared spectroscopic study of water dynamics around different ions reveals that the effect is usually limited to the first hydration shell of water molecules surrounding an ion, where cations and anions lock different degrees of freedom: semi-rigid hydration. In certain cases – when strongly hydrated cations and anions are combined – large structures (~ 18 H₂O's) are formed in between the ions, where the water dynamics are locked. This shows that the effect of ions and counterions on water can be strongly interdependent and non-additive.

6.1 INTRODUCTION

The properties of solutions of ions in water are of relevance for a wide range of systems, including biological environments [78] and atmospheric aerosols [65]. Interestingly, even for simple binary solutions the effect of ions on the structure and dynamics of water has been the subject of ongoing debate [45, 101, 166]. Key questions concerning ion effects on water pertain to the number of water molecules that are affected, and how the different degrees of freedom of these water molecules are influenced.

During the last decade a variety of measurement techniques has provided evidence that ions primarily have an effect on the structure and dynamics of the first solvation shell of water molecules directly surrounding the ion. This evidence consists of *structural* measurements of ion hydration using neutron and X-ray diffraction [36, 100], X-ray absorption spectroscopy [29] and infrared and Raman spectroscopy [150]. Information on the ion effects on water *dynamics* has been mainly obtained from femtosecond time-resolved infrared vibrational spectroscopy (fs-IR) [112, 119, 121] and optical Kerr effect spectroscopy [169].

These reports support the notion that the effect of ions on water is largely limited to the first solvation shell. A different dynamical technique, dielectric relaxation (DR), also showed that for many different cations and anions, the effect is limited to the first solvation shell [26,34,66,176]. However, for certain ion combinations an effect beyond the first solvation shell was observed [24,25,175].

Here, we study the effect of ions on water using terahertz dielectric relaxation (DR) spectroscopy and femtosecond vibrational infrared spectroscopy (fs-IR). It turns out that these techniques are complementary, in that they are sensitive to water reorientation dynamics along different axes of the water molecule. Moreover, the ability to independently resolve water reorientation along different directions helps to uncover previously unappreciated cooperativity between hydrated cations and anions. We study dissolved salts, containing various combinations of ions that have different charge densities and water affinities. For specific combinations of cations and anions we observe dynamic hydration effects that extend well beyond the first structural solvation shell.

6.2 EXPERIMENT AND ANALYSIS

6.2.1 THZ SPECTROSCOPY

We perform dielectric relaxation (DR) spectroscopy using a terahertz time-domain spectroscopy (THz-TDS) setup. This setup (see Chapter 3, Fig. 3.4) is based on THz generation and detection in ZnTe non-linear crystals, using 800 nm pulses with a duration of ~ 150 fs. The time-dependent electric field strengths of the THz pulses (~ 3 ps) that are transmitted through the sample are measured by means of electro-optic sampling with a variably delayed pulse of 800 nm light with a duration of ~ 150 fs in a second ZnTe crystal. By comparison of the THz pulse that is transmitted through an empty cuvette and through a cuvette filled with the sample, we can extract the complex refractive index $\hat{n} = n - i\kappa$. Here n is the regular refractive index and κ is the extinction coefficient. We determine the frequency-dependent complex dielectric response $\hat{\epsilon}(\omega) = \hat{n}^2$ for a number of salt solutions. In each measurement a sample is measured quasi-simultaneously with a reference sample. We employ a mechanical device that alternatively positions the sample and the reference sample (contained in cuvettes that have chambers with an optical path length of $103 \pm 0.5 \mu\text{m}$) in the THz beam. This approach minimizes the effect of fluctuations in THz intensity and temperature as noise sources. We measure the following combinations of salt solutions: $\text{MgCl}_2\text{-CsCl}$, LiCl-CsCl , $\text{Cs}_2\text{SO}_4\text{-CsCl}$, $\text{Mg}(\text{ClO}_4)_2\text{-CsCl}$ and $\text{MgSO}_4\text{-Cs}_2\text{SO}_4$. In most cases, the salt CsCl is chosen as a reference sample, since its dielectric properties are known and the ions Cs^+ and Cl^- have a negligible hydration effect according to GHz dielectric relaxation measurements [34]. We have measured other additional combinations of samples and reference samples, to assure consistency. We

compare samples with similar concentrations.

Molecular reorientation processes lead to dielectric relaxation, i.e. the anomalous dispersion of the dielectric constant and the accompanying absorption of electromagnetic energy [19, 20], as explained in Section 2.2. The dielectric response of pure water has shown evidence for two molecular reorientation processes [46, 68, 138–140, 186]

$$\hat{\epsilon}(\omega) = \frac{S_{1,\text{pure}}}{1 + i\omega\tau_{\text{D,pure}}} + \frac{S_{2,\text{pure}}}{1 + i\omega\tau_{2,\text{pure}}} + \epsilon_{\infty} \quad (6.1)$$

At room temperature, $S_{1,\text{pure}} \approx 75$ and $S_{2,\text{pure}} \approx 1.8$ and the corresponding time constants are $\tau_{\text{D}} \approx 8$ ps and $\tau_2 \approx 250$ fs [186]. The former time constant is associated with the reorientation of water, which is a concerted process that occurs through a molecular jump mechanism [81, 83]. The latter time constant is generally ascribed to the reorientation of undercoordinated water molecules [186]. The dielectric constant in the high frequency limit is given by ϵ_{∞} .

In previous dielectric relaxation studies of aqueous salt solutions, it was observed that a certain number of water molecules shows very slow reorientation dynamics, whereas for the remaining water molecules the orientational dynamics are similar to bulk liquid water [24–26, 34, 66, 175, 176]. Also in computer simulations it was found that a fraction of water remains that is unaffected by the presence of the ions [82, 92]. In analyzing the THz data, we thus follow the literature and identify two sub-ensembles of water molecules in ionic solution: those whose dynamics are predominantly unaffected by the presence of ions (bulk-like water), and those whose dynamics are affected (hydration shell water). Including the conductivity σ due to ions (see Eq. 2.13), we obtain the following dielectric function of the ionic solution

$$\hat{\epsilon}(\omega) = \frac{S_1}{1 + i\omega\tau_{\text{D}}} + \frac{S_2}{1 + i\omega\tau_2} + \frac{\sigma}{i\omega\epsilon_0} + \epsilon_{\infty} \quad (6.2)$$

The addition of ions to water has an effect on the relaxation strength S_1 , since fewer water molecules contribute to this process. In total, there are three effects by which ions can lead to a lowering of $S_{1,\text{pure}}$ by an amount ΔS_1 (depolarization): (i) the solution’s water concentration is slightly lower than the pure water case, resulting in a small overall lowering of the dielectric response (dilution effect); (ii) due to the interaction of the electric field of an ion with a number of water molecules in the vicinity of an ion, these water molecules can no longer participate in the relaxation process with τ_{D} (static depolarization); and (iii) due to ions that move in the driving field, water molecules are caused to reorient in a direction opposite to the driving field (kinetic depolarization) [60, 66]. The static and kinetic depolarization effects

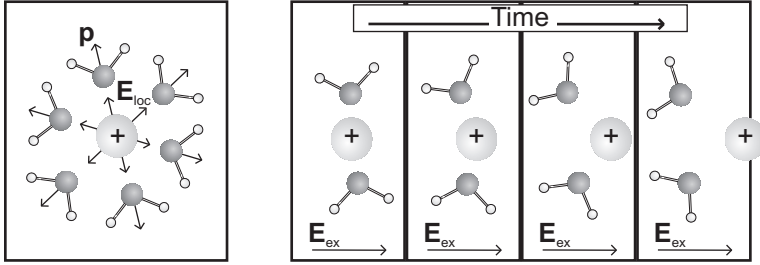


FIGURE 6.1. Schematic representation of the static (left figure) and kinetic (right figure) depolarization effects of a cation on the surrounding water molecules. Here, \vec{p} is the dipole moment of a water molecule, \vec{E}_{loc} is the local electric field produced by the ion and \vec{E}_{ex} is the external driving field, i.e. the THz field.

are schematically depicted in Fig. 6.1.

In ionic solutions the Debye time τ_D might be somewhat different from the value in pure water $\tau_{D,pure}$. However, this effect was found to have a negligible dependence on the nature of the ions [34, 175, 176]. The effect is furthermore small: it results in a τ_D that is $\sim 10\%$ lower for a 1 molar solution, compared to pure water.

In analyzing the data, we use the parameter $S_{1,ref}$ for the reference salt solution of CsCl from Ref. [34] and literature values for the ion conductivities of the solutions CsCl, MgCl₂, LiCl, Cs₂SO₄, MgSO₄ and Mg(ClO₄)₂ from Refs. [4, 17, 24, 25, 34, 170, 175]. For each sample, we fix τ_D to the value that was found for the accompanying reference sample. This allows us to extract the relaxation strength S_1 of a salt solution. For details on the extraction and modeling of the dielectric data from THz measurements, see Section 4.1.2. Finally, through the relaxation strength S_1 of a salt solution, we calculate the hydration number of the ions in the solution.

The hydration number of an ion, is defined as the number of moles of water molecules per mole dissolved salt, which no longer participate in dielectric relaxation due to the presence of the ion (effect *ii* above). These hydration numbers have been extracted successfully for a large number of ionic solutions by Buchner et al. [24–26, 34, 175, 176]. We start with the extracted relaxation strength S_1 of a salt solution and obtain the total decrease of the relaxation strength of a salt solution compared to pure water: $\Delta S_1 = S_1 - S_{1,pure}$. This number is negative, since it is a reduction of the induced polarization, i.e. a depolarization. This depolarization is subsequently corrected for the effect of kinetic depolarization (effect *iii* mentioned above), which is proportional to the conductivity σ and depends on the salt concentration c [26, 66]

$$\Delta S_{1,\text{kin.dep.}}(c) = -\sigma(c) \cdot \frac{2\tau_{\text{D,pure}}}{3} \frac{\epsilon_{\text{s,pure}} - \epsilon_{\infty}(c)}{\epsilon_{\text{s,pure}}\epsilon_0} . \quad (6.3)$$

Here, $\epsilon_{\text{s,pure}}$ is the static permittivity of pure water and $\epsilon_{\infty}(c)$ the high frequency limit of the permittivity for the salt solution. After having corrected the total depolarization ΔS_1 for the kinetic depolarization, we obtain the corrected depolarization $\Delta S'_1$. This number can subsequently be translated into the hydration number, as measured with THz DR spectroscopy, $N_{\vec{p}}$, using [54]

$$N_{\vec{p}}(c) = \left(c_{\text{s}} - \frac{S_{1,\text{pure}} + S_{2,\text{pure}} + \Delta S'_1}{S_{1,\text{pure}} + S_{2,\text{pure}}} c_0 \right) / c \quad (6.4)$$

In this equation, c_{s} is the concentration of solvent water molecules in the solution and c_0 represents the concentration of water molecules of pure water (~ 55 mol/L). The subscript \vec{p} refers to the molecular vector whose reorientation is monitored: the dipole moment of the water molecules. In Eq. 6.4, the dilution effect of the ionic solution (effect i mentioned above) is taken into account through the concentrations c , c_{s} and c_0 . We point out that the hydration number is a dynamics property and is therefore distinct from the structural concept of solvation shells. Solvation shells are often defined in terms of the distance distribution of the water molecules from the center of the ion, but as such do not present information on the dynamics of the water molecules.

6.2.2 FS-IR SPECTROSCOPY

Complementary to DR measurements, we use femtosecond time-resolved infrared vibrational spectroscopy (fs-IR) measurements. The setup of these experiments is schematically depicted in Chapter 3, Fig. 3.5. This technique allows the direct study of the reorientational dynamics of individual water molecules with high temporal resolution (~ 150 fs). In these experiments, we excite the OD-stretch vibration of a subset of HDO molecules in H_2O (4% D_2O in H_2O). Molecules with their OD group preferentially aligned along the polarization axis of the excitation (pump) pulse are most efficiently tagged. By interrogating, using a second laser (probe) pulse, the number of tagged OD groups that are oriented parallel and perpendicular to the excitation axis, the rotation of these groups can be followed in time. To this purpose, we measure the pump-induced absorption change as a function of frequency and pump-probe delay for a probe pulse that is polarized parallel ($\Delta\alpha_{\parallel}$) and a probe pulse that is polarized perpendicular ($\Delta\alpha_{\perp}$), with respect to the pump pulse. We use $\Delta\alpha_{\parallel}$ and $\Delta\alpha_{\perp}$ to construct the isotropic signal, which is independent of reorientation

$$\Delta\alpha_{\text{iso}} = \frac{1}{3}(\Delta\alpha_{\parallel} + 2\Delta\alpha_{\perp}) . \quad (6.5)$$

To obtain the anisotropy dynamics of the excited OD-stretch dipole vectors, the measured data $\Delta\alpha_{\parallel}$ and $\Delta\alpha_{\perp}$ are corrected for the time-dependent thermalization signal. The temporal evolution of this contribution to the signal is obtained from a detailed investigation of the spectral dynamics of the isotropic signal. All data are modeled with the cascading energy relaxation model described in Section 4.2.1 and Ref. [134]. In this model the energy from the OD-stretch vibration is transferred through an intermediate state (presumably the bending mode) to a thermal end level (lower energy modes). The model contains two main fit parameters: τ_1 (first excited state OD-stretch \rightarrow intermediate state) and τ_2 (intermediate state \rightarrow thermal end state). A least squares fit is conducted for the whole spectrum at each delay time to find the two time scales that constitute the best fit. In Fig. 6.2, we show measurements and the results of the fitting procedure for the isotropic data of different sulfate-containing salt solutions. Clearly, the vibrational lifetime depends only weakly on the salt concentration.

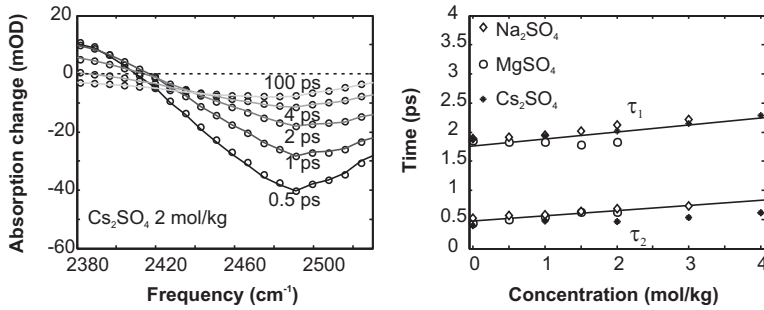


FIGURE 6.2. A typical pump-induced absorption spectrum for a number of pump-probe delay times for a 2 mol/kg solution of Cs_2SO_4 (A). (B) The fit results for the time scales τ_1 and τ_2 as a function of ion concentration, after modeling the energy relaxation. The lines are guides to the eye.

We use the heat-corrected data $\Delta\alpha'_{\parallel}(t)$ and $\Delta\alpha'_{\perp}(t)$ to construct the anisotropy $R(t)$, where t is the pump-probe delay time

$$R(t) = \frac{\Delta\alpha'_{\parallel}(t) - \Delta\alpha'_{\perp}(t)}{\Delta\alpha'_{\parallel}(t) + 2\Delta\alpha'_{\perp}(t)}. \quad (6.6)$$

The decay of the anisotropy represents the orientational relaxation of the OD groups of the water molecules in the system. In neat $\text{HDO}:\text{H}_2\text{O}$, the time scale of the decay of the anisotropy corresponds well within a constant scaling factor to the relaxation time $\tau_{\text{D,pure}}$ of pure water, as measured with THz DR

spectroscopy. This was shown for a large range of temperatures in Chapter 5.

In aqueous salt solutions, we describe the anisotropy decay using a bimodal model, analogous to the DR measurements: the slow time constant and the associated fraction of slow hydration shell water are obtained from a double exponential fit to the anisotropy decay. Here the bulk-like time constant is determined from independent measurements of the reorientation time of neat water ($\tau_{\text{bulk}} = 2.6 \pm 0.1$ ps at room temperature). The slow component represents a weighted average of water molecules that have in common that they reorient more slowly than the water molecules in bulk liquid water. Hence, the data are fit with the following model

$$R(t) = A_{\text{bulk}} \cdot e^{-t/\tau_{\text{bulk}}} + A_{\text{shell}} \cdot e^{-t/\tau_{\text{shell}}} . \quad (6.7)$$

For all studied solutions ($\text{Mg}(\text{ClO}_4)_2$ up to 2 mol/kg, LiI up to 4 mol/kg, LiCl up to 4 mol/kg, Cs_2SO_4 up to 4 mol/kg, Na_2SO_4 up to 3 mol/kg and MgSO_4 up to 2 mol/kg), we found good agreement with a fixed slow water time constant of $\tau_{\text{shell}} = 10$ ps. We point out that exchange of water molecules inside and outside the hydration shell can occur. However, this time scale is slow (tens of picoseconds [74]) in comparison to the time scale of the molecular reorientation of neat water [134]. Hence, a water molecule outside the solvation shell has long reoriented before it is exchanged with a water molecule in the solvation shell. As a result, the dynamics of the water molecules outside the solvation shells are observed well separated from the dynamics of the water molecules inside the solvation shell. For water in the solvation shell, the exchange time is also too long to obtain an averaging of solvation shell and bulk behavior. The residence time of the solvation shell may however contribute to the measured reorientation time scale. When the water molecule leaves the shell, it will likely also reorient. Hence the reorientation time of the hydration shell does present a lower limit for the residence time of the water molecules in the solvation shell. For all studied ions the residence time is too long [74] to make the slowly reorienting water molecule into a bulk-like water molecule. Hence, the value of the hydration number is not dependent on the time scale of the exchange.

In analogy to the DR measurements, the slow water fraction as measured with fs-IR can be translated into a hydration number $N_{\vec{\mu}}$. This corresponds to the number of moles of slowly reorienting OD groups (with transition dipole moment $\vec{\mu}$) per mole dissolved salt

$$N_{\vec{\mu}} = \frac{A_{\text{shell}}}{A_{\text{bulk}} + A_{\text{shell}}} \times 2c_s , \quad (6.8)$$

where the factor 2 is due to the fact that there are two OD groups per water molecule.

6.3 RESULTS

We first present the results of DR spectroscopy of different dissolved salts. In the inset of Fig. 6.3A, we show THz pulses as transmitted through 0.5 mol/kg solutions of Cs_2SO_4 , MgSO_4 and through a reference solution of CsCl [34]. Generally, THz pulses are delayed as a result of refraction and experience a decrease in amplitude as a result of absorption (see also Chapters 2 and 4). In Fig. 6.3A, we show the imaginary part of the extracted dielectric function ϵ , which is associated with absorption of electromagnetic radiation by water molecules.

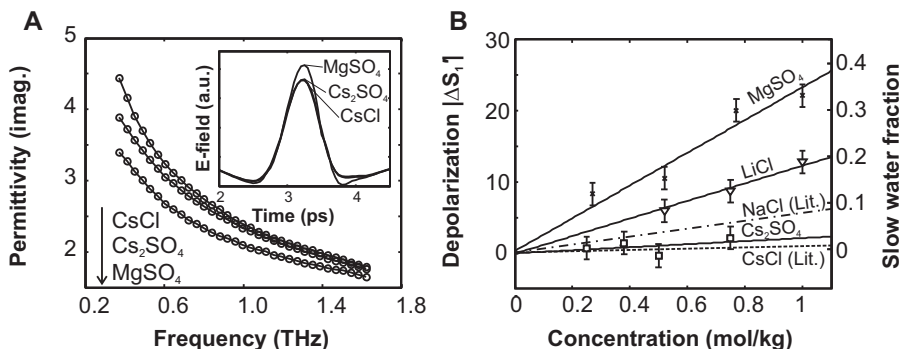


FIGURE 6.3. *Results of DR spectroscopy.* (A) The imaginary part of the dielectric function for 0.5 mol/kg solutions of CsCl , Cs_2SO_4 and MgSO_4 and the corresponding transmitted THz pulses (inset). (B) The depolarization (corrected for kinetic depolarization due to conductivity, according to Eq. 6.3) and the fraction of slow water as a function of concentration for the salt solutions CsCl (from Ref. [34]), Cs_2SO_4 , NaCl (from Ref. [26]), LiCl and MgSO_4 . The fraction of slow water is calculated from Eq. 6.4. The lines are linear fits to the depolarization values and serve to distinguish the studied salts. Error bars represent the 95% confidence interval and are derived through error propagation of the experimental uncertainty in the dielectric function.

In Fig. 6.3B, we show the concentration-dependent depolarization (corrected for kinetic depolarization, as described in the previous section) and corresponding slow water fraction for five different salts. It is typically found that ions with a larger charge density (small, multivalent ions) affect the dynamics of a larger number of water molecules, i.e. have a higher hydration number, than ions with a lower charge density (large, monovalent ions) [24–26, 34, 36, 66, 100, 175]. This is caused by the larger local electric field around these ions, which affects the orientation of a larger number of surrounding water molecules. The results for CsCl , NaCl and LiCl are in good agreement with this general rule, since the cation Cs^+ is larger than Na^+ , which is in turn larger than Li^+ . The extracted hydration numbers $N_{\overline{p}}$ for these salt solutions are ~ 0 , ~ 4 and ~ 9 , respectively. This shows that the water molecules in the solvation shell of

Cs^+ show reorientational dynamics similar to bulk liquid water [34], probably because the positive charge of the Cs^+ ion is distributed over a large volume. It also shows that water surrounding the anion Cl^- is not slowed. Therefore, the observed slowly reorienting water molecules are likely located in the first geometrically surrounding solvation shell of the cations Na^+ and Li^+ . Indeed, it is generally considered that the cationic hydration strengths are related as $\text{Li}^+ > \text{Na}^+ > \text{Cs}^+$ [77]).

For Cs_2SO_4 we find that $N_{\vec{p}}^- \approx 1$, where the slowly reorienting water can be attributed to a water molecule located within the solvation shell of strongly hydrated SO_4^{2-} , possibly forming hydrogen bonds with both OH groups to two oxygen atoms of the SO_4^{2-} ion. This result is surprising, since sulfate is a strongly hydrated anion ([77]). Hence the low value of $N_{\vec{p}}^-$ found for Cs_2SO_4 indicates that the effect of anions on water reorientation is either negligible or not measurable by DR measurements. Similarly, a previous GHz DR measurement of the anions Br^- , I^- , NO_3^- , ClO_4^- and SCN^- found that the impact of these anions on water dynamics is remarkably small and similar, despite the different water affinities of these ions [176]. The results for MgSO_4 form an exception and will be discussed in detail in Section 6.5.

The results of the fs-IR measurements for four aqueous salt solutions are shown in Fig. 6.4. Here, we show the anisotropy decay for the dissolved salts $\text{Mg}(\text{ClO}_4)_2$, LiI , LiCl and Cs_2SO_4 . These measurements show very different behavior from the THz DR measurements: for water around the anion SO_4^{2-} a slowing down of the reorientation dynamics is observed, while for the other solutions, which contain the strongly hydrated cations Li^+ and Mg^{2+} , there is surprisingly little effect. This indicates that the effect of cations on water reorientation is either negligible or not measurable by fs-IR measurements.

6.4 SEMI-RIGID HYDRATION

As we have seen, there is an apparent discrepancy between the DR measurements and the fs-IR measurements: Li^+ shows a large slow fraction when measured with DR, but the fs-IR measurements of LiI and LiCl show a negligible slow fraction. For the hydrated anion SO_4^{2-} , the opposite is the case: no slow fraction is observed with DR spectroscopy, whereas fs-IR measurements show the existence of a significant slow water fraction. These apparently contradictory results are shown in Fig. 6.5.

The differences between the results of DR and fs-IR can however be understood by noting the different molecular vectors that the two measurement techniques probe: the permanent dipole moment \vec{p} of water molecules in the case of DR and the OD-stretch transition dipole moment $\vec{\mu}$ in the case of fs-IR (see Fig. 6.6). The local electric field around the ions causes the dipole vector \vec{p}

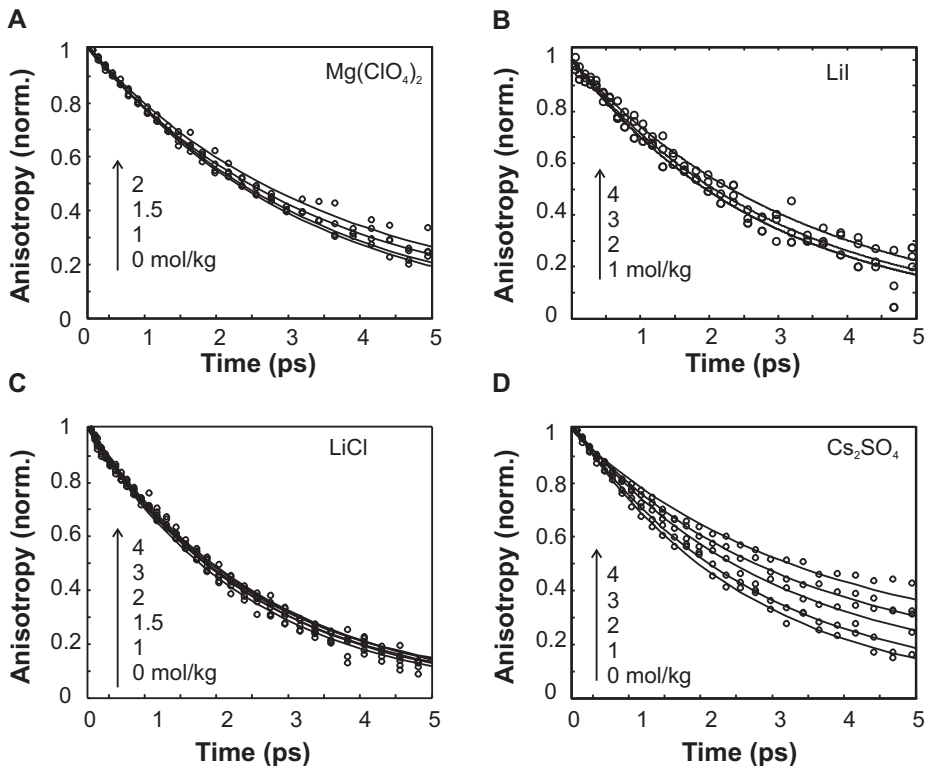


FIGURE 6.4. *Results of fs-IR spectroscopy.* The normalized decay of the anisotropy $R(t)$ for a number of concentrations of $\text{Mg}(\text{ClO}_4)_2$ (A), LiI (B), LiCl (C) and Cs_2SO_4 (D). The lines are bi-exponential fits according to Eq. 6.7.

of water molecules in the solvation shell of a cation to point radially away from the cation, whereas for an anion one of the OD groups of a hydrogen-bonded water molecule linearly points towards the anion [117, 150]. Fig. 6.6 shows that the observed rotational motion of water molecules in the cationic solvation shell does not lead to reorientation of the vector \vec{p} , but does result in randomization of the transition dipole vector $\vec{\mu}$. For the case of anions, the reverse effect occurs: for water molecules in the anionic solvation shell, the motion of \vec{p} is unrestricted within a cone with fixed axis $\vec{\mu}$, where $\vec{\mu}$ corresponds to the vector of the OD that is hydrogen-bonded to the anion.

Reorientation in a cone with a semi-cone angle between $\vec{\mu}$ and \vec{p} of $\theta \approx 52^\circ$ (half the HOD-bond angle) leads to a complete randomization of a vector whose motion is unrestricted within the cone (see Fig. 6.7). This explains the insensitivity of DR towards anionic, and of fs-IR towards cationic hydration. For both cations and anions, these observations lead to a molecular picture

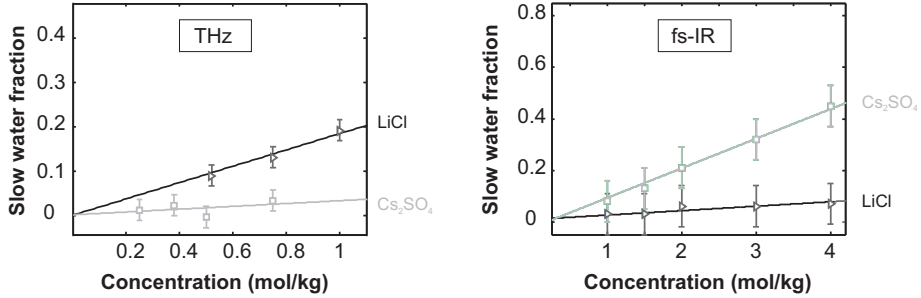


FIGURE 6.5. *Discrepancy between THz DR and fs-IR spectroscopy.* The left figure shows the slow water fractions for LiCl and Cs₂SO₄ as extracted with THz DR spectroscopy; the right figure shows the slow water fractions for the same salts as extracted with fs-IR spectroscopy.

of "semi-rigid hydration", i.e. water molecules in ionic solvation shells that reorient in a propeller-like manner, giving rise to anisotropic reorientation, along a distinct axis.

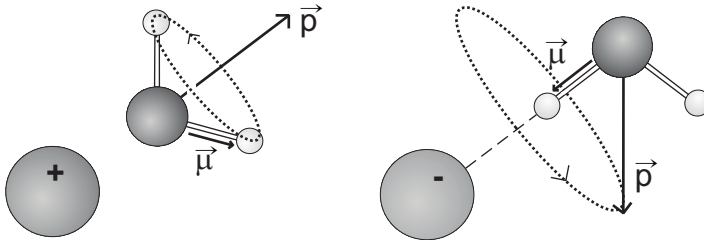


FIGURE 6.6. *Semi-rigid hydration.* A water molecule in the solvation shell of a cation (left) and an anion (right). Dielectric relaxation measurements probe the reorientation of the permanent dipole vector \vec{p} . Femtosecond infrared spectroscopy is sensitive to the reorientation of the OD-stretch transition dipole moment $\vec{\mu}$. The dotted arrows indicate reorientation in a cone, in the case of semi-rigid hydration.

To show that reorientation around a fixed axis leads to complete randomization of the vector whose motion is unrestricted within the cone, we calculate the expected end level of the anisotropy $R_{t \rightarrow \infty}$ for a water molecule that can rotate with a fixed angle around a certain axis. The geometry is given in Fig. 6.7, where it is generalized to the rotation of a vector around an axis with an angle θ between vector and axis. The initial orientation μ_i corresponds to an angle ϕ_i in the circular plane in which the vector will precess. The final orientation is associated with angle ϕ_e . We take $\phi_i = 0$ and integrate over ϕ to allow the final orientation to have a randomly distributed angle $\phi = \{0, 2\pi\}$. We find

$$R_{t \rightarrow \infty} = \frac{2}{5} \int_0^{2\pi} P^{(2)}(\mu_i \cdot \mu_e) d\phi \quad (6.9)$$

with $P^{(2)}(x) = \frac{1}{2}(3x^2 - 1)$, the second order Legendre polynomial, $\mu_i = (\sin(\theta), 0, \cos(\theta))$ and $\mu_e = (\sin(\theta) \cos(\phi), \sin(\theta) \sin(\phi), \cos(\theta))$. The result for the anisotropy end level is shown in Fig. 6.7 as a function of the angle θ . The angle between the rotating vector and the rotational axis in the case of a water molecule that rotates around its permanent dipole is half the HOD bond angle and hence $\sim 52^\circ$. It is clear that the anisotropy end level is very small (< 0.005), indeed confirming that such reorientation leads to complete randomization of the vector.

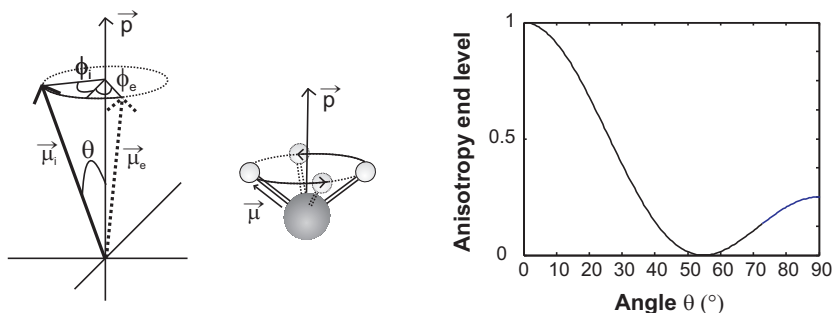


FIGURE 6.7. *Rotation in a cone.* Graphical representation of the geometry, where a water molecule can rotate around the axis of its permanent dipole \vec{p} . The initial and final state of the OD-stretch dipole moment are given by $\vec{\mu}_i$ and $\vec{\mu}_e$, respectively. The graph on the right shows the anisotropy end level as a function of the angle θ between $\vec{\mu}$ and the axis of rotation.

6.5 COOPERATIVITY

The molecular picture of semi-rigid hydration explains the ion effect on water molecules directly surrounding the ion. This picture holds for salts for which one of the counterions is weakly hydrated. However, when both ions are strongly hydrated, we find that the effect on water dynamics can be much stronger and non-additive. In Fig. 6.8, we show the normalized anisotropy for $\text{Mg}(\text{ClO}_4)_2$, Cs_2SO_4 and MgSO_4 , each for concentrations ranging from 0 to 2 mol/kg. A remarkable conclusion can be drawn from these three measurements: MgSO_4 shows a very large slow reorientation component, whereas Mg^{2+} and SO_4^{2-} individually, in combination with other ions (ClO_4^- and Cs^+ , resp.) do not. In Fig. 6.9B, we show the slow water fraction as a function of salt concentration. Clearly, MgSO_4 has a much larger fraction of slowly reorienting

water molecules (corresponding to a hydration number $N_{\bar{\mu}} = 32$, extracted using Eq. 6.8) than $\text{Mg}(\text{ClO}_4)_2$ and Cs_2SO_4 (with hydration numbers $N_{\bar{\mu}}$ of 4 and 9, respectively). This means that the dynamics of a large number of water molecules are affected, due to a cooperative effect of the cation and the anion. The size of most ions allows them to be structurally surrounded by ~ 6 water molecules. Hence, a value of $N_{\bar{p}} > 6$ and $N_{\bar{\mu}} > 12$ implies that the effect of the ion on the orientational dynamics of water extends well beyond the first structurally surrounding shell of water molecules.

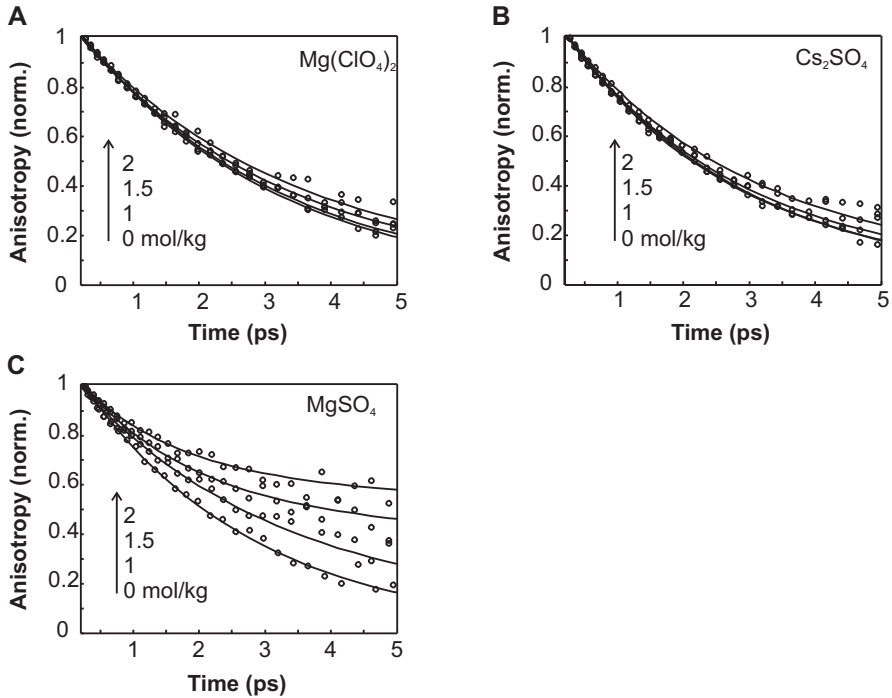


FIGURE 6.8. The normalized decay of the anisotropy $R(t)$ for a number of concentrations of $\text{Mg}(\text{ClO}_4)_2$ (A), Cs_2SO_4 (B) and MgSO_4 (C).

The THz DR data in Fig. 6.9A show the same cooperative effect as the fs-IR measurements: $\text{Mg}(\text{ClO}_4)_2$ has a hydration number $N_{\bar{p}} = 6$ and Cs_2SO_4 has a hydration number $N_{\bar{p}} = 1$, respectively associated with water molecules directly adjacent to the Mg^{2+} ion and a water molecule hydrating the SO_4^{2-} ion. For MgSO_4 $N_{\bar{p}} = 18$, which is much larger than the sum of the hydration numbers of $\text{Mg}(\text{ClO}_4)_2$ and Cs_2SO_4 . For MgSO_4 , there are approximately twice as many slowly rotating OH groups ($N_{\bar{\mu}}$) as slowly rotating dipoles ($N_{\bar{p}}$), indicating that the same collection of slow water molecules is observed by fs-IR and THz DR. Even the combination of the moderately strongly hydrated cation Na^+ with the strong anion SO_4^{2-} is observed to affect the dynamics

of a large number of water molecules ($N_{\vec{\mu}} = 24$; see Fig. 6.9B). The same is true for the combination of the moderately strongly hydrated anion Cl^- with the strong cation Mg^{2+} (see Fig. 6.9A). In these cases, however, the hydration numbers are also increased because there are three instead of two ions per dissolved salt molecule. These results lead to the conclusion that the effects of ions and counterions can be strongly interdependent and non-additive. The key parameter determining how strongly ions affect water dynamics is thus the combination of the solvated cation and anion.

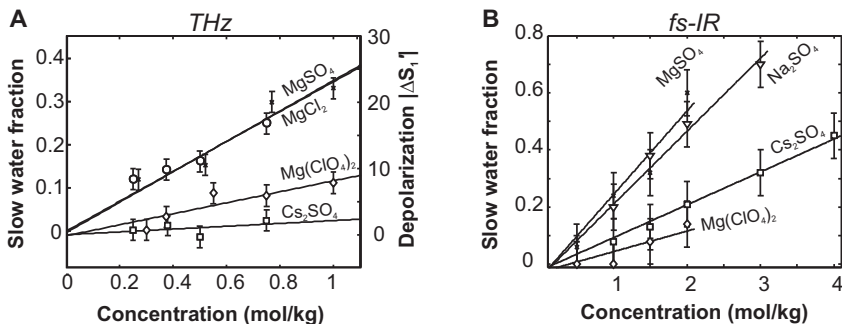


FIGURE 6.9. *Cooperativity*. The fraction of slow water compared to bulk-like water as a function of salt concentration as measured by THz spectroscopy (A) and by fs-IR spectroscopy (B). The lines are linear fits and serve as guides to the eye to distinguish the studied salts. The error bars are based on at least three measurement runs and represent the 95% confidence interval.

It is clear that the effect of MgSO_4 , Na_2SO_4 and MgCl_2 on water extends well beyond the first solvation shell of the ions and that the ions show strong cooperativity in affecting the dynamics of water molecules. Previous GHz DR studies by Buchner et al. showed the presence of a certain amount of (contact and solvent-separated) ion pairs for solutions of MgSO_4 and Na_2SO_4 [24, 25]. Our THz DR measurements are not directly sensitive to the reorientation of ion pairs, since ion pairs lead to additional dielectric loss peaks at very low frequencies (<5 GHz), located well outside our THz measurement window (0.4 – 1.2 THz). For the fs-IR measurements we can neglect the contribution of contact ion pairs to the anisotropy data, since this technique excites and probes specifically the OD vibrations of water molecules. Hence, the dramatic slowing down of the anisotropy decay for MgSO_4 and Na_2SO_4 corresponds to slow reorientation of water molecules, not the slow reorientation of contact ion pairs. A remaining question is whether the observed slow water molecules could be water hydrating ion pairs. In the case of contact ion pairs, this is very unlikely because the concentration of contact ion pairs is generally small – less than

10% for MgSO_4 , even at high salt concentrations [25] – whereas the observed cooperative effect leads to a slowing down of a large fraction of the water (up to 70% of all water molecules in the solution; see Fig. 6.9). In the case of solvent separated ion pairs, it is likely that the water molecules that separate the ions have slow reorientation dynamics. The large hydration number for MgSO_4 indicates that there are large extended structures of slowly reorienting water molecules in between Mg^{2+} and SO_4^{2-} ions (see Fig. 6.10).

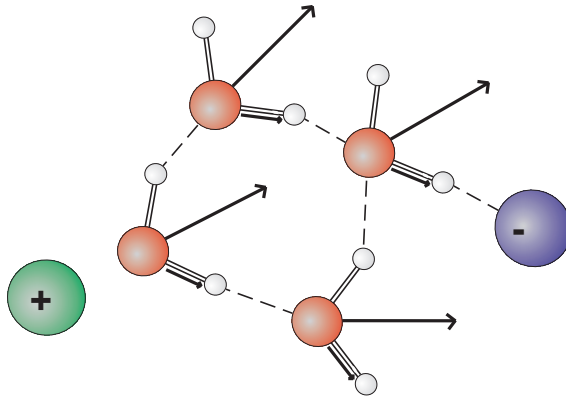


FIGURE 6.10. Proposed geometry, in which the water dynamics are locked in two directions due to the cooperative interaction with the cation and the anion.

The cooperativity in ion hydration can be explained from the fact that the cation and anion lock different degrees of freedom of the water molecules, i.e. the direction of the bisectrix (\vec{p}) and the direction of OD ($\vec{\mu}$), respectively. The nearby presence of both ions can thus lead to a locking in both directions of the hydrogen-bond structure of several intervening water layers, giving rise to the observation in DR and fs-IR of slowed down water molecules well beyond the first solvation shell. This cooperativity is schematically illustrated in Fig. 6.10. As illustrated in this figure, we expect the solvation structures to be quite directional in between the ions. If an ion forms ~ 4 of these structures with surrounding counterions, the value of $N_{\vec{p}}$ of 18 implies that each of these structures consist, on average, of 4-5 water molecules. This interpretation also means that for solutions like MgSO_4 and Na_2SO_4 the slowly reorienting water molecules are not arranged in a spherically symmetric way around the ions.

6.6 TEMPERATURE DEPENDENCE

The reorientation of water molecules in the rigid, locked hydrogen-bond structure occurring for MgSO_4 can be expected to show a different temperature

dependence compared to neat liquid water. We measure the temperature dependence of the anisotropy decay for 1.5 mol/kg MgSO_4 (Fig. 6.11A) over an interval of about 50 °C. We compare the temperature dependence to that of a 4 mol/kg Cs_2SO_4 solution (Fig. 6.11B) with the same hydration level (Fig. 6.8D), but no cooperativity. At room temperature, the anisotropy for MgSO_4 decays more slowly than for Cs_2SO_4 , but with increasing temperature the situation reverses. To quantify the results, we fit the anisotropy data at different temperatures with a single averaged time scale for all water molecules in the system. This means that a change in this time scale represents both the changes in time scales and changes in the relative fractions of bulk-like and slow water molecules. Figure 6.11C shows a much stronger temperature dependence of this average time scale for a solution of 1.5 mol/kg MgSO_4 than for a solution of 4 mol/kg Cs_2SO_4 .

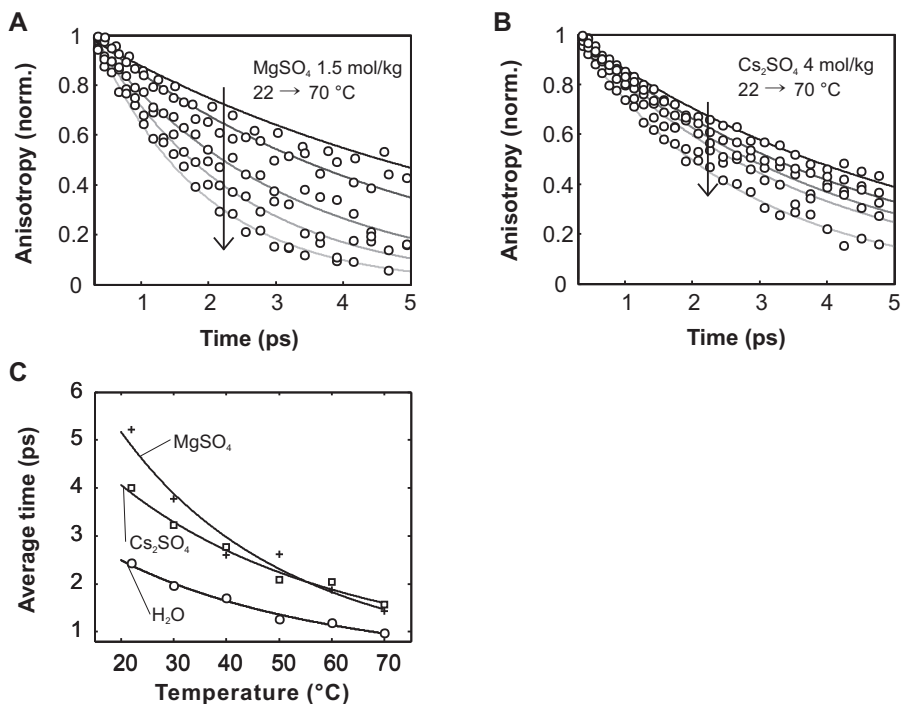


FIGURE 6.11. Temperature dependence of the reorientation. The temperature-dependent anisotropy decay data for MgSO_4 (A) and Cs_2SO_4 (B) with fits as explained in the text. (C) Average reorientation times of solutions of 1.5 mol/kg MgSO_4 , 4 mol/kg Cs_2SO_4 and neat H_2O : H_2O (from Ref. [164]) as a function of temperature.

The difference in temperature dependence of the reorientation of MgSO_4 and Cs_2SO_4 solutions indicates that the reorientation within the hydration structures involves a different mechanism. For pure water it was found from

MD simulations that the reorientation of water follows a concerted mechanism and that the rate-limiting step for reorientation of a water molecule is the motion of a second water molecule in and out of the solvation shell of the first [81, 83]. For the Cs_2SO_4 solution the hydration number $N_{\vec{\mu}}$ has a value of 9, which is likely associated with the OH groups of water molecules that are hydrogen bonded to the SO_4^{2-} ion. In view of the small value of $N_{\vec{\mu}}$, these water molecules are surrounded by water molecules that show bulk-like dynamics. Hence, although the reorientation of the water molecules hydrating the SO_4^{2-} is slow, the temperature dependence of this reorientation is similar to that of pure liquid water, because the reorientation is governed by hydrogen-bond interactions to water molecules that show bulk-like behavior. Correspondingly, the temperature dependence of the reorientation time of Cs_2SO_4 has the same slope as for bulk water. In contrast, for MgSO_4 the solvation structures are large, as expressed by the large values of the hydration numbers $N_{\vec{p}} = 18$ and $N_{\vec{\mu}} = 32$. Hence, the reorientation of a water molecule in the solvation structure relies on the motions of water molecules that are contained in the same solvation structure. These motions are substantially slowed down, and reorientation thus involves a collective reorganization of the extended solvation structure, which explains the difference in temperature dependence with a solution of Cs_2SO_4 and pure liquid water.

6.7 CONCLUSION AND OUTLOOK

In conclusion, we have found that the hydration structure of a strongly hydrated ion depends critically on the nature of its counterion. If the counterion is weakly hydrated, the strongly hydrated ion is surrounded by a semi-rigid solvation shell, where reorientation is restricted only in a certain direction, but is still allowed in other directions. If, however, strongly hydrated cations and anions are combined, the dynamics of water molecules well beyond the first solvation layer are affected through a cooperative effect of the ions. In this case, the hydrogen-bond network in between the ions is locked in multiple directions. These findings show that the effect of ions on water dynamics can be strongly interdependent and non-additive.

The observed cooperativity in ion hydration has implications for the Hofmeister series, where an ordering is given for the relative strength of cations and ions to affect properties (such as solubility) of a biomolecular solution (see Chapter 1). Due to the cooperative effects, the Hofmeister series should be considered in terms of salts, instead of individual ions^a. Furthermore, it is likely that the molecular origin of the Hofmeister series is related to cooperative effects between ions, e.g. Ca^{2+} , and biomolecules, e.g. DNA and

^aIn his original work (published at the end of the 19th century), Franz Hofmeister described the effect of salts on biological solutions. The interpretation in terms of the effect of individual ions was given later [57, 77, 78].

proteins, which contain negative charges. Due to this cooperativity between ions and biomolecules, the water dynamics can be affected, which in turn leads to changes in the properties of the solution. This explanation of the molecular origin of the Hofmeister series forms an alternative to the direct ion-biomolecule effects or the pure ion-water effects.

7 STRUCTURE AND DYNAMICS OF THE HYDRATED PROTON

We study the hydration of protons in liquid water using terahertz time domain spectroscopy and polarization-resolved femtosecond mid-infrared pump-probe spectroscopy. We observe that the addition of protons leads to a strong decrease of the dielectric response of liquid water that corresponds to 19 ± 2 water molecules per dissolved proton. This depolarization results from water molecules (~ 4) that are strongly bound to the proton, and from the reorientational motion of water (corresponding to the response of ~ 15 water molecules) involved in the transfer of the proton charge.

7.1 INTRODUCTION

Protons in hydrogen-bonded networks play an important role in many fundamental and technological processes in chemistry, physics and biology. Examples include acid-base reactions, proton exchange membrane fuel cells (see Fig. 1.3) and transmembrane proton pumps. One of the remarkable properties of protons in aqueous solutions is their anomalously high mobility [16]. This has been attributed to the Grotthuss mechanism, which differs from the typical Stokes mass diffusion for ion transport. The Grotthuss mechanism is based on the efficient interconversion between the Eigen complex, H_9O_4^+ , and the Zundel complex, $[\text{H}_2\text{O} \cdots \text{H} \cdots \text{H}_2\text{O}]^+$, which constitutes the proton charge transport [1, 32, 103, 104, 168, 184]. Here, the proton shuttles to an adjacent water molecule by interconversion of a hydrogen bond and a covalent bond (see Fig. 7.1). Hence the charge, rather than the mass, of the proton is transferred, making proton conductivity significantly larger than that of other ions [16].

Both theory and experiment have found indications that protons can affect the solvating hydrogen-bond network over a relatively long distance. Simulations using Multistate Empirical Valence-Bond analysis, have indicated that proton transfer couples to hydrogen-bond dynamics of large water clusters of at least three hydration shells [86]. The hydration of the proton has also been studied with different experimental techniques including infrared and far-infrared spectroscopy [53, 91, 106, 107, 144, 146, 149, 189]. These studies have arrived at very different values for the number of water molecules affected

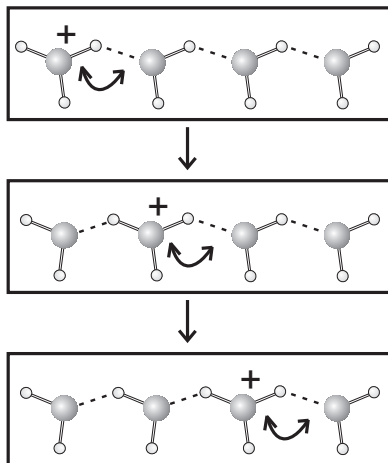


FIGURE 7.1. The Grotthuss mechanism for proton transport.

by the proton, ranging from ~ 6 to ~ 100 . This wide range of values may be traced to several drawbacks of previous techniques that have been applied to measuring the effect of the proton on water. In the infrared, the aqueous proton gives rise to broad structureless bands, from which it is very difficult to deduce information about the water structure. Microwave spectroscopy is in principle very well suited to study the effects of ions on the structural dynamics of water, as has been demonstrated for different salts [25, 26, 34, 53, 175, 176]. However, for the study of the effect of the proton on water this technique is not well suited, because the mobility of the proton leads to very strong absorption and loss of signal at microwave frequencies. This problem is much less severe at higher frequencies, because the absorption due to charge mobility is inversely proportional to the probing frequency. Recently, the technique of terahertz time-domain spectroscopy (THz-TDS) [68, 138, 140] has been developed, and it has been shown that this technique is ideally suited to study water structure and dynamics [41, 56, 71]. Here we use this technique in combination with polarization-resolved femtosecond mid-infrared pump-probe spectroscopy to study the effects of the proton on the structural dynamics of water.

7.2 EXPERIMENTAL

The THz-TDS setup (see Chapter 3, Fig. 3.4) is based on THz generation and detection in ZnTe non-linear crystals, using 800 nm pulses with a duration of ~ 110 fs. The time-dependent electric field strength of the THz pulses (~ 3 ps) that are transmitted through the sample are measured by means of electro-optic sampling with a variably delayed pulse of 800 nm light with a duration of ~ 150 fs in a second ZnTe crystal. THz-TDS provides the frequency-dependent com-

plex dielectric response of a sample $\hat{\epsilon}(\omega)$. We determine the complex dielectric response of water around protons. To isolate specifically the effect of the proton, we measure the difference between the dielectric response of an acid (e.g. HCl) and its corresponding salt (e.g. NaCl) for different acid-salt combinations. This way, we can correct the data for the contribution of the anions on the water solvent. We employ a mechanical device that alternatively positions two samples (a salt and an acid solution in cuvettes that have chambers with an optical path length of $103 \pm 0.5 \mu\text{m}$) in the THz beam. This approach minimizes the effect of fluctuations in THz intensity and temperature as noise sources and allows calibration of the measured dielectric response (see Section 4.1.2 for details on the extraction and calibration).

The polarization-resolved femtosecond mid-infrared pump-probe setup (see Chapter 3, Fig. 3.5) uses a pump pulse to label specifically oriented water molecules with a vibrational excitation. The subsequent vibrational and orientational relaxation is monitored using a weak probe pulse. Using this technique, we can readily determine the decay of the anisotropy $R(t) = \frac{\Delta\alpha_{\parallel} - \Delta\alpha_{\perp}}{\Delta\alpha_{\parallel} + 2\Delta\alpha_{\perp}}$, where $\Delta\alpha_{\parallel}$ and $\Delta\alpha_{\perp}$ are the pump-induced change in absorption with the polarization of the pump pulse parallel and perpendicular to the probe pulse, respectively (see Section 4.2.2). The exponential decay of the anisotropy gives the (second order) reorientation time of the excited water molecules. As will be shown below, this parameter is important for the analysis of the dielectric response of protons in water.

We employ THz-TDS in the region between 0.3-1.2 THz to examine the hydration of protons in liquid water. Up to a frequency of 1.2 THz, the dielectric response is dominated by dielectric relaxation [46]. The dielectric relaxation response of water $\hat{\epsilon}(\omega)$ contains information on how well the permanent dipoles associated with water molecules can keep up with oscillating fields of frequency ω . For pure water at room temperature, $\hat{\epsilon}(\omega)$ can be described with the double Debye relaxation model [46, 68, 138–140, 186]

$$\hat{\epsilon}(\omega) = \frac{S_1}{1 + i\omega\tau_D} + \frac{S_2}{1 + i\omega\tau_2} + \epsilon_{\infty} . \quad (7.1)$$

Here, the first (main) term represents the dielectric relaxation process with strength S_1 and a time constant of $\tau_D \approx 8$ ps (the Debye time) at room temperature. The Debye time describes the cooperative reorganization of water solvent molecules. The second term is thought to be associated with undercoordinated water molecules [186] and has a (much smaller) strength S_2 and a (shorter) timescale τ_2 . Finally, ϵ_{∞} represents the dielectric constant in the high frequency limit.

When ions are added to water, the dielectric response changes. First of all, the dielectric response includes a contribution from the conductivity of the charged ions (see Eq. 2.13). Secondly, ions may affect both the Debye

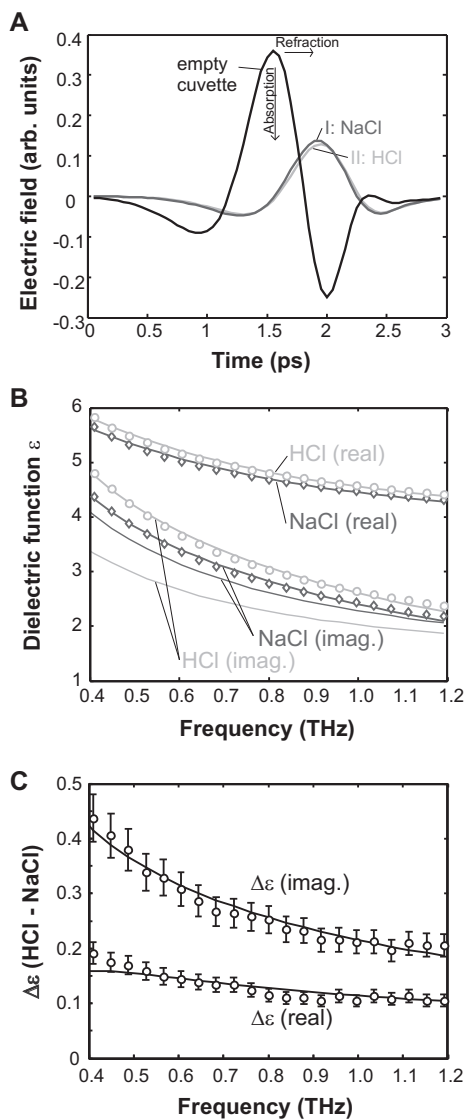


FIGURE 7.2. (A) THz pulses as transmitted through an empty cuvette and through cuvettes filled with a 1 mol/kg solution of NaCl and HCl, respectively. (B) The extracted dielectric function of 1 mol/kg HCl and 1 mol/kg NaCl. The thick lines that go through the data points are a fit to Eq. 7.1 with S_1 for the salt (NaCl) fixed to its literature value from Ref. [26]. The thin lines represent the dielectric response after correction for the conductivity contribution. (C) The differential dielectric response $\Delta\epsilon$ for 1 mol/kg HCl-NaCl, with the fit according to Eq. 7.2. Error bars indicate the 95 % confidence interval.

time τ_D and the strength of the relaxation process S_1 of the water molecules surrounding the ions. The latter occurs when the electric field of ions affects the reorientation dynamics of the surrounding water molecules, which as a result can no longer participate in the relaxation process. Strong hydration therefore leads to a lowering of the relaxation strength S_1 , i.e. to a depolarization effect (see also Section 6.2.1). We determine how the presence of protons affects the dielectric relaxation parameters by measuring the differential dielectric response for the following acid-salt combinations: HCl-NaCl, HCl-KCl, HCl-CsCl, HCl-LiCl, HClO₄-NaClO₄ and HI-NaI. These salts were chosen, since the cooperative effects are limited, meaning that the effect of the cations and anions can be considered independently (see Chapter 6). The concentrations were varied between 0.25 and 1.0 mol/kg.

7.3 RESULTS AND DISCUSSION

In Fig. 7.2(a), we show the transmitted THz pulses through an empty cuvette and through cuvettes filled with a 1 mol/kg solution of HCl and a 1 mol/kg solution of NaCl in pure water. The acid solution has a somewhat higher absorption and refraction than the salt solution. This is caused by the proton conductivity, which is 5 times larger than that of the sodium ions [16]. We analyze the data in the frequency domain using Fresnel equations [72] (see Section 4.1.2 for details). Using the independently determined cuvette responses, we extract the dielectric response of the two samples separately.

The dielectric responses of the 1 mol/kg HCl-NaCl acid-salt combination and the differential response are shown in Fig. 7.2(b-c), respectively. To quantify the effect of the presence of the proton on the water structure and dynamics, we examine the differential dielectric response $\Delta\hat{\epsilon}$ (HY-XY) for each acid-salt (HY-XY) combination. We use the following equation to model the differential dielectric response

$$\Delta\hat{\epsilon}(\omega) = \frac{\Delta S_{1,H} - \Delta S_{1,X}}{1 + i\omega\tau_D} + \frac{\sigma_{HY} - \sigma_{XY}}{i\omega\epsilon_0} + \Delta(S_2, \epsilon_\infty) \quad (7.2)$$

In this equation $\Delta S_{1,H}$ and $\Delta S_{1,X}$ represent the proton and the cation effect on the pure water parameter S_1 , respectively. The second term, where the vacuum permittivity is given by ϵ_0 , is concerned with the difference in conductivity of the acid σ_{HY} and salt σ_{XY} solutions. Following [26, 34, 175, 176] we assume that the conductivity σ is independent of frequency^a. The last term $\Delta(S_2, \epsilon_\infty)$ takes

^aCharges, such as electrons in a free electron gas, often have a frequency-dependent conductivity that follows the Drude equation: $\sigma \propto \frac{1}{1+i\omega\tau}$, where τ is the average time between collisions between electrons and the crystal lattice. In the case of short collision time τ , the conductivity becomes purely real (corresponding to a purely imaginary dielectric function) and frequency-independent. Given the expected short time τ for protons in water, a frequency-independent conductivity seems a valid approximation.

into account the different effects that the proton and the cation have on the relaxation process with strength S_2 and on ϵ_∞ . These effects are significantly smaller than the effects on S_1 . This is apparent from the spectral shape of the differential response, and intuitive given the small (few percent) contribution of the S_2 process on the overall dielectric response.

To arrive at Eq. 7.2, we have made the assumption that the Debye reorientation time τ_D is the same for acid and salt solutions with the same anion. This assumption is corroborated by (i) microwave measurements of dielectric relaxation that have indeed indicated that τ_D is mainly affected by the presence of anions and not cations [26, 34, 176] and by (ii) polarization-resolved femtosecond pump-probe measurements in the mid-infrared. This measurement technique has proven to be capable of probing the effect of cations and anions on the water reorientation (see Chapter 6). The results in Fig. 7.3 show that the second order reorientation time $\tau_r^{(2)}$, which is approximately equal to $\frac{1}{3.4}\tau_D$ (see Ref. [164]), is indistinguishable for 0:4, 1:3 and 2:2 aqueous solutions of $\text{HClO}_4:\text{NaClO}_4$ with a constant anion concentration of 4 mol/kg. Since the concentration of anions is kept constant, we isolate the effect of the proton. We do not probe water molecules that are in close proximity of the anion or part of the proton complex, since these have a different spectral response [119, 184].

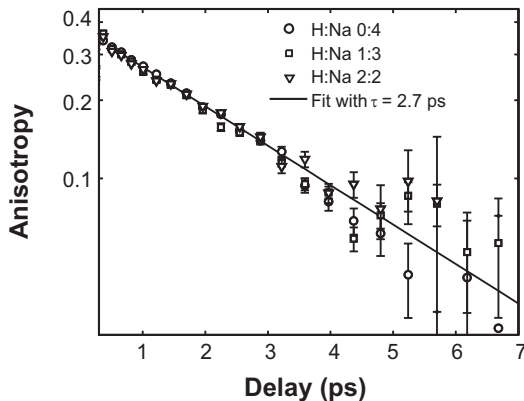


FIGURE 7.3. The decay of the anisotropy R is independent of the proton:cation ratio, corroborating the assumption that τ_D remains the same for protons and cations.

We extract the depolarization effect of the proton $\Delta S_{1,H}$ for each acid-salt combination using Eq. 7.2. The fit results for the 1 mol/kg solutions of HCl and NaCl are shown in Fig. 7.2(c). We have first fit the dielectric response of the salt solution to obtain τ_D and use this number to fit the differential dielectric responses to Eq. 7.2. We use data from the literature for the conductivity of the solutions (σ_{HY} and σ_{XY}) and for the depolarization effect of the cation $\Delta S_{1,X}$. The data for the salt solutions are taken from GHz dielectric relaxation

measurements by Buchner et al. [26, 34, 175, 176]. We show the results for the depolarization effect of protons, $\Delta S_{1,H}$, in Fig. 7.4. The data are independent of the identity of the different cations and anions, which validates our approach to isolate specifically the effect of the proton on the water response.

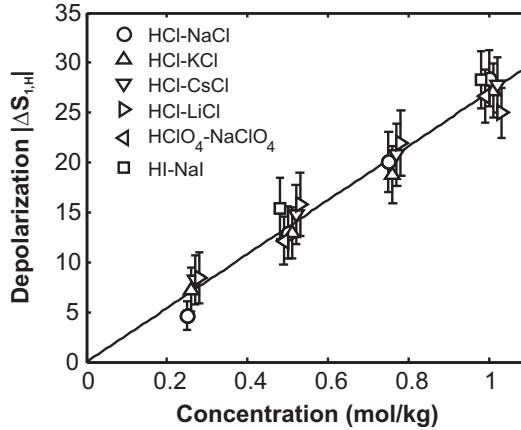


FIGURE 7.4. The depolarization induced by protons for different proton concentrations. Each data point corresponds to a differential measurement for an acid-salt combination and is slightly horizontally offset for clarity. The line is a linear fit to all data points. The slope is a direct measure for the number of water molecules that is affected by the presence of the proton. Above concentrations of 1.5 mol/kg the relation becomes non-linear, indicating overlapping hydration layers [41, 56].

For all measurements with different acid-salt combinations the value of $\Delta S_{1,H}$ is negative. This finding is in line with the results of microwave dielectric relaxation measurements [26, 34, 175]. In these measurements it was found that cations have a depolarization effect. This is partially due to the excluded volume of the ions and partially due to interaction between the electric field of an ion and the surrounding water molecules (see also Chapter 6). Smaller and multivalent cations typically have a stronger hydration and hence larger depolarization effect. Our results show that protons induce an anomalously large depolarization effect. We extract the number of affected water molecules N_H around protons through [54]^b

$$N_H(c) = \left(c_s - \frac{S_1 + \Delta S_{1,H}}{S_1} c_0 \right) / c \quad (7.3)$$

^bAn alternative method of calculating the number of affected water molecules, namely using the solvent-normalized Cavell equation, which takes into account local field effects [25], yields $N_H = 20$ instead of 19.

In this equation c is the concentration of protons, c_s is the concentration of solvent water molecules in the solution and c_0 represents the concentration of water molecules of pure water (55.5 mol/L). Furthermore S_1 corresponds to the relaxation strength of pure water and $\Delta S_{1,H}$ to the depolarization effect of protons. Using our results for the depolarization effect of protons, we find that for protons in water $N_H = 19 \pm 2$, where the uncertainty consists of a part due to experimental uncertainty ($\sim 2\%$) and a part due to systematic uncertainty in the assumed literature values for the cation depolarization and the salt and acid conductivities ($\sim 8\%$). Surprisingly, this number of affected water molecules is even larger than the strongly hydrating cation Mg^{2+} , which has been found to have an effect on ~ 6 water molecules (see Chapter 6).

7.4 DISCUSSION AND CONCLUSION

The depolarization effect of the proton likely has a very different origin from that of for instance Mg^{2+} . For cations like Mg^{2+} , the depolarization results mainly from the effect of the electric field of ions on nearby water molecules (see Fig. 6.1). This effect will also occur for protons, but for the proton an additional effect is important: the depolarization is also the result of the motion of water molecules associated with the motion of the proton charge. A charge (the proton) that moves in the driving electric field (the THz pulse) causes the surrounding water molecules to rotate [60]. The direction of this rotation has an opposite sign compared to the direction of the externally applied electric field (see Fig. 6.1), hence resulting in a *decrease* in the dielectric relaxation strength. We calculate the effect of this kinetic depolarization using Eq. 6.3 and find that the kinetic depolarization corresponds to the response of ~ 15 water molecules. The remaining depolarization effect of ~ 4 water molecules is likely due to water molecules that are strongly bound by the proton. This number of ~ 4 bound water molecules corresponds well to the so-called Eigen $[H_9O_4]^+$ hydronium complex that has been found in MD simulations [1,104,168].

Our findings experimentally confirm the results of recent simulations, which showed that a small number of very strong hydrogen bonds are present directly around the proton [102] and that the rate-limiting step for proton transport is the collective reorganization of a larger number of water molecules [86]. This leads to a more detailed picture of proton transport in water, as we show in Fig. 7.5. Here, water molecules that are hydrogen bonded to the original hydronium complex undergo a structural transition from a planar geometry to a tetrahedral geometry. Vice versa, water molecules that become hydrogen bonded to the new hydronium complex undergo a transition from a tetrahedral to a planar geometry.

The observation that a large number of water molecules are involved in aqueous proton transport has important consequences for proton hydration

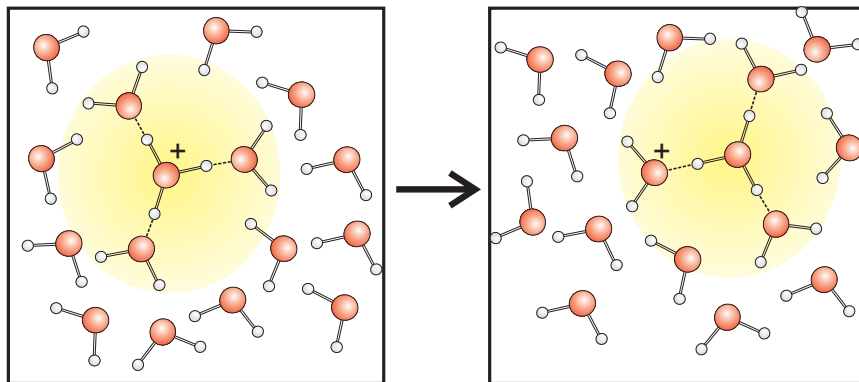


FIGURE 7.5. Schematic picture of proton transport. Here, the initial state is an Eigen complex with 3 water molecules surrounding a hydronium ion. After reorganization of a number of water molecules, the final state is again an Eigen complex, where one of the 3 water molecules that originally surrounded the hydronium ion now carries the proton charge, i.e. became the hydronium ion, which is in turn surrounded by three strongly hydrogen-bonded water molecules. This process can be regarded as the transport of an "inverted polaron", in analogy to electrons in a crystal lattice. The electric field of an electron can cause a deformation of the ordered crystal lattice, forming a polaron. In our case, the electric field of the proton causes a local ordering in an otherwise disordered water matrix: an inverted polaron.

and transport in systems in which the number of water molecules is limited, as is for instance the case in confined systems. Examples of these systems are protons confined in micelles and protons in membranes and transmembrane proton pumps and protons in proton exchange membrane fuel cells (see Chapter 1). Based on the present observations, we expect that the bulk mechanism of proton transfer is not efficient in these confined systems or that in strongly confined systems a different, modified mechanism of proton transport occurs.

8 PROTON TRANSFER IN WATER NANOPOOLS

Proton transfer from the photoacid 8-hydroxy-1,3,6-pyrenetrisulfonic acid (HPTS) to water is studied in reverse micelles with ionic (AOT = sodium dioctyl sulfosuccinate) and non-ionic (BRIJ-30 = polyoxyethylene(4)lauryl ether) surfactants. The dynamics are studied by probing the transient electronic absorption and transient vibrational absorption, both with sub-picosecond resolution. The reverse micelle sizes range from approximately 1.6 to 5.5 nm in diameter. We find that the rate of proton transfer decreases with decreasing reverse micelle size, for both studied surfactants. In addition, for AOT reverse micelles, a fraction of the photoacid molecules exhibit non-radiative decay, thereby quenching the proton transfer.

8.1 INTRODUCTION

Protons in water play an essential role in many chemical and biological processes. In living organisms, water is commonly contained in very small volumes. As a result, protons are often dissolved in nanopools of water within a membrane [114]. The confinement of water and the interactions with the confining surfaces can have strong effects on the proton mobility. Similar effects can also arise in proton exchange membrane fuel cells, where a proton flows within a confined aqueous environment [190]. Reverse micelles are an exquisite model for studying confined water [90,98]. Early studies of proton transfer in reverse micelles were done by Politi et al. [130,131] and Bardez et al. [11,12] using fluorescence measurements. It was observed that small reverse micelles have a decreased proton transfer rate, whereas in larger reverse micelles protons exhibit the same dynamics as in bulk water. More recently, the dynamics of protons in confined aqueous environments were studied in the optical regime using time-correlated single photon experiments with an instrument response function of 45 ps [111,156]. These studies focused on confined water in Nafion fuel cell membranes. Additionally, reverse micelles were studied using AOT (sodium dioctyl sulfosuccinate) as the surfactant. The hydrophilic groups of AOT and Nafion are quite similar as they both contain sulfonate groups. For both systems the proton transfer was observed to slow down with decreasing water concentration [111,156].

Photoacids are ideal molecules for studying the transfer of protons to water because for these molecules the acidity can be switched by optical excitation, which makes it possible to start the proton transfer reaction at a well-defined point in time. A commonly used photoacid for this type of studies is 8-hydroxypyrene-1,3,6-trisulfonate (HPTS). The proton release from HPTS can be triggered by exciting HPTS with a 400 nm pulse. This excitation leads to an increase in acidity by a factor 10^6 [180]. The subsequent excited state proton transfer reaction ($\text{ROH}^* + \text{H}_2\text{O} \rightarrow \text{RO}^{-*} + \text{H}_3\text{O}^+$) can then be monitored with different optical techniques, including fluorescence emission and transient visible or mid-infrared absorption spectroscopy.

Here we investigate the dynamics of proton transfer from HPTS to water in confined aqueous environments using both electronic absorption in the visible range and vibrational absorption in the mid-infrared range, both with sub-picosecond time resolution. The water nanopools are formed by reverse micelles produced using two different types surfactants, ionic (AOT) and non-ionic one (BRIJ-30 = polyoxyethylene(4)lauryl ether). As a result, we can distinguish the effects of the confinement of the water from the effects of the specific interactions of the system with the surfactant.

8.2 EXPERIMENTAL

We performed pump-probe experiments in which we excite HPTS to an electronically excited state. In the visible region, the absorption and emission of electronically excited states of the acid (ROH^*) and the base (RO^{-*}) can be used to probe the proton transfer reaction [2, 3, 35, 62, 89, 126–129, 132, 151, 155, 167]. In the midinfrared region, the specific vibrational resonances of the photoacid and the photobase can also be monitored [137]. Additionally, probing the broad midinfrared absorption band of the hydrated proton makes it possible to monitor the uptake of the proton by the water solvent [38, 148].

The 400 nm pump, the visible continuum probe, and the tunable infrared pulses are generated using non-linear frequency conversion of light from a commercial Ti:Sapphire regenerative amplified laser system (Spectra-Physics Hurricane). This system produces 110 fs, 1 mJ pulses centered at 800 nm with a repetition rate of 1 kHz. The pump pulse centered at 400 nm is obtained by second harmonic generation of the 800 nm pulses in a $\beta\text{-Ba}_2\text{BO}_4$ (BBO) crystal (2 mm, $\theta = 29^\circ$). The energy of the pump pulse is about 1 μJ . The polarization of the pump beam is set at the magic angle (54.7°) with respect to the probe polarization so that only isotropic signals are probed.

To generate the visible continuum probe pulses, we focus about 1 μJ of the 800 nm pulse into a 3 mm thick z-cut sapphire substrate to generate a broadband continuum with wavelengths ranging from over 1000 nm to just

below 400 nm (see Chapter 3, Fig. 3.7). In probing the transient spectra of the photoacid and photobase, we use the wavelength range between 400 and 700 nm. The probe pulses are spectrally dispersed with a grating-based spectrograph (Acton) and are detected with a home-built diode-array detector.

To generate the tunable mid-infrared probe pulses for the transient vibrational absorption experiments, a white-light seeded optical parametric amplifier (Spectraphysics OPA) converts the 800 nm fundamental into two tunable output pulses: signal (1200 - 1600 nm) and idler (1600 - 2400 nm). These pulses are separated and focused into a AgGaS₂ crystal (2 mm, $\theta = 45^\circ$). Difference-frequency mixing of the signal and idler pulses produces probe pulses that are tunable between 2.7 and 8 μm (3700 - 1250 cm^{-1}). For details of the setup, see Chapter 3, Fig. 3.6.

A computer controlled translation stage sets the relative delay between the pump and probe pulses and an optical chopper blocks every other pump pulse for active background subtraction. The probe pulse is split into two parts, one of which is focused into the sample in spatial overlap with the pump pulse. The other part is not focused in overlap with the pump pulse and is used as a reference to compensate for pulse-to-pulse intensity fluctuations. The sample is placed between CaF₂ windows that are separated by a teflon spacer of 100 - 200 μm . The sample is rotated to avoid photo-product formation and long-term heating effects. The transmitted probe and reference pulses are spectrally dispersed with a spectrograph and detected with a 2×32 liquid-nitrogen cooled mercury-cadmium-telluride (MCT) array detector (Infrared Associates).

The reverse micelle samples are made by adding a solution of HPTS (8-hydroxy-1,3,6-pyrenetrisulfonic acid) in water to a mixture of surfactant and apolar solvent. We use two combinations of surfactant and solvent: AOT (sodium dioctyl sulfosuccinate) and isoctane, and BRIJ-30 (polyoxyethylene(4)lauryl ether) and cyclohexane. In both cases the molar ratio of surfactant and apolar solvent is 1:20. The concentration of HPTS in water is chosen such that each reverse micelle contains at most one HPTS molecule. The ratio between the concentration of water and the concentration of surfactant $w = \frac{[\text{H}_2\text{O}]}{[\text{surfactant}]}$ determines the size of the reverse micelles. For AOT reverse micelles we studied samples with $w = 2, 3, 6, 8, 10$ and 15 ; for BRIJ reverse micelles we studied $w = 1, 2, 3, 4, 6, 8, 10, 15$. These values of w correspond to diameters ranging from ~ 1.6 nm to 5.5 nm [69, 120, 171, 192]. A reverse micelle with a diameter of 1.6 nm contains approximately 50 water molecules [171].

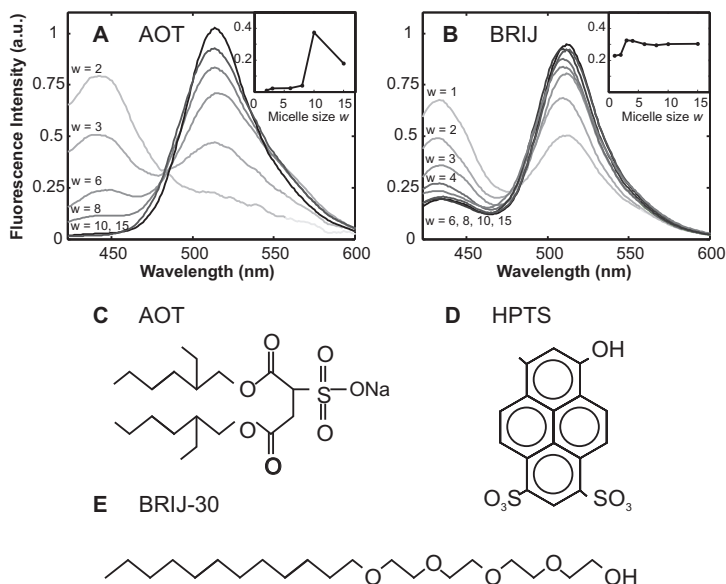


FIGURE 8.1. Steady-state fluorescence spectra of HPTS in reverse micelles with AOT (A) as the surfactant and with BRIJ (B) as the surfactant. The insets show the fluorescence intensity integrated over the entire spectrum for different reverse micelle sizes. (C) The structural formula of AOT (sodium dioctyl sulfosuccinate). (D) The structural formula of HPTS (8-hydroxy-1,3,6-pyrenetrisulfonic acid). (E) The structural formula of BRIJ-30 (polyoxyethylene(4)lauryl ether).

8.3 RESULTS

8.3.1 STEADY-STATE FLUORESCENCE

Figure 8.1 shows fluorescence spectra of HPTS for AOT reverse micelle with $w = 2$ to 15 and BRIJ reverse micelle with $w = 1$ to 15. The fluorescence spectrum of each sample is normalized to the total frequency-integrated fluorescence of that sample. The fluorescence peak at 440 nm corresponds to the excited photoacid ROH^* , and the peak at 520 nm corresponds to the excited conjugate photobase RO^{*-} . For both AOT and BRIJ reverse micelles, the intensity of ROH^* increases relative to that of RO^{*-} with decreasing reverse micelle size. This finding agrees with previous observations, and shows that the proton uptake by water is reduced/slowed down in small reverse micelles [11, 130, 156]. For the AOT reverse micelles, the intensity of ROH^* completely vanishes for the larger reverse micelle sizes, showing that practically all photoacid molecules release their proton well within the fluorescence lifetime upon approaching the bulk limit. In contrast, for the large BRIJ reverse micelles, there remains a small contribution centered at 440 nm. This could be caused by hydrogen bonding of the photoacid molecule to the surfactant, thereby preventing proton

transfer.

The insets of Fig. 8.1 show the frequency-integrated fluorescence intensity as a function of reverse micelle size. These intensities are corrected for the different concentrations of HPTS in each individual sample. This correction is performed by measuring the absorption spectrum of each sample with a steady state UV-Visible spectrometer (Jasco V530) to determine the concentration. For the AOT reverse micelles, the integrated fluorescence becomes relatively small for $w < 10$. This observation indicates the presence of a quenching process in which the excited photoacid molecule undergoes non-radiative decay to the ground state ($\text{ROH}^* \rightarrow \text{ROH}$). For the BRIJ reverse micelles, the integrated fluorescence intensity does not show such a strong dependence on reverse micelle size. Only for very small reverse micelle sizes ($w \leq 2$), a slight decrease in the integrated fluorescence intensity is observed.

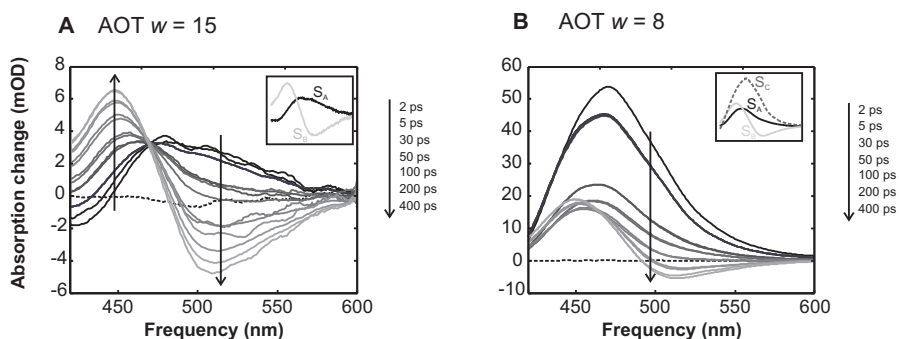


FIGURE 8.2. Femtosecond visible absorption spectrum for AOT reverse micelles with $w = 15$ (A) and $w = 8$ (B). Thick lines show the measured data; thin lines the fitted spectra using the model described in the text. The arrows indicate the direction of pump-probe delay time. Insets show the decomposed spectra found by the model.

8.3.2 FEMTOSECOND VISIBLE PUMP-PROBE

Figure 8.2 shows the transient visible absorption spectra at different delay times obtained for two different AOT reverse micelle sizes ($w = 15$ and $w = 8$). These spectra were collected using the visible pump-probe setup described in the experimental section and illustrated in Fig. 3.7. For large reverse micelles ($w = 15$), the transient spectra strongly resemble the transient spectra observed for a solution of HPTS in bulk water [155]. The spectra show an isosbestic point around 480 nm, indicating that the dynamics are dominated by an interconversion between two different distinct states (ROH^* and RO^{*-}). At early delay times, the spectrum shows a broad absorption centered near 500 nm that is due to the excited state absorption of the photoacid, ROH^* . At

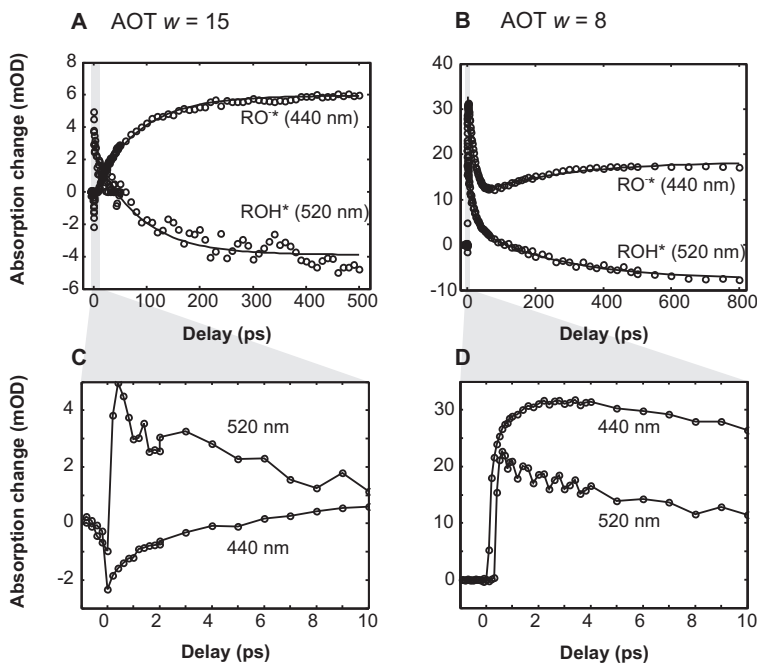


FIGURE 8.3. (A) The signal as a function of pump-probe delay time at a wavelength of 440 and 520 nm for large reverse micelles ($w = 15$). The lines are obtained by fitting the data to Eq. 8.1. (B) The signal as a function of pump-probe delay time at a wavelength of 440 and 520 nm for medium size reverse micelles ($w = 8$). The lines are obtained by fitting the data to Eq. 8.2. Details of the early time dynamics are shown for $w = 15$ (C) and $w = 8$ (D).

large delay times, the spectrum shows an absorption band at 440 nm that is due to the absorption of the excited state of the conjugate photobase RO^{-*} . The spectrum also shows a decrease in absorption at 520 nm due to stimulated emission of the photobase. This stimulated emission is also present at early delay times, but is then overwhelmed by the absorption of the excited state of ROH^* . For medium size reverse micelles ($w = 8$), the spectra look very different and no longer show an isosbestic point (Fig. 8.2B).

Figure 8.3 shows the time evolution of the transient absorption signals measured at wavelengths of 440 nm and 520 nm as a function of delay time. For large reverse micelles (Fig. 8.3A), the signals show a complementary rise and decay at longer delays, reflecting the conversion of ROH^* to RO^{-*} . At short delays, there is a fast (~ 2 ps) rise at 440 nm (Fig. 8.3C), similar to the bulk water case, that is associated with excited state relaxation [167]. For medium size reverse micelles (Fig. 8.3B), both signals (440 and 520 nm) show an initial decay (~ 20 ps), followed by a slow rise at 440 nm (RO^{-*}) and a slow

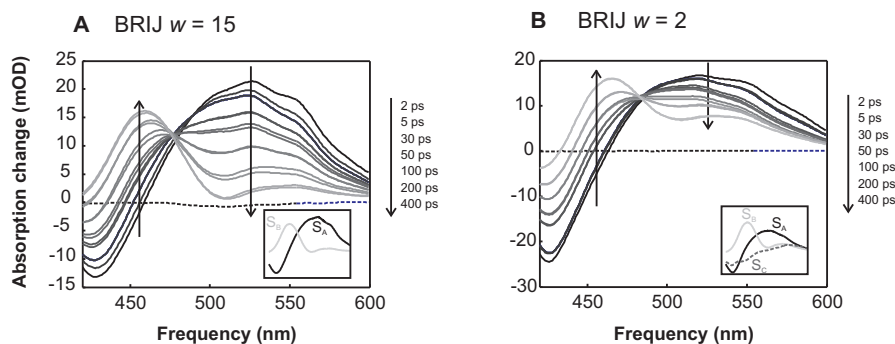


FIGURE 8.4. Femtosecond visible absorption spectrum for BRIJ reverse micelles with $w = 15$ (A) and $w = 2$ (B). Thick lines show the measured data; thin lines the fitted spectra using the model described in the text.

decay at 520 nm (ROH^{-*}). Also in this case, at short delays there is a ~ 2 ps excited state relaxation component that leads to a rise at 440 nm (Fig. 8.3D).

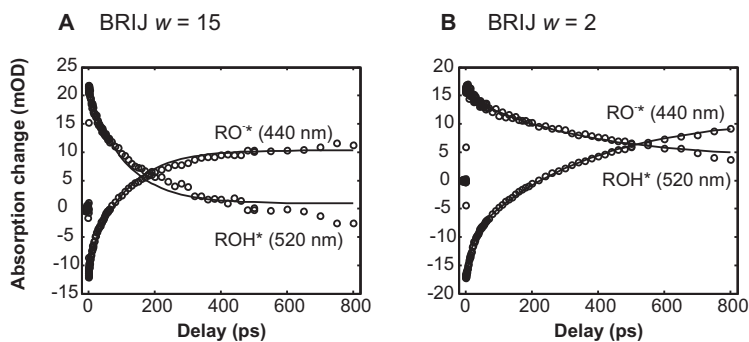


FIGURE 8.5. Delay scans at two frequencies with corresponding fits for $w = 15$ (A) and $w = 2$ (B).

Figure 8.4 shows the transient visible absorption at different delay times for two BRIJ reverse micelles ($w = 15$ and $w = 2$). For all BRIJ reverse micelles, the spectra are quite similar to the spectra observed for bulk water and for large AOT reverse micelles. The dynamics, however, do change with reverse micelle size, as is illustrated in Fig. 8.5. For large BRIJ reverse micelles (Fig. 8.5A), the dynamics are similar to bulk water and large AOT reverse micelles, showing a rise at 440 nm (RO^{-*}) and a complementary decay at 520 nm (ROH^*). For small BRIJ reverse micelles (Fig. 8.5B), there is a small-amplitude fast initial component, followed by a slow rise at 440 nm and a slow decay at 520 nm. The rise and decay are clearly much slower than in the case of the large reverse micelles.

8.3.3 FEMTOSECOND MIDINFRARED PUMP-PROBE

Figure 8.6 shows the transient absorption spectra in the mid-infrared for two different AOT reverse micelles ($w = 15$ and $w = 6$) for different delay times. These spectra were taken with the visible-mid-infrared pump-probe setup described in the experimental section and illustrated in Fig. 3.6. The excitation results in a direct rise of absorption bands at 1480 and 1540 cm^{-1} , which can be assigned to ROH^* . As a result of the deprotonation, these bands decay and a new band grows in at 1500 cm^{-1} , representing the absorption of RO^{-*} [137] [148]. These vibrational bands likely are combinations of aromatic ring distortional modes and stretching modes [108].

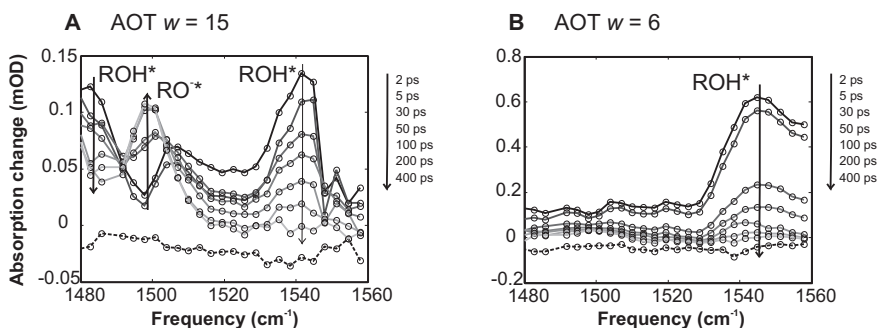


FIGURE 8.6. Femtosecond midinfrared absorption spectrum showing decaying acid bands (ROH^*) at 1480 and 1540 cm^{-1} and a rising base band (RO^{-*}) at 1500 cm^{-1} for an AOT reverse micelle $w = 15$ (A). For a smaller reverse micelles with $w = 6$ only the decay of the acid band at 1540 cm^{-1} is observed (B).

For large AOT reverse micelles ($w = 15$), the spectra in the 1500 cm^{-1} region are nearly identical to the corresponding spectra in bulk H_2O [148]. This finding agrees with the observations in the visible pump-probe data. For smaller reverse micelles ($w = 6$), the measured spectra are different (Fig. 8.6B). These spectra do not show a rise of the RO^{-*} band at 1500 cm^{-1} . In addition, the band of ROH^* at 1480 cm^{-1} is no longer observed.

Figure 8.7A shows the absorption of the photoacid vibration at 1540 cm^{-1} as a function of delay time for four different AOT reverse micelle sizes. The transient signals show the presence of an initial fast component for which the amplitude increases with decreasing reverse micelle size. We also probe the transient spectra in the frequency range between 1850 and 1950 cm^{-1} , which contains the broadband infrared absorption that is attributed to the partially/fully hydrated proton [148] [38]. Figure 8.7B shows the signal of the

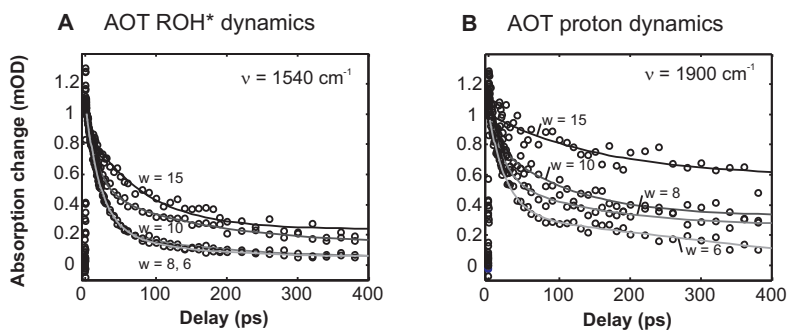


FIGURE 8.7. (A) The dynamics of the ROH* band around 1540 cm^{-1} for a range of reverse micelle sizes ($w = 15, 10, 8$ and 6). (B) The dynamics of the proton continuum averaged between 1850 and 1950 cm^{-1} for the same range of reverse micelle size.

partially/fully hydrated proton as a function of delay time for four different reverse micelle sizes. Again, for large reverse micelles ($w = 15$), the dynamics are similar to that observed for bulk liquid water [148]. As the reverse micelle size decreases, the dynamics develop a fast initial component, similar to what is observed for the dynamics of the ROH* band at 1540 cm^{-1} .

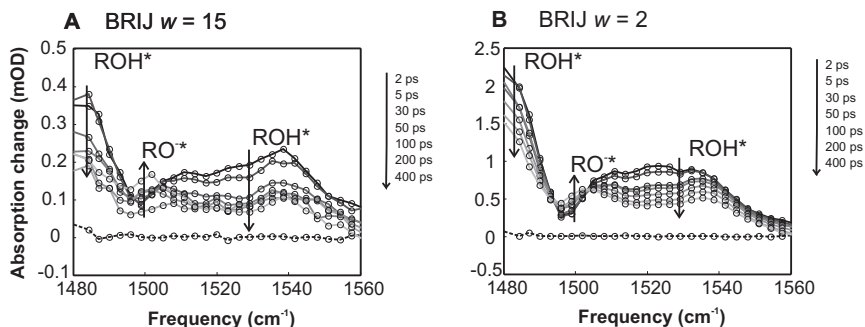


FIGURE 8.8. Femtosecond midinfrared absorption spectrum with decaying acid bands (ROH*) around 1480 and 1540 cm^{-1} and rising base band (RO*) around 1500 cm^{-1} for BRIJ reverse micelles with $w = 15$ (A) and $w = 2$ (B).

In Fig. 8.8, transient mid-infrared absorption spectra at different delays are shown for BRIJ reverse micelles with $w = 15$ and $w = 2$. A striking difference with the mid-infrared spectra observed for the AOT reverse micelles (Fig. 8.6), is that for BRIJ reverse micelles the spectra do not change much with reverse micelle size. Only the RO* band at 1500 cm^{-1} shows a somewhat less pronounced rise for $w = 2$, indicating that there is less deprotonation in this smaller reverse micelle.

8.4 DISCUSSION

For HPTS dissolved in large AOT and BRIJ reverse micelles ($w \geq 10$), the shapes and dynamics of the transient electronic and vibrational spectra are very similar to what is observed for HPTS dissolved in bulk liquid water. This finding is consistent with earlier results from fluorescence measurements and time-correlated photon counting experiments [11, 130, 156] on proton transfer in reverse micelles. It also corresponds well with the observation that the water in large reverse micelles shows very similar molecular dynamics as bulk water [40, 110, 125, 172].

To analyze our results in more detail, we use the excited state proton transfer scheme in Fig. 8.9. For large reverse micelles, we model the transient visible spectra with two spectral components and one interconversion time constant. This time constant is used as a global fit parameter that is fixed for all wavelengths. Hence, we fit the following equation to the absorption change $\Delta\alpha(\nu, t)$

$$\Delta\alpha(\nu, t) = S_B(\nu) + [S_A(\nu) - S_B(\nu)] \cdot e^{-k_{PT}t} , \quad (8.1)$$

with S_A and S_B the spectra of the two components and k_{PT} the interconversion rate. The spectra $S_A(\nu)$ and $S_B(\nu)$ represent the absorption spectra of ROH^* and RO^{-*} , respectively, and k_{PT} represents the rate at which the proton is released from ROH^* . We start the fit after 5 ps, after the very fast initial dynamics – the Stokes shift (~ 1 ps), excited state relaxation (~ 2 ps) and contact-ion pair formation (~ 3 ps) – are complete [154, 155, 167]. The contact ion-pair formation corresponds to a charge transfer state with a weakened OH bond of the photoacid, but for which proton dissociation has not yet taken place. The spectra obtained from the fit to Eq. 8.1 for the AOT and BRIJ reverse micelles are shown in the insets of Figs. 8.2 and 8.4, respectively. The fits to the dynamics are shown with the solid lines in Figs. 8.3 and 8.5.

For large AOT and BRIJ reverse micelles ($w = 15$), we find $k_{PT} = (84 \pm 5 \text{ ps})^{-1}$ and $(110 \pm 5 \text{ ps})^{-1}$, respectively. These values agree well with the bulk value for the proton transfer rate of $(90 \text{ ps})^{-1}$ [128, 155]. Similar dynamics are observed for the vibrational bands of the photoacid and the photobase. For $w = 15$ AOT and BRIJ reverse micelles, the dynamics of the vibrational ROH^* band at 1540 cm^{-1} can be fit well with a single-exponential function. For the AOT reverse micelle we find a rate constant of $(89 \pm 10 \text{ ps})^{-1}$, and for the BRIJ reverse micelle a value of $(129 \pm 15 \text{ ps})^{-1}$. At much longer delays ($> 1 \text{ ns}$), it is expected that the proton transfer dynamics are governed by diffusion and a power law dependence is expected [156].

For smaller reverse micelles with $w < 8$, the dynamics of the transient electronic and vibrational spectra strongly differ from what is observed for bulk liquid water and large reverse micelles. Especially in the case of AOT reverse micelles, we see a number of changes occurring between $w = 10$ and $w = 8$, both in the steady-state fluorescence data and in the time-resolved differential absorption measurements. First of all, the electronic absorption spectrum is vastly different for $w = 8$ (Fig. 8.2). The signal corresponding to ROH^* (at 520 nm) contains a large component that disappears on a fast timescale (Fig. 8.3). Secondly, the vibrational spectrum is very different for $w = 6$ (Fig. 8.6) and also includes a similar fast component (Fig. 8.7A). Finally, the proton continuum for small AOT reverse micelles shows a strong initial decay with a similar time constant (8.7B). The time-resolved measurements indicate that the fast initial process corresponds to a disappearance of ROH^* , without RO^{-*} or a proton signal (H_3O^+) being formed.

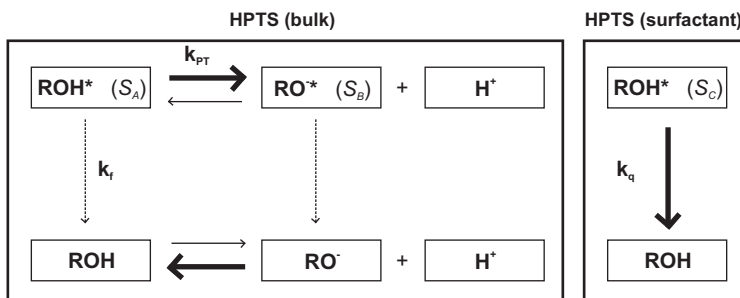


FIGURE 8.9. Scheme describing the dynamics of HPTS, with k_{PT} the proton transfer rate, k_f the fluorescence rate and k_q the quenching rate. In brackets we show the electronic absorption spectra from Eqs. 8.1 and 8.2 that correspond to that state.

For small AOT reverse micelles, this effect is much more pronounced than for the BRIJ reverse micelles. For both reverse micelle systems, the amplitude of the fast contribution increases with decreasing reverse micelle size. This finding and the observation that the fluorescence intensity becomes smaller for decreasing reverse micelle sizes (Fig. 8.1), indicate that the fast initial component comes from a rapid non-radiative decay. Therefore, we model the transient absorption measurements for smaller reverse micelles with two parallel processes: the conversion of ROH^* to RO^{-*} (deprotonation) and the quenching of ROH^* to ROH . We also include the possibility that the spectrum of the HPTS molecules that undergo a rapid non-radiative decay differs from the spectrum of the HPTS molecules that undergo deprotonation. For small reverse micelle sizes ($w \leq 8$) we thus use the following equation to fit the observed absorption changes

$$\begin{aligned} \Delta\alpha(\nu, t) &= S_B(\nu) + [S_A(\nu) - S_B(\nu)] \cdot e^{-k_{PT}t} \\ &+ S_C(\nu) \cdot e^{-k_q t} \quad , \end{aligned} \quad (8.2)$$

where $S_C(\nu)$ corresponds to the electronic absorption spectrum of HPTS molecules that undergo quenching with rate constant k_q . For all small reverse micelle sizes with $w < 8$ we obtain a good fit of the transient electronic response using Eq. 8.2. In addition, we find that the spectra S_A and S_B are nearly identical to the corresponding spectra for large reverse micelles ($w \geq 10$). Additionally, for both AOT and BRIJ reverse micelles ($w < 8$), we find a quenching rate constant k_q of about 20 ps^{-1} , regardless of the reverse micelle size. As expected, the amplitude of the contribution from the spectrum S_C increases for smaller reverse micelles. As the amount of quenching depends on the nature of the surfactant and increases with decreasing reverse micelle size, it seems likely that the quenching involves HPTS molecules that are hydrogen-bonded to the surfactant.

For AOT reverse micelles, some HPTS molecules presumably bind to one of the negatively charged sulfonate groups. This hydrogen bond will result in a change in the electronic structure of the HPTS molecule resulting in a different transient absorption spectrum, namely $S_C(\nu)$ versus $S_A(\nu)$. The change in electronic structure will also influence the vibrational spectrum, especially the absorption bands of the aromatic ring modes. It is found that the ROH* band at 1480 cm^{-1} shows a strong decrease in relative amplitude compared to the ROH* band at 1540 with decreasing reverse micelle size. The band at 1480 cm^{-1} has been assigned to a combination band of stretch and aromatic ring deformation modes [108], and is thus indeed expected to be affected by a change in the electronic structure configuration of the HPTS molecule.

The transient vibrational absorption measurements show very similar dynamics to the transient electronic absorption measurements. Therefore we use a similar fitting scheme for the vibrational absorption measurements. For larger reverse micelles, ($w \geq 10$, the measured transient absorption signals are fit to a single exponential decay. Similarly, for smaller reverse micelles ($w \leq 8$), the transient vibrational absorption signals measured for AOT reverse micelles are fit to a bi-exponential decay, one exponent representing the quenching process, the other exponent the proton transfer. The fast process has a time constant of 20 ps, in good agreement with the transient electronic absorption measurements.

For medium size AOT reverse micelles ($w = 8$), the proton transfer rate k_{PT} is observed to slow down to $(221 \text{ ps})^{-1}$. This observation is in good quantitative agreement with previous measurements of HPTS [11, 130, 156] and 2-naphthol-6,8-disulfonate in AOT reverse micelles [35]. For the smallest AOT reverse micelles ($w = 2$, $w = 3$ and $w = 6$), the signal is strongly dominated by the quenching contribution, making it impossible to extract a reliable deprotonation rate. HPTS in BRIJ reverse micelles shows minimal quenching, and we can deduce the time constant of the proton transfer, even for the small BRIJ reverse micelle ($w = 2$). For this reverse micelle size we find a time constant of proton transfer of 350 ps, which shows that the proton transfer is slowed down by a factor of 4 in comparison to bulk liquid water.

The slowing down of the proton transfer process with decreasing reverse micelle size appears to be caused by the confinement of the water volume, and not by specific interactions with the surfactant, as the HPTS molecules that do interact with the surfactant show rapid quenching. The slowing down of the proton transfer with decreasing reverse micelle size can be explained by the fact that the rate of proton transfer to water is largely determined by the orientational motion of water molecules [1, 16, 165, 168], as discussed in detail in Chapter 7. The reorientation of the water molecules is slowed down considerably in reverse micelles [40, 110, 125], particularly in the region near the surfactant layer.

8.5 CONCLUSION

We studied the effect of the confinement of water on the rate of proton transfer using femtosecond visible and mid-infrared pump-probe spectroscopy. As model systems we study reverse micelles of different sizes and of different surfactant composition. We study reverse micelles with an anionic surfactant (AOT) and with a non-ionic surfactant (BRIJ-30). For both types of reverse micelles, we observe that for large reverse micelles ($w = 15$) the proton transfer shows a similar rate constant k_{PT} of $\sim(90 \text{ ps})^{-1}$ as is observed in bulk liquid water.

For small reverse micelles ($w \leq 8$), we observe two distinct decay processes. Some of the excited photoacid molecules are observed to become rapidly quenched after excitation, with a rate k_q of $\sim(20 \text{ ps})^{-1}$. This fraction is much larger for AOT reverse micelles than for BRIJ reverse micelles, and the quenching contribution increases with decreasing reverse micelle size. The quenching is likely caused by specific interactions between HPTS and the surfactant molecules. The remaining fraction of the excited photoacid molecules undergo proton transfer with a slower rate than in bulk liquid water. For small BRIJ reverse micelles with $w = 2$, we observe a time constant for proton transfer of 350 ps, which is about 4 times slower than in bulk liquid water. The slowing down of the proton transfer with decreasing micelle size is similar for AOT and BRIJ reverse micelles. Therefore, this slowing down appears not to be caused by specific interactions with the surfactant, but rather by the confinement of the water volume.

9 WATER DYNAMICS IN A HYDROPHOBIC HYDRATION SHELL

We study the influence of the amphiphilic compound tetramethylurea (TMU) on the dynamical properties of water, using dielectric relaxation spectroscopy in the regime between 0.2 GHz and 2 THz. This technique is capable of resolving different water species, their relative fractions and their corresponding reorientation dynamics. We find that the reorientation dynamics of water molecules in the hydration shell of the hydrophobic groups of TMU is between 3 (at low concentrations) and 10 (at higher concentrations) times slower than the dynamics of bulk water. The data indicate that the effect of hydrophobic groups on water is strong but relatively short-ranged. With increasing temperature, the fraction of water contained in the hydrophobic hydration shell decreases, which implies that the overall effect of hydrophobic groups on water becomes smaller.

9.1 INTRODUCTION

The interaction between hydrophobes and water is of fundamental chemical interest, and highly relevant for biochemistry and biology. Molecules that are essential in biological processes, such as proteins, change the structure and dynamics of the surrounding water shell, whereas this water hydration layer, in turn, affects the functioning of these biomolecules [9]. In hydrophobic interactions, a distinction is generally made between small and large hydrophobes. For the former (length <1 nm), water molecules can adopt orientations that allow the hydrogen-bond network to go around the solute, whereas in the latter case (length >1 nm), the extended solute surface makes it impossible for adjacent water molecules to maintain a complete hydrogen-bonding network with the surrounding liquid. [31]. The hydration of (small) hydrophobes has been studied using numerous techniques. Besides theoretical work [31, 84, 147, 179], it has been a popular subject for experimental investigations. Earlier studies examined mainly thermodynamic properties [44], and found that upon mixing hydrophobes and water, the system experiences negative changes in enthalpy and excess entropy. Later studies examined structural and dynamical proper-

ties on a molecular level [8, 18, 27, 47, 52, 63, 67, 133, 135, 136, 145, 152, 187].

The various measurements and computer simulations have so far led to some consistent and some contradictory conclusions. The negative changes in enthalpy and excess entropy from Ref. [44] were originally thought to be caused by an enhancement in the structure of the water network around the hydrophobic solute. This enhancement was, however, not observed in neutron diffraction measurements that probe the structural properties of aqueous solutions of hydrophobic molecules [18, 152]. New insights were gained by NMR, dielectric relaxation (DR) and femtosecond infrared pump-probe (fs-IR) studies of the reorientation dynamics of water molecules hydrating hydrophobes. These studies showed that it is not the structure of water that is affected by the presence of the hydrophobe, but rather the reorientational dynamics: water in the hydrophobic hydration shell was found to be slowed down in its rotational motion [27, 47, 52, 63, 67, 133, 135, 136, 145, 187].

From these DR and fs-IR studies it was concluded that a strong retardation occurs of the rotational dynamics of a limited number of water molecules hydrating the hydrophobic groups. These results are consistent with NMR measurements [47, 63, 133, 145, 187], which measure the average reorientation time of all water molecules. As a result, in NMR the size of the hydration shell needs to be assumed to find the degree of retardation of the hydration shell water. fs-IR measurements do not have this disadvantage, since the full orientational correlation function is measured. However, fs-IR measurements have the disadvantage that the time window is restricted to about 10 picoseconds, which limits the possibility of extracting time scales that are much outside this window. Hence, these measurements unfortunately cannot quantify the time scale of the slowed reorientation, nor determine precisely how many water molecules are slowed down, or why they are slowed down.

Classical molecular dynamics (MD) simulations have shown a relatively modest retardation effect for amphiphilic molecules, which was assigned to be a purely geometric effect: the excluded volume that is occupied by the solute [84] prevents a water molecule in the hydration shell from being approached by another water molecule to which it would hydrogen-bond after the reorientation process. These simulations furthermore suggested that for most solutes the major effect in the hydration dynamics comes from the hydrophilic group [158], which does not agree with the observation that the effect on the water dynamics scales with the size of the hydrophobic part, as found by NMR [133, 145] and fs-IR [135].

The key in solving these apparent controversies is being able to resolve simultaneously, and in a model-independent way, the different water species, their relative fractions and their corresponding reorientation dynamics. To this end, we combine in this study two complementary dynamical techniques, to reach a better molecular level understanding of hydrophobic hydration of the

prototypical hydrophobe tetramethylurea (TMU). GHz-THz DR measurements over 4 decades in frequency space were performed for TMU:water mixtures over a wide range of concentrations and the results are compared to literature data from fs-IR, as measured by Rezus et al. [136]. GHz-THz DR measurements were also performed for a TMU:water mixture at different temperatures in order to get more clarity on whether the number of hydration shell water molecules with slowed down reorientation dynamics depends on temperature.

9.2 EXPERIMENTAL

Dielectric relaxation measurements probe the macroscopic polarization of a sample as a function of frequency, which in the case of an uncharged polar liquid, reflects the reorientation of dipoles, as explained in Chapter 2. In this chapter, we combine electrical^a and optical sources, to cover a large range of probing frequencies (200 MHz - 2 THz). This makes this technique a powerful tool for investigating polar liquids that exhibit much varying reorientation times.

The samples were mixtures of TMU (1,1,3,3-Tetramethylurea, >99% purity, used as purchased from Sigma Aldrich) and Millipore grade water. For the concentration-dependent studies, mixtures were prepared with different ratios of TMU molecules per water molecules, expressed in terms of $w = \frac{[\text{TMU}]}{[\text{H}_2\text{O}]}$. The studied concentrations were $w = 0.005, 0.009, 0.018, 0.036, 0.07, 0.18, 0.25, 0.5, 1, 3$, and pure TMU ($w \rightarrow \infty$). For studying the temperature dependence, a mixture with $w = 0.07$, corresponding to a molality of 4 mol/kg or a molarity of 2.7 mol/L at room temperature, was used.

The complex permittivity of the mixtures was determined between 200 MHz and 50 GHz using a frequency-domain reflectometer based on an Agilent 85070E dielectric probe kit, connected to an Agilent E8364B vector network analyzer (VNA) in conjunction with an electronic calibration module (Agilent N4693B) [61]. The VNA was operated in one-port reflection mode and was used to determine the complex reflection coefficient, which after analysis using Agilent software yielded the dielectric spectrum of the sample. For all measurements, a calibration was done with an air sample and a mercury sample representing a short circuit. Further calibrations were done following Ref. [143] with three appropriate liquids with known dielectric properties from the set of H₂O, *N,N*-Dimethylacetamide [15], Propylene carbonate [14], Benzonitrile [14] and 1-Butanol [124]. All liquids were used as purchased from Sigma Aldrich. The temperature of the sample was controlled with a thermostat to an accuracy of ± 0.05 °C. For the frequency range between 60 and 89 GHz, a double-beam interferometer with variable path-length transmission sample cells was used [13].

^aThe measurements in the GHz frequency range were conducted in the group of Prof. R. Buchner at the University of Regensburg (Germany) using electronically created and detected guided waves.

For the frequency region between 0.4 and 1.2 THz, a time-domain spectrometer was used (see Chapter 3, Fig. 3.4). This THz setup was based on terahertz generation in a ZnTe (110) nonlinear crystal (see Section 2.2.3), using 800 nm pulses with a duration of ~ 110 fs from a Ti-Sapphire laser. The time-dependent electric field strength was measured using the electro-optic effect in a second ZnTe crystal with a variably delayed pulse of 800 nm with a duration of ~ 110 fs (see Section 2.2.4 for details). A frequency domain analysis of the THz pulse, with a duration of ~ 3 ps, transmitted through an empty cell (Infrasil quartz, path length $103 \pm 0.5 \mu\text{m}$) and the THz pulse transmitted through a filled sample cell yielded the complex frequency-dependent permittivity of the sample. This was done through an analysis where the (multiple) reflection and transmission coefficients for all transitions (air-quartz-sample-quartz-air) were taken into account [72]. A mechanical device was used to position a mixture sample and a pure water sample alternately in the focus of the THz beam (4 seconds cycle time) [165]. The measurement of pure water with known dielectric properties was then used to calibrate the dielectric properties of the mixture that was measured in parallel, as explained in Section 4.1.2. The temperature-dependent measurements were done using a sample cell with a variable optical path length, equipped with a Peltier element, as in Ref. [163].

9.3 RESULTS AND DISCUSSION

9.3.1 CONCENTRATION DEPENDENCE

DATA AND FIT RESULTS The results of the combined GHz-THz dielectric relaxation measurements are shown in Fig. 9.1 for a wide range of TMU-water mixtures, measured at 25 °C. First of all, it is interesting to note that upon increasing the concentration of TMU, the peak of the imaginary permittivity (Fig. 9.1A) first shifts to lower frequencies (corresponding to slower reorientation) and then back to higher frequencies upon further increasing the concentration. It is also clear that the imaginary permittivity has a rather asymmetric shape at those concentrations where the reorientation is slowest. For pure water, two relaxation processes are needed to describe the complex permittivity up to ~ 1.2 THz [46, 139], as described in Section 2.2.2.

It is apparent from the highly asymmetric signal at intermediate concentrations (e.g. for $w = 0.07$) that the addition of TMU introduces a third, slower Debye relaxation process. Thus, we used the following equation to describe all frequency-dependent permittivities $\hat{\epsilon}(\omega)$

$$\hat{\epsilon}(\omega) = \frac{S_{\text{slow}}}{1 + i\omega\tau_{\text{slow}}} + \frac{S_{\text{bulk}}}{1 + i\omega\tau_{\text{bulk}}} + \frac{S_{\text{fast}}}{1 + i\omega\tau_{\text{fast}}} + \epsilon_{\infty} \quad . \quad (9.1)$$

Here, the first term describes the reorientation of the slow component, with a

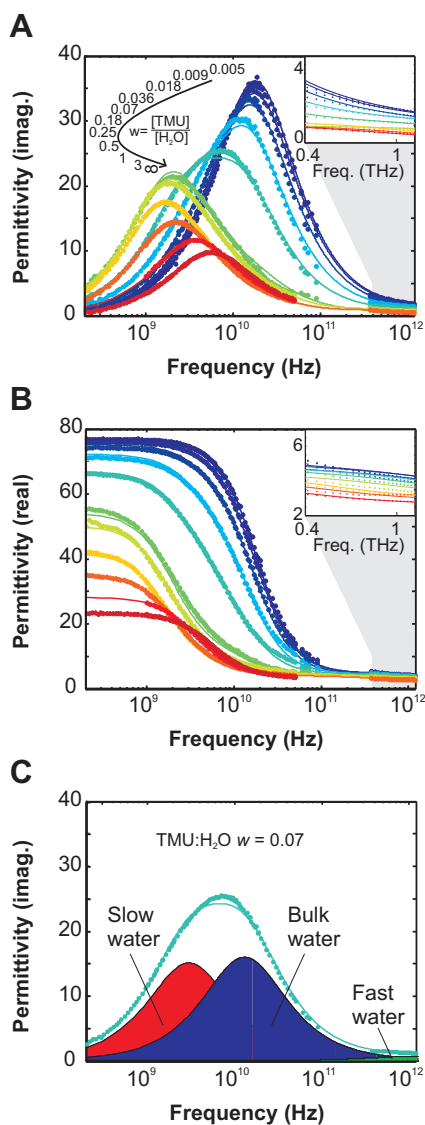


FIGURE 9.1. Combined data (dots) and fits (lines) from GHz and THz dielectric relaxation spectroscopy, showing the imaginary (ϵ'') (A) and real (ϵ') (B) permittivity as a function of frequency for different TMU concentrations, given in ratios of $w = \text{TMU}:\text{H}_2\text{O}$. The insets show the frequency dependence in the THz regime more closely. (C) A decomposition into the three dielectric relaxation processes – slow hydration shell water (red), bulk-like water (blue) and fast water (green) – for $w = 0.07$.

strength S_{slow} and a time scale τ_{slow} . This slow component contains both contributions from slowly reorienting water molecules and from the reorientation of the solute TMU molecules. The second term describes the reorientation of bulk-like water with a strength S_{bulk} and a time scale τ_{bulk} . Finally the third term describes a fast dipolar reorientation process that can be attributed to undercoordinated water molecules [186], which has a strength S_{fast} and a time scale τ_{fast} . The remaining high frequency limit permittivity is given by ϵ_{∞} . The high frequency limit is where the transition occurs from the region where relaxation processes are active to the region where resonant processes are active, such as intermolecular hydrogen-bond stretching, located at 5.4 THz [46, 186], and intramolecular OH-stretching, located at 100 THz (3400 cm^{-1}). The strengths S_i are indicative of the dipole density, i.e. reflect the number of water molecules that participate in the corresponding Debye processes.

In fitting the data to Eq. 9.1, it was assumed that the relative error in the permittivity was constant over the whole frequency range. The results of the fits are shown as lines in Fig. 9.1, where the three relaxation strengths S_i and time scales τ_i are not constrained. Clearly Eq. 9.1 describes the data very well, over nearly 4 decades of frequencies and more than 2 decades of concentrations. The fit results for the strengths S_i are shown in Fig. 9.2A; the fit results for the reorientation time scales of the bulk-like water (τ_{bulk}) and slow component (τ_{slow}) are shown in Fig. 9.3, along with the viscosity data from Ref. [118].

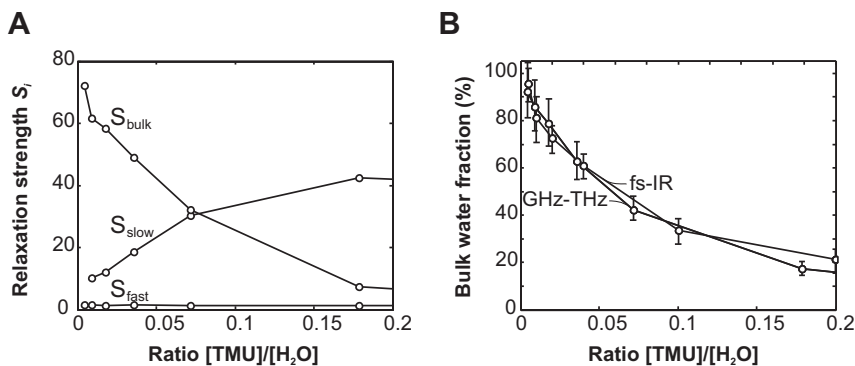


FIGURE 9.2. (A) The extracted relaxation strengths S_i for the slow component, the bulk-like water and the fast water. (B) The extracted fraction of bulk-like water, based on the fits to the GHz-THz data and the fs-IR data, as a function of TMU concentration.

The fit results for the relaxation strengths S_{slow} , S_{bulk} and S_{fast} were used to extract the fractions of the three components. Since the slow mode contains contributions from water dipoles and TMU dipoles, we determine the fraction of bulk-like and fast water. For the large range of concentrations studied, it was

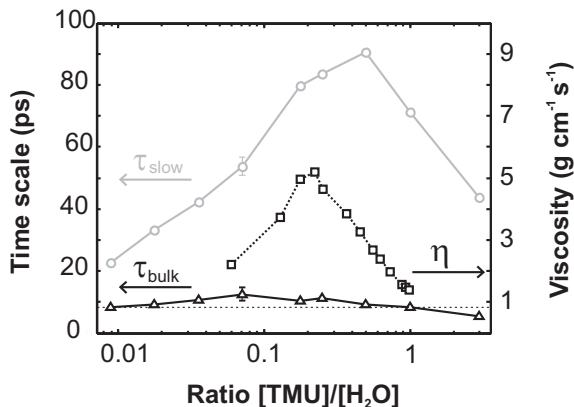


FIGURE 9.3. The extracted reorientation time scale for the slow hydration shell water $\tau_{\text{slow}}(c)$ (\circ), the reorientation time scale for bulk-like water $\tau_{\text{bulk}}(c)$ (\triangle), and the viscosity (\square ; data from Ref. [118]) as a function of TMU concentration. The dashed line represents the reorientation time for bulk water $\tau_{\text{bulk}}(0)$. Error bars are given as an indication.

most appropriate to use the following equation, based on the solvent-normalized Cavell equation [25,27], to extract the fraction of bulk-like water, as a function of TMU concentration c

$$f_{\text{bulk}}(c) = \frac{[S_{\text{bulk}}](c)}{[S_{\text{bulk}} + S_{\text{fast}}](0)} \frac{c_{\text{H}_2\text{O}}(0)}{c_{\text{H}_2\text{O}}(c)} \frac{\tau_{\text{bulk}}(0)}{\tau_{\text{bulk}}(c)} \frac{(2\epsilon_s(c) + 1)\epsilon_s(0)}{\epsilon_s(c)(2\epsilon_s(0) + 1)} \quad , \quad (9.2)$$

where $c_{\text{H}_2\text{O}}(c)$ is the concentration (in mol/L) of water in a TMU-water mixture of concentration c (also in mol/L). In this equation, we take into account the effects of dilution (second term), dipole-dipole correlations (third term) and local field effects (fourth term). It is assumed that the effective dipole moment of water in these solutions is the same as in neat water. For the fraction of fast water, we replace S_{bulk} in the numerator by S_{fast} and remove $\frac{\tau_{\text{bulk}}(0)}{\tau_{\text{bulk}}(c)}$.

INTERPRETATION The relaxation strengths of the three components show a clear dependence on the concentration (see Fig. 9.2A). The fraction of water with fast dynamics (the process with time scale τ_{fast}), showed an increase from 2% at $w = 0$ to 13% at $w = 1$. This is related to an undercoordination of the water network and is consistent with the observation that the linear absorption spectrum of the OD-stretch vibration shifts to higher frequencies for higher concentrations of TMU in TMU-water mixtures (where the water contained a small fraction of D_2O) [136]. This could indicate an overall weakening of the hydrogen-bond network, as concluded previously from isotope-substituted neutron diffraction of a small hydrophobe in water [152] and from theoretical

calculations [49,99]. Furthermore, a similar observation of an increased fraction of undercoordinated water was made for weakly hydrated amphiphilic lipid molecules, using THz DR spectroscopy [163].

The fraction of water with the bulk-like time scale τ_{bulk} decreases with increasing concentration of TMU, as illustrated in Fig. 9.2, while simultaneously the relaxation strength of the slow component increases. At low concentrations this increase is linear with the TMU concentration, showing that this component is associated with water molecules hydrating TMU and TMU itself. The relative contributions of TMU and water to the slow component depends on the concentration and have been calculated from the relaxation strength of the slow component, compared to the relaxation strength of pure TMU. For instance, for $w = 0.02$, the slow component amounts to $\sim 17\%$ of the total response of which $\sim 3\%$ is due to TMU and $\sim 14\%$ due to water. For $w = 0.2$, the slow component constitutes $\sim 85\%$ of the total response of which $\sim 25\%$ is due to TMU and $\sim 60\%$ due to water. Therefore, for $w < 0.2$ the slow component is dominated by slowly reorienting water molecules that hydrate TMU.

Up to a concentration of $w = 0.07$ (~ 4 mol/kg), the bulk-like fraction decreases linearly with concentration (see Fig. 9.2B), which agrees well with previous NMR [145] and fs-IR [135, 136] studies. At higher concentrations, overlapping hydration shells and weak aggregation effects [5] might occur. The fraction of water that is associated with the bulk-like time scale indeed behaves very much like bulk water: there is very little dependence of the time constant on concentration. For increasing TMU concentrations, the time scale increases somewhat (less than a factor 1.5) and then decreases again (Fig. 9.3). Hence, it appears that these water molecules are surrounded by other water molecules and behave bulk-like at all concentrations.

The fraction of water that exhibits slower reorientation dynamics is significantly slower at all concentrations. At very low concentrations (< 0.1 M), the slowdown factor is ~ 3 , in good agreement with an earlier DR study [52]. At a moderate concentration of $w = 0.018$ (1 mol/kg), the reorientation dynamics of the slow water fraction is 4 times slower than that of bulk water. This indicates that for these mixtures, there is a significant retardation effect of the reorientation dynamics of water hydrating TMU. The observed time scales also agree with the results of classical molecular dynamics simulations by Wei et al., who found the first order time correlation function for a 5 mol/L TMU-water solution to be still non-zero after 50 ps [179], but are significantly longer than was calculated in the classical MD simulations by Laage and Hynes [84]. The present observations are consistent with NMR measurements results.

The longest reorientation time is found for a TMU-water mixture with about two water molecules per TMU molecule ($w = 0.5$). This time scale (~ 90 ps) is more than 10 times longer than the reorientation time of bulk water. For these mixtures, the reorientation of TMU and its hydration shell

is also much slower than the reorientation of TMU molecules in pure TMU. This suggests that the small water molecules and the larger TMU molecules together form a dense jammed system. The concentration dependence of the reorientation time correlates very well with the concentration dependence of the viscosity [118]. The viscosity also shows a maximum at a ratio where there are only a few water molecules per TMU, as illustrated in Fig. 9.3. For $w = 0.25$ the viscosity is ~ 5 times higher than for pure water and for pure TMU.

The strong effect of TMU on the dynamics of water even at low concentrations, shows that this osmolyte has a strong hydrophobic hydration effect. Hence, it is to be expected that the hydrophobic groups of TMU also favorably interact with the hydrophobic groups of proteins, which could explain why TMU is very effective in stimulating the denaturation of proteins.

COMPARISON WITH FS-IR DATA The GHz-THz DR data can be compared with the results from polarization-resolved femtosecond infrared pump-probe studies of the reorientation dynamics in TMU-water mixtures by Rezus et al. [136], where it was found that a significant fraction of water was present with slower reorientation dynamics. This fs-IR technique studies directly the reorientation dynamics of individual water molecules with high temporal resolution (~ 150 fs). In these experiments, the OD-stretch vibration of a subset of HDO molecules in H_2O (4% D_2O in H_2O) was excited by a resonant infrared pump pulse with a frequency of ~ 75 THz (2500 cm^{-1}). Molecules with their OD group preferentially aligned along the polarization axis of this infrared pump pulse were most efficiently tagged. With a variable time delay, the system was then interrogated by a probe pulse, which measured the number of tagged molecules parallel and perpendicular to the excitation axis. An appropriate ratio of the two signals divides out the effects of vibrational relaxation and provides the anisotropy parameter $R(t)$, which (corrected for heating due to the excitation according to Ref. [134]) as a function of pump-probe delay time t then reflects the orientational dynamics of the probed water molecules. This technique makes it possible to directly monitor the water dynamics during a time window of ~ 10 ps. Due to the limited time window, fs-IR studies [135, 136] concluded that the slow hydration shell water is associated with a reorientation time of $\tau_{\text{slow}} > 10$ ps.

GHz-THz dielectric relaxation measurements and fs-IR pump-probe spectroscopy are sensitive to the same reorientation processes of water molecules. However, there are four main differences between the two techniques, which are fortunately well understood. First of all, (*i*) GHz-THz dielectric relaxation measurements are sensitive to the inverse Fourier transform of the time derivative of the *first* order time correlation function, whereas fs-IR measurements are sensitive to the decay of the *second* order time correlation function [19, 20, 164]. Due to this difference, the reorientation time found with fs-IR is ~ 2.5 times shorter than the reorientation time scale found with DR, assuming jump reori-

entation of water molecules [81]. Secondly, *(ii)* GHz-THz dielectric relaxation measurements probe the dynamics of the macroscopic polarization of the sample, while fs-IR measurements probe the dynamics of isolated water molecules. As a result, dielectric relaxation measurements can contain contributions due to local fields and dipole-dipole correlations [19, 20, 164]. Due to the local field effects and dipole-dipole correlations the total difference between the reorientation times measured by GHz-THz DR and by fs-IR amounts to a factor of ~ 3.4 for neat water, as experimentally found in Ref. [164]. Furthermore, *(iii)* the two techniques are sensitive to the reorientation of different axes of the molecule: the dipole vector in the case of GHz-THz DR and the OD-vector in the case of fs-IR [162]. If water molecules would reorient in an anisotropic fashion, i.e. in preferred directions, this could also result in different reorientation time scales for the two techniques. Finally, *(iv)* GHz-THz measurements not only probe the orientational dynamics of water dipoles, but also of the solute TMU molecules. Hence, the comparison can be made up to $w = 0.2$, as in this concentration range the slow component is dominated by water molecules hydrating TMU.

In order to determine if the GHz-THz DR results are in agreement with the data from previous fs-IR measurements, we use the slow reorientation time scales as found from the GHz-THz DR measurements (corrected by a factor of $\zeta \approx 3.4$)^b [164] to describe the fs-IR anisotropy decays

$$R(t) = A_{\text{bulk}} \cdot e^{-\zeta \cdot t / \tau_{\text{bulk}}(0)} + A_{\text{slow}} \cdot e^{-\zeta \cdot t / \tau_{\text{slow}}} \quad . \quad (9.3)$$

Here, $\frac{A_{\text{bulk}}}{A_{\text{bulk}} + A_{\text{slow}}}$ and $\frac{A_{\text{slow}}}{A_{\text{bulk}} + A_{\text{slow}}}$ represent the fraction of water molecules that exhibit bulk-like dynamics and the fraction of water that has slow dynamics, respectively. In Fig. 9.4 the data from Ref. [136] are shown, together with bi-exponential fits based on Eq. 9.3. Only the amplitudes are adjustable parameters, since the bulk-like reorientation time $\tau_{\text{bulk}}(0)$ is fixed to the one for neat water and the slow reorientation time is inferred from the GHz-THz DR measurements, which makes these fits highly constrained. The fast water process (with time scale τ_{fast} , see Eq. 9.1) that is present in the GHz-THz DR data, does not show up in the fs-IR studies.

The fits show that the time constants obtained from DR yield a good description of the fs-IR results. Therefore, the corresponding fractions of bulk-like and slow water can also be compared. The results for the bulk-like fractions from GHz-THz DR and fs-IR spectroscopy as a function of TMU concentration are shown in Fig. 9.2B. This figure shows that the results of the two techniques are consistent not only in terms of the inferred reorientation time scales, but also in terms of the fractions of bulk-like water, over a large range of concentrations. The quantitative agreement between the results of the GHz-THz DR

^bAssuming that the conversion factor ζ mainly comes from local field effects, we calculate [20] that ζ decreases by less than 5% at very high TMU concentrations. This validates the assumption of a concentration-independent conversion factor.

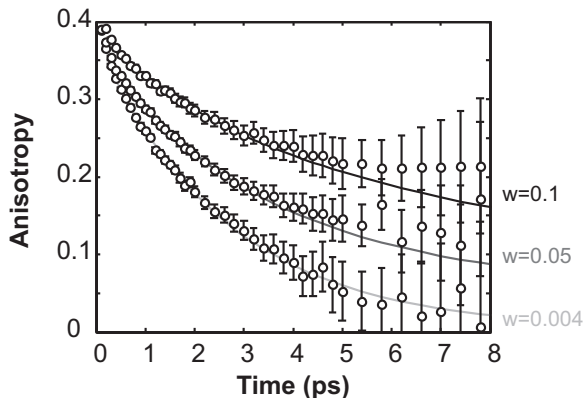


FIGURE 9.4. The anisotropy decay as a function of pump-probe delay time for a number of TMU concentrations, from Ref. [136]. To describe these data (lines), the resulting time scales from the GHz-THz measurements τ_{slow} and $\tau_{\text{bulk}}(0)$ were used, after correction for the difference between macroscopic first order (GHz-THz) and microscopic second order (fs-IR) correlation function measurements.

and fs-IR spectroscopies confirms that the reorientation dynamics of water in solutions of TMU can be described in terms of two major subensembles, namely bulk-like water and slow water hydrating TMU.

The fractions of bulk-like water as extracted from GHz-THz DR and fs-IR measurements agree well for the whole concentration range (Fig. 9.2B). In the low concentration regime (up to $w = 0.07$) the fraction of bulk water indicates that each TMU molecule slows down the dynamics of about 8-12 water molecules, corresponding to 2-3 water molecules per methyl group. This agrees well with fs-IR studies on mixtures of TMU:water and water with other methyl-group containing amphiphiles, where 2 slow water molecules (4 OH groups) were found per methyl group [135, 136]. Previous fs-IR and NMR studies showed that the effect of hydrophobic solutes on the reorientation scales quite well with the number of methyl groups contained in the solute [133, 135, 145]. Hence, the water network appears to fold around the individual methyl groups, rather than interacting with the hydrophobic part of TMU as if it were a single extended hydrophobic surface. We also find that the number of slowed water molecules is significantly smaller than the number of water molecules contained in the geometric hydration shell. This result can be rationalized by the notion that the water molecules contained in the geometric hydration shell show a strong variation in positions and orientations. Some of the water molecules within the shell can thus experience hydrogen-bond and reorientation dynamics as in bulk water, while for a selected part, these dynamics are strongly slowed

down.

The time scale of ~ 10 ps of the hydrophobic hydration shell is in excellent agreement with the time scale found for TMU:water solutions of 1.5 mol/kg at room temperature [122]. However, this time scale is now found to be dependent on concentration, varying from ~ 10 ps at 1 mol/kg to ~ 25 ps at higher concentrations (second order time scales).

9.3.2 TEMPERATURE DEPENDENCE

In Fig. 9.5, the GHz-THz dielectric spectra are shown for TMU-water mixture with $w = 0.07$ (4 mol/kg). As in bulk water [23], at higher temperatures the frequency-integrated permittivity decreases due to a decrease in dipole density and increased thermal fluctuations of the dipoles. However, at THz frequencies the imaginary part of the permittivity increases because the dielectric response extends to higher frequencies as a result of faster reorientation at elevated temperatures. In order to quantify the behavior of the mixture, the data were fit with Eq. 9.1 (see lines in Fig. 9.5). In the fitting procedure - like in the previous section - error weighing was used, based on a constant relative error in the permittivity. Equation 9.1 is clearly capable of fitting the data very well for all temperatures. We can determine the activation energy of the reorientation of the hydration shell if we assume that for all water molecules in the hydration shell the reorientation becomes equally accelerated by an increase in temperature. Under this assumption, we obtain the reorientation times as shown in Fig. 9.6A. In this figure we also show Arrhenius fits (connected lines) to the extracted time scales. According to Arrhenius' law $\tau \propto e^{E_{\text{act}}/k_{\text{B}}T}$, where E_{act} is the activation energy, in this case of the reorientation, and k_{B} is Boltzmann's constant. The extracted activation energies are $E_{\text{act}}^{\text{bulk}} = 12$ kJ/mol, for the bulk-like water fraction, and $E_{\text{act}}^{\text{slow}} = 22$ kJ/mol for the water in the hydration shell. The activation energy of the bulk-like water fraction is in excellent agreement with the activation energy of pure water from the THz reflection study of Ref. [140].

The temperature-dependent data from our GHz-THz DR measurements are compared with the fs-IR study by Petersen et al. [122]. In this study, 1.5 mol/kg solutions of TMU and tertiary butyl alcohol were studied. It was found that both hydrophobic molecules are surrounded by a hydration shell water with slower dynamics. It was furthermore observed that the relative speedup of the reorientation with temperature was larger for slow hydration shell water than for bulk-like water. An Arrhenius fit showed that the overall activation energy of the slow water fraction was almost twice as large as the overall activation energy of the bulk-like water fraction [122]. Similar observations were done in NMR studies [47, 187]. Hence, the present results of our GHz-THz measurements are in excellent agreement with the results of these previous studies.

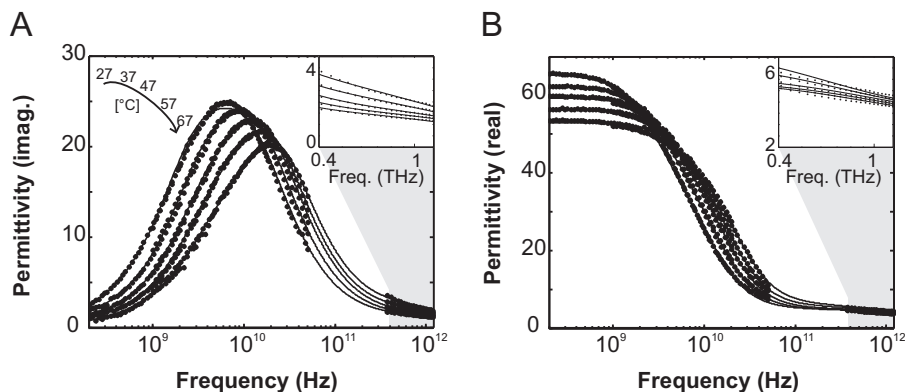


FIGURE 9.5. The imaginary (A) and real (B) part of the permittivity for a solution of TMU in water (4 mol/kg) at different temperatures. The insets show the frequency dependence in the THz regime more closely.

In Fig. 9.6B, we show the result of the fit for the GHz dielectric spectrum at 57 °C. Clearly, the fit is not optimal: the measured spectrum is much more asymmetric than the fit result. A much better fit can be obtained by allowing the bulk-like water fraction and the slow fraction to change with temperature. The resulting curve fits the GHz spectrum quite accurately. In Fig. 9.6C, the time scales of the reorientation processes of the two sub-ensembles using this approach are given as a function of temperature. In Fig. 9.6D the corresponding bulk-like and slow fractions are presented. With increasing temperature, the bulk-like water fraction increases while the slow water fraction decreases. Hence, we find that the speedup of the reorientation of the water molecules hydrating TMU is the result of two effects: (i) the transfer of water molecules with hydration shell character to bulk-like character; (ii) the speedup of the reorientation of water molecules that keep their hydration-shell character. The THz-GHz technique allows us to make a distinction between these two contributions. The two contributions are schematically illustrated in Fig. 9.7.

Figure 9.6C shows that for the water molecules that keep their hydration shell character, the speedup of the reorientation with temperature is the same as for bulk water. This indicates that the reorientation mechanism of water molecules in the shell is probably not very different from that of water molecules in the bulk liquid. It has been proposed that in bulk liquid water the reorientation of an OH group proceeds through a transient bifurcated hydrogen-bond configuration [81]. The much slower reorientation of water in the hydration shell thus suggests that the rate at which the hydrogen-bond structure evolves to a bifurcated state is much lower in the hydration shell than in the bulk liquid.

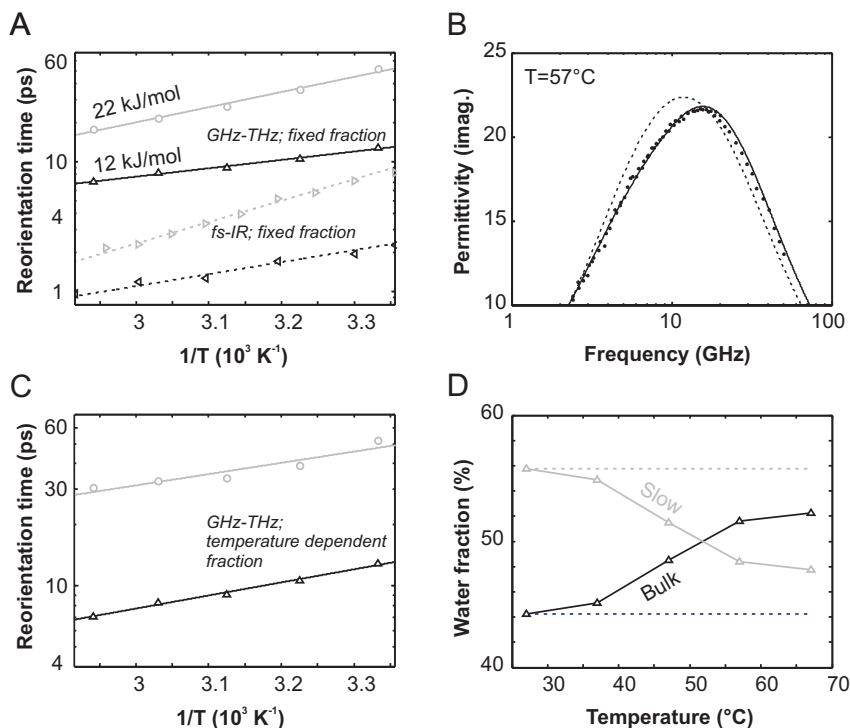


FIGURE 9.6. (A) The fit results when the fractions of bulk-like and slow water are fixed for the GHz-THz measurements (\circ, Δ), together with fs-IR measurements ($\triangleright, \triangleleft$) from Ref. [122], where the same assumption was made. (B) A comparison of the fit for TMU $w = 0.07$ at 57°C , where the fraction of bulk-like is free (line) and where it is kept constant over temperature (dotted line). (C) The reorientation time for bulk-like water (Δ) and TMU/slow water (\circ) as a function of $1/T$ with fits where the water fractions were free. Please note that the slope of the slow water species in this case does not represent the activation energy of the hydrophobic hydration shell water, as the number of water molecules in this ensemble is not constant with temperature. (D) The fraction of bulk-like and slow water as a function of temperature and the fixed fractions for the alternative fit (dotted line).

The transition of water molecules from hydration-shell character to bulk-like character suggests that the size of the hydrophobic hydration shell decreases with temperature. Of course, the water molecules will not significantly change their position in the solution upon a temperature increase. Therefore, the transition to bulk-like character implies that the range over which the hydrophobic molecular groups affect the water hydrogen-bond network decreases. Since the hydrophobe is surrounded by the same geometrical hydration shell

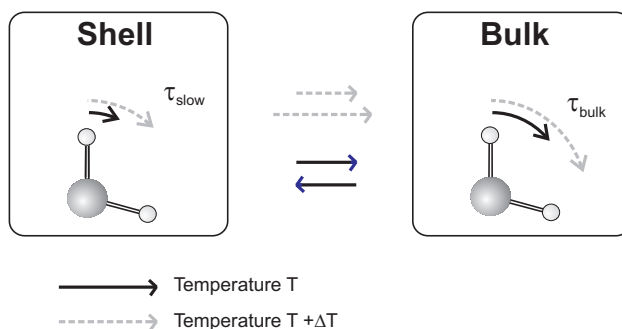


FIGURE 9.7. Graphical representation describing the chemical equilibrium between bulk-like water and hydration shell water as a function of temperature, as well as the temperature dependence of the reorientation time. The lower temperature is described by straight arrows; the higher temperature by dashed arrows.

at all temperatures, this points to a decrease in the correlation length of the hydrogen-bond network around hydrophobic surfaces. At higher temperatures, the hydrogen-bond network is more dynamic and less coordinated and therefore the effect of the hydrophobic group will have a shorter persistence length. The effect of a smaller effective hydration shell at higher temperatures is thus also connected with more pronounced interfacial density fluctuations [105], and is consistent with the increases of excess entropy and enthalpy changes of the hydrophobic hydration [153].

The decrease of the hydrophobic hydration shell with temperature shows that the retardation effect on the reorientation is not a simple excluded volume effect, as recent computer simulations have suggested [84]. The excluded volume is a purely geometrical effect: the reorientation of water molecules adjacent to a hydrophobe experience an excluded volume, where no new hydrogen-bond partners can be found, leading to slower reorientation. When the temperature is changed, the molar volumes of water and TMU stay more or less constant^c, meaning that the geometry of the system is unaltered. Hence, the fraction of slow hydration shell water would not be expected to change with temperature. The observation that there is a change in the fraction of slow hydration shell water with temperature shows that other effects play a role, in addition to the excluded volume effect.

^cThe density of the TMU-water mixture with $w = 0.07$ has been measured with a vibrating tube densimeter (Anton Paar DMA60/601 HT) and showed that the density decreased by less than 2% between 25 and 67 °C.

9.4 CONCLUSION

By measuring the GHz-THz dielectric response in TMU-water mixtures over a range of concentrations and for different temperatures, a better molecular level understanding of hydrophobic hydration has been obtained. We find that there is a substantial retardation of the dynamics of water directly surrounding the hydrophobe, where the reorientation dynamics are between 3 (at low concentrations) and 10 (at higher concentrations) times slower than the dynamics of bulk water. It is furthermore clear that the effect of the hydrophobe is relatively short-ranged: the dynamics of 8-12 (at concentrations below $w = 0.07$) water molecules per TMU molecule show substantial retardation; the other water molecules behave bulk-like.

By changing the temperature for a TMU:water mixture with about 14 water molecules per TMU molecule ($w = 0.07$), it was shown that the overall activation energy of the slow hydration shell water is about twice as large as for bulk water. Since the GHz-THz measurements can separately determine the reorientation time scales and fractions of slow and bulk-like water, it was found that the fraction of bulk-like water increases with increasing temperature, thus explaining the higher activation energy for hydration shell water. This temperature effect indicates that the hydrophobic interaction decreases with temperature. It furthermore shows that the retardation effect is not the result of a simple excluded volume effect. Instead, the retardation results from a more collective frustration of the structural dynamics of the hydrogen-bond network of water by the hydrophobic molecular groups.

10 WATER DYNAMICS IN DOPC LIPID MODEL MEMBRANES

We study hydrated model membranes, consisting of stacked bilayers of 1,2-Dioleoyl-*sn*-Glycero-3-Phosphocholine (DOPC) lipids, using terahertz time-domain spectroscopy and infrared spectroscopy. Terahertz spectroscopy enables the investigation of water dynamics, owing to its sensitivity to dielectric relaxation processes associated with water reorientation. By controlling the number of water molecules per lipid molecule in the system, we elucidate how the interplay between the model membrane and water molecules results in different water dynamics. For decreasing hydration levels, we observe the appearance of new types of water dynamics: the collective bulk-like dynamics become less pronounced, whereas an increased amount of both very slowly reorienting ('slow') and very rapidly reorienting ('fast') water molecules appear. Temperature-dependent measurements reveal the interconversion between the three distinct types of water present in the system.

10.1 INTRODUCTION

Insights into membrane hydration, i.e. the interplay between water and membrane molecules is essential for a complete understanding of biological cell functioning. Biological membranes constitute the barrier between the inside and the outside of the cell. The principal building blocks of membranes are lipids: amphiphilic molecules that spontaneously self-assemble into bilayers when in contact with water. The details of the resulting membrane, such as the curvature of the bilayer, its mechanical properties, the lipid density in the bilayer and the thermodynamics of the self-assembly process, depend intimately on the hydration of the hydrophilic lipid head groups. The many biochemical tasks performed at these interfaces (e.g. the controlled transfer of ions or nutrients across the membrane barrier) are performed by membrane proteins that span the membrane. The correct functioning of these trans-membrane proteins, in turn, has often been shown to depend critically on their interaction with water and their lipid neighbors [88]. Such interactions are greatly influenced by the details of the hydrogen-bonding capabilities of lipid head groups: for example, replacing a hydrogen atom by a (hydrophobic) methyl group can influence

local water density and hydrogen-bond network strength sufficiently to render neighboring transmembrane proteins inactive [51]. Furthermore, hydration of membranes is closely related to the fluidity of the membrane, which in turn is of fundamental importance for phenomena like membrane fusion or drug transport [28].

The structural complexity and dynamics of water interacting with membranes has been studied using various spectroscopic tools. Much information has been obtained by using techniques such as NMR [178] or (time-resolved) mid-infrared spectroscopy [173, 174, 191]. NMR experiments have provided insights into the orientational order within the water-shell around lipid head-groups and have helped in clarifying the different rates of lateral and normal translational diffusion of water at lipid-water interfaces [178]. Femtosecond time-resolved pump-probe mid-infrared spectroscopy (fs-IR) has an improved time resolution, in principle allowing one to access dynamical processes such as changes in hydration, which have been predicted to occur on (sub-)picosecond timescales [142, 173, 174, 191].

Recently, terahertz (THz) spectroscopy has emerged as a powerful tool for investigating biomolecular systems and their interaction with water [10, 41, 55, 56, 71]. For instance, THz absorption studies in the 2-3 THz region on protein hydration have provided detailed information about the spatial extent, the nature and dynamics of the aqueous hydration shell of proteins [41, 56]. The strength of THz spectroscopy to study the structure and dynamics of water lies in the fact that the dielectric response in the THz region directly reflects the reorientation of water dipoles occurring on picosecond timescales. This same effect also gives rise to strong absorption of THz radiation by aqueous systems, limiting the THz penetration depth to $\sim 100 \mu\text{m}$. Here, we apply dielectric relaxation spectroscopy in the THz domain to the study of hydration in membrane-models composed of stacks of 1,2-Dioleoyl-sn-Glycero-3-Phosphocholine (DOPC) lipid bilayers in order to investigate the influence of membrane confinement on the water reorientation dynamics. DOPC has been chosen since it is an unsaturated lipid generally used as a component of model membranes mimicking real ones [70]. We have studied the THz dielectric relaxation of these membranes by varying their level of hydration and by changing the ambient temperature, in order to investigate the possible heterogeneity of water within DOPC membranes.

10.2 EXPERIMENTAL

10.2.1 SAMPLE

The experiments were performed on membrane models made of stacked 1,2-Dioleoyl-sn-Glycero-3-Phosphocholine (DOPC) bilayers (see Fig. 3.1E). DOPC

was purchased from Avanti Polar Lipids Inc. Solutions of DOPC in pure chloroform were prepared at a concentration of about 15 g/L. Drops of these solutions were deposited on a fused quartz window, with the chloroform let to evaporate. It is known that in this way stacks of lipid bilayers are formed by self-assembly [70]. Samples with a thickness of a few hundred micrometers were readily realized by successive depositions. These samples were then inserted in a sample holder with a variable thickness of the sample chamber. The sealed cell was first exposed to a dry nitrogen flow to dehydrate the lipid and was subsequently put in contact with a reservoir at controlled humidity. This allowed us to control the degree of hydration from $x \approx 0.3$ water molecules/lipid molecule to $x \approx 11$ water molecules/lipid molecule. The cell was equipped with Peltier modules in order to control the temperature. The temperature could be varied between -20 °C and 150 °C.

10.2.2 MEASUREMENT TECHNIQUES

Spectra in the frequency range $0.4 - 1.2$ THz were measured by means of a spectrometer based on THz time-domain spectroscopy (see Chapter 3, Fig. 3.4 for details of the setup). In this setup, a broad bandwidth single-cycle THz pulse (~ 3 ps) is generated by optical rectification in ZnTe of a 110 fs laser pulse, centered at a wavelength of 800 nm. The field strength (rather than intensity) of the THz pulse transmitted through the sample is measured in the time domain by means of electro-optic sampling using a small part of the 110 fs pulse for probing at suitable time-delay the quasi-instantaneous THz field strength inside the electro-optic crystal. Each sample was held in a temperature-controlled sample holder with sample chamber of variable thickness. By measuring the THz transmission of each sample for different thicknesses, the complex dielectric function $\hat{\epsilon} = \epsilon' - i\epsilon''$ of the samples was extracted as a function of angular frequency ω , as described in Chapter 4.1.1. In addition, for each sample a linear mid-infrared spectrum between 2000 and 4000 cm^{-1} was recorded using a standard double beam spectrometer (Perkin-Elmer 881).

10.3 ANALYSIS

In the frequency region that we study ($0.4 - 1.2$ THz), the main process that is active is dielectric relaxation. The dielectric relaxation response of water contains information on how well the permanent dipoles associated with water molecules can keep up with oscillating fields of a certain frequency. At driving frequencies that exceed the reorientation frequency of water, the driving field can be resonant with infrared active modes that do not involve dielectric relaxation. In pure water, one such mode appears around 5.4 THz (180 cm^{-1}), which is attributed to hydrogen-bond stretching [46,186]. Furthermore, a (very weak) low frequency mode is located around 1.8 THz (60 cm^{-1}), which has

been attributed to hydrogen-bond bending [46, 139, 188]. We therefore restrict our analysis to frequencies up to 1.2 THz, to ensure that our data only include contributions from dielectric relaxation.

For pure water at room temperature, dielectric relaxation can be described with the double Debye relaxation model [46, 68, 138–140, 186]

$$\hat{\epsilon}(\omega) = \frac{S_1}{1 + i\omega\tau_D} + \frac{S_2}{1 + i\omega\tau_2} + \epsilon_\infty \quad (10.1)$$

Here, the first (main) term represents the dielectric relaxation process with relaxation strength S_1 and a time constant of $\tau_D \approx 8$ ps (the Debye time) for bulk water at room temperature. The second term has a strength S_2 and a (shorter) timescale τ_2 . The fast component in the dielectric relaxation of pure water is usually attributed to rotation or translation of water molecules that are not involved in hydrogen bonding or involved in fewer hydrogen bonds [186]. We shall refer to water molecules that exhibit dielectric relaxation with timescale τ_2 as 'fast' water molecules.

In the case of a mixed system of hydrated DOPC lipid bilayers, the dielectric response is significantly modified from the bulk water response. First of all, the response will consist of a contribution due to DOPC and a contribution due to water. The dielectric response of pure DOPC has an absorption peak in the MHz region that is associated with headgroup rotation, as a result of the dipole moment of the headgroup that contains a negatively charged phosphate group and a positively charged choline group [70]. We verified that the response of pure DOPC in the GHz-THz region is low and dispersionless; it can therefore be incorporated into the parameter ϵ_∞ . Secondly, due to a volumetric lowering of the water content, the dielectric relaxation strengths due to water reorientation S_1 and S_2 will decrease. Finally, it has been established with dielectric relaxation spectroscopy that for stacked bilayer systems of DOPC and DMPC, a resonance occurs below 1 GHz that has been ascribed to water molecules that are so strongly bound, that their reorientation rate is reduced by orders of magnitude [70]. These water molecules could have slower dynamics due to interaction with local electric fields or due to clathrate formation. Here, we will refer to these water molecules as slow water. These slow water molecules have a response that is shifted out of the THz window: they are invisible to THz spectroscopy, as they cannot reorient on timescales that correspond to the THz spectral window. The presence of these slow water molecules will lead to a further lowering of the values of S_1 and S_2 in Eq. 10.1. The presence and quantity of bound water molecules can be determined from combining the THz measurements with independent mid-IR linear absorption spectroscopy, which we use to independently quantify the overall OH-bond density.

In our analysis, we use Eq. 10.1 to determine the amount of bulk-like water (resonance at $1/2\pi\tau_D$) and the amount of fast water (resonance at $1/2\pi\tau_2$).

These amounts are reflected in the values of the relaxation strengths S_1 and S_2 . Since the resonance due to slow (resonance <1 GHz) water is outside our THz window, we do not need to add a third relaxation process - which would appear as an additional term in Eq. 10.1 - to account for the slow water. Rather we infer the amount of slow water by subtracting the amount of bulk-like and fast water from the total amount of water obtained from infrared spectroscopy. Thus we are able to quantify the relative amounts of 3 types of water in this system: bulk-like, fast and slow: the first two directly from the THz spectra, and the latter from a comparison of the THz spectra with the IR spectra. Despite the fact that the resonance of bulk-like water (~ 18 GHz at room temperature) lies outside our experimental window (0.4 - 1.2 THz), it still contributes significantly to our signal (especially to the imaginary part of the dielectric function ϵ''). To restrict the number of free parameters, we fix τ_D to its value for bulk water. This means that we assume the presence of water molecules whose reorientation dynamics are similar to the dynamics in bulk water. The assumption that the reorientation time of part of the membrane-bound water corresponds to that of bulk water is justified by (i) the observation of a significant fraction of bulk-like water in fs-IR measurements of hydrated lipid bilayers [191], and (ii) by microwave measurements of hydrated DOPC lipid membranes, where a dielectric relaxation resonance is found at the same location as in the case of bulk water (at 20 GHz for 25 °C) [79].

Our extraction procedure consists of two steps. (1) First we fit our results for $\hat{\epsilon}(\nu)$ to Eq. 10.1. This yields the parameters S_1 and S_2 , from which we know the amount of bulk-like and fast water in the system. (2) Then we extract the amount of slow water using these parameters and the total amount of water in the system, as determined from our linear infrared spectra. We use the following relations to calculate the fractions of bulk water f_{bulk} , fast water f_{fast} and slow water f_{slow} [54]

$$\begin{aligned}
 \text{(a)} \quad f_{\text{bulk}} &= \frac{c_0}{c_{\text{H}_2\text{O}}} \frac{S_1}{S_{1,\text{pure}} + S_{2,\text{pure}}} , & (10.2) \\
 \text{(b)} \quad f_{\text{fast}} &= \frac{c_0}{c_{\text{H}_2\text{O}}} \frac{S_2}{S_{1,\text{pure}} + S_{2,\text{pure}}} , \\
 \text{(c)} \quad f_{\text{slow}} &= 1 - f_{\text{bulk}} - f_{\text{fast}} .
 \end{aligned}$$

In these equations, $c_{\text{H}_2\text{O}}$ is the concentration of solvent water molecules in the solution determined from mid-IR linear absorption experiments and c_0 represents the concentration of water molecules of pure water (55 mol/L). S_1 and S_2 are the relaxation strengths of the bulk-like and fast water in our system, respectively, and $S_{1,\text{bulk}}$ and $S_{2,\text{bulk}}$ correspond to the relaxation strengths of pure water, taken from Ref. [186].

10.4 RESULTS

10.4.1 LINEAR INFRARED SPECTRA

First, we measure the linear infrared absorption spectra of our samples to determine the number of water molecules per lipid molecule, $x = c_{\text{H}_2\text{O}}/c_{\text{lipid}}$. This is done by comparing the amount of infrared light absorption in the CH-stretch region, a measure for the number of lipid molecules, with the absorption of the OH-stretch vibration of water molecules. The procedure for extracting x is calibrated by recording linear spectra of a dehydrated DOPC sample and adding known amounts of water to the sample. The data for a number of different hydration levels are shown in Fig. 10.1A. These spectra are normalized to the peak of the OH-stretch vibration at $\sim 3400 \text{ cm}^{-1}$. The results are summarized in Table I.

TABLE I. Sample characteristics

RH	x (water/lipid)	%wt	$c_{\text{H}_2\text{O}}$ (mol/L)	c_{lipid} (mol/L)
0%	0.3	0.69%	0.49	1.64
47%	3.8	8.7%	5.7	1.49
67%	5.5	12.6%	7.8	1.42
83%	6.5	14.9%	9.0	1.39
93%	8.4	19.2%	11.1	1.32

The values that we find for x are in excellent agreement with previous results using X-ray diffraction [58]. The values for $c_{\text{H}_2\text{O}}$ and c_{lipid} are calculated from x , using the molecular weight of water and DOPC (18 and 786 g/mol, respectively) and the density of water and DOPC (1000 and 1300 g/L, respectively). These concentrations will be used for later analysis (see Section 10.5). We also show in more detail the region of the OH-stretch vibration for the different samples (see Fig. 10.1B). Clearly, the OH-stretch vibration shifts to lower frequencies upon binding of water to the lipids, indicating the presence

of water molecules that exhibit stronger hydrogen bonding. However, for lower hydration levels, an additional peak is visible at higher frequencies. This peak originates from water molecules that are involved in relatively weak hydrogen bonding. In our analysis, we assume that the infrared absorption cross sections for CH and OH are independent of hydration level.

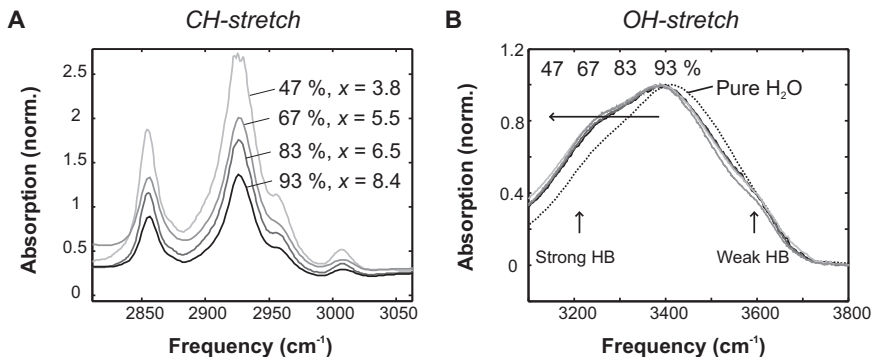


FIGURE 10.1. (A) The linear spectra of lipid bilayers with different hydration levels. These spectra are normalized to their absorption of the OH-stretch vibration and hence indicate the amount of lipid in the system with respect to water. (B) In the OH-stretch region, a clear red-shift of the center frequency can be observed upon decreasing the hydration level, which corresponds to the stronger hydrogen bonds between water and the phosphate group. In addition, a small peak can be seen on the blue side of the spectrum, which corresponds to weaker hydrogen-bonded or free water molecules.

10.4.2 VARYING THE HYDRATION LEVEL

In Fig. 10.2 we show the measured dielectric responses of 5 different samples at relative humidities of 0, 47, 67, 83 and 93%, corresponding to a water fraction of $x = 0.3, 3.8, 5.5, 6.5$ and 8.4 . It is apparent that the dielectric response is largely dispersionless for the pure lipid, and that an increase in the water density results in an increase in the dielectric response. These data can be described very well using Eq. 10.1, with τ_D fixed to its bulk water value. The imaginary part of the dielectric response clearly shows the onset of a resonance at a lower frequency. This resonance cannot belong to the DOPC headgroup reorientation or the slow water, since these modes are invisible in our THz window. Therefore the resonance is very likely to correspond to the relaxation process with time constant $\tau_D \approx 8$ ps, i.e. reorientation of hydrogen-bonded water molecules. A similar frequency dependence can be observed in the THz region for samples of pure water [46, 68, 138–140, 186, 188]. The observation of the onset of this resonance indicates that indeed our system contains water molecules that have reorientation dynamics that are similar to bulk water

molecules.

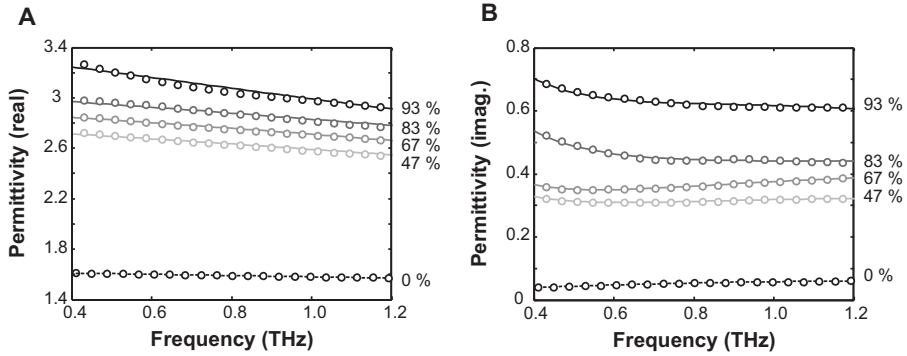


FIGURE 10.2. The real (ϵ') and imaginary (ϵ'') part of the dielectric response of hydrated bilayers with different relative humidities. The lines are fits to the data, as explained in the text.

TABLE II. Fit parameters and extracted water fractions

RH	S_1	S_2	τ_2 (fs)	% slow	% bulk	% fast
0%	0.16	0.12	110	57 %	25 %	18 %
47%	3.9	0.53	89	41 %	52 %	7 %
67%	4.3	0.67	78	52 %	43 %	6 %
83%	7.8	0.69	82	29 %	66 %	6 %
93%	8.8	0.89	121	34 %	60 %	6 %
Pure H ₂ O [186]	74.9	1.8	250	—	97.7 %	2.3 %

The retrieved model parameters are summarized in table II. It can be seen that the parameters S_1 and S_2 increase with increasing water content, as expected. The values for τ_2 are a factor of 3 lower for lipid-bound water compared to the bulk. Figure 10.3 shows the fractions of slow, bulk-like and fast water as a function of lipid hydration. Clearly, a significant portion of the water molecules does not behave as bulk water, but is involved in much slower reorientational dynamics. The relative amount of fast water, compared to bulk water, is significantly larger for hydrated lipid bilayers than for bulk water. Especially in the case of DOPC with very low hydration, the fraction of fast water seems to be significant.

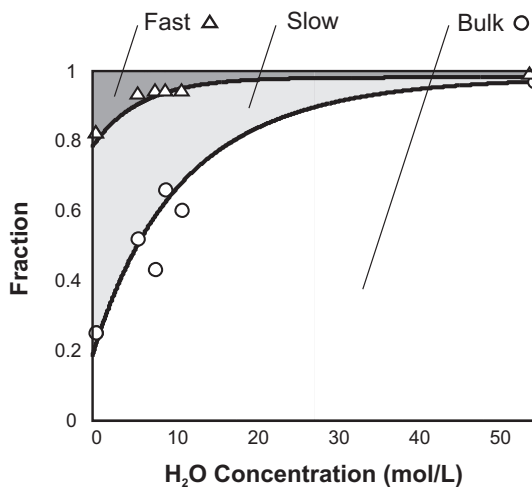


FIGURE 10.3. The fractions of slow water f_{slow} , bulk water f_{bulk} and fast water f_{fast} from Eqs. 10.2a–c as a function of water concentration. The lines are mono-exponential guides to the eye.

10.4.3 VARYING THE TEMPERATURE

We have performed temperature-dependent measurements on DOPC lipid membranes with a number of different hydration levels. For these samples we find the same qualitative trends in the fit parameters as the data presented before: the presence of slow water and an increased amount of fast water. For a relative hydration level of 58%, we show the temperature dependence of the dielectric response in Fig. 10.4. Other samples with different hydration levels yielded qualitatively similar temperature-dependent results. The data in Fig. 10.4 have been fit to Eq. 10.1 with the parameter τ_D fixed to its bulk water value for different temperatures, taken from Ref. [139]. We can use Eq. 10.1,

because it is known from MHz dielectric relaxation measurements that the reorientation time of slow water is too large to give a significant contribution to the dielectric response in our frequency window [70].

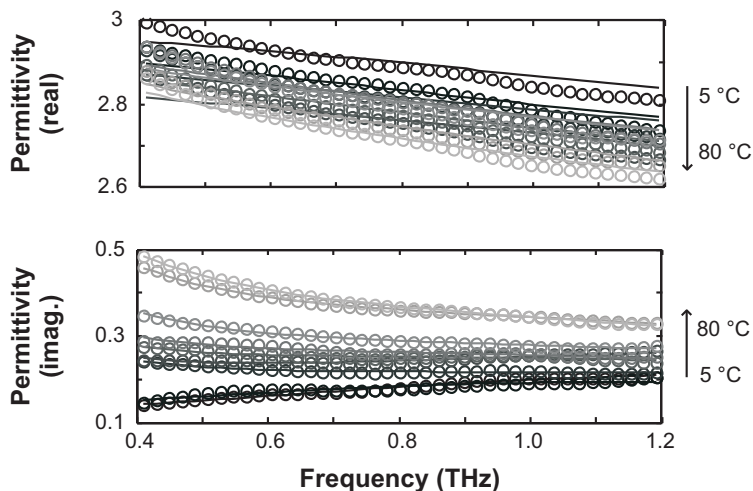


FIGURE 10.4. The real (ϵ') and imaginary (ϵ'') part of the dielectric response of hydrated bilayers with different temperature, from 5 °C to 80 °C, for 58% RH. The lines are fits to the data, as explained in the text.

We show the temperature dependence of the parameter S_1 for the case of pure water (from Ref. [23]) and for the bulk-like component of the hydrated DOPC lipid membranes in Fig. 10.5A. In Fig. 10.5B, the parameters S_2 and τ_2 are shown as a function of temperature for our system and for the case of pure water (from Ref. [186]). The line through the data points that we measured for τ_2 is the same fit that was used for pure water [186], scaled down by a factor 3.

10.5 DISCUSSION

The main observation is that in hydrated lipid bilayers a change in the water dynamics occurs: upon decreasing the hydration level, the amount of water obviously decreases and there is *(i)* an increased *relative* amount of slow water and *(ii)* an increased *relative* amount of fast water, as compared to bulk water. We will discuss these observations in the following.

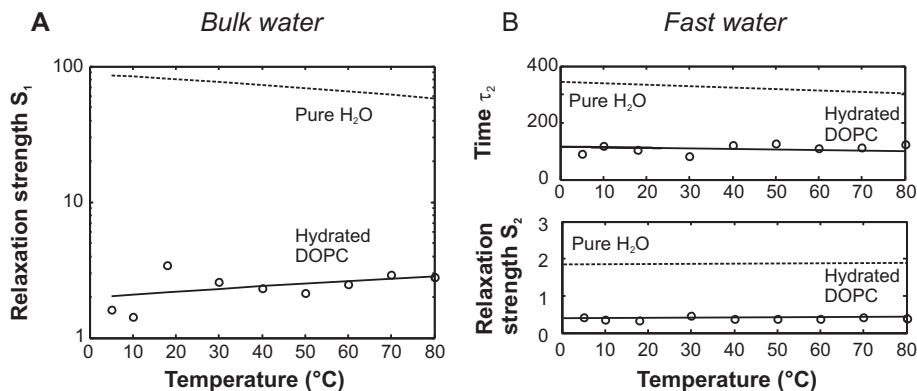


FIGURE 10.5. (A) The temperature dependence of the bulk water parameter S_1 for the case of pure water (dashed line, from Ref. [23]) and the case of bulk-like water molecules in our model membranes (data points and line). (B) The temperature dependence of the fast water parameters τ_2 and S_2 for the case of bulk water (dashed line, from Ref. [186]) and for our system (data points and line).

10.5.1 SLOW WATER

The presence of slow water is evident from the reduced values of S_1 , which are lower than one would expect just based on the volumetric lowering of the water content. This means that there are water molecules that have a reorientation time that is significantly longer than the reorientation time of bulk water. We have found that the relative number of slow water molecules increases with decreasing hydration (see Table II and Fig 10.3). The presence of slow water molecules is also consistent with the observation that the OH-stretch frequency shifts to lower frequencies. This shift indicates that strong hydrogen bonds are formed, which indicate a slower reorientation.

The presence of (slow) water in the phosphocholine headgroup region of lipids such as DOPC and DMPC (1,2-Dimyristoyl-sn-Glycero-3-Phosphocholine) has been previously experimentally observed by MHz dielectric relaxation [70], NMR [59], electrical conductivity [64], X-ray and neutron diffraction and scattering [30,76,181] and fs-IR [173,174,191] measurements. Most experimental techniques can not determine accurately to which lipid groups the water molecules are bound. In Ref. [191], it is proposed that the slow water consists of water molecules surrounding the phosphate group of the phosphocholine headgroup [191] of DMPC, since a slowing down of the anisotropy decay (a measure that is directly related to the reorientation time) is observed. However, similar fs-IR measurements by Rezus et al. have shown that the presence of methyl groups near water molecules, results in a much slower decay of the anisotropy [135]. This means that the slowing down of the anisotropy decay in Ref. [191] could in fact also indicate slow water in the

vicinity of the choline group of the model membranes, since this group contains three methyl groups. Unfortunately, our measurements are unable to distinguish whether slow water is located around the phosphate or the choline group region. We do observe that, depending on the hydration level, only 1 to 4 water molecules per lipid molecule exhibit a slowing down of their reorientational dynamics.

10.5.2 BULK-LIKE WATER

The temperature-dependent dielectric functions show an increase in the imaginary part of the dielectric function for increasing temperatures (see Fig. 10.4). Since we are not directly sensitive to the slow water in our frequency window, this increased dielectric response indicates that the fraction of bulk-like water increases. Indeed, the temperature dependence of the parameter S_1 , shown in Fig. 10.5A is remarkably different for the case of pure water compared to the case of hydrated DOPC lipid bilayers: whereas in pure water the molecules exhibit a *decrease* in relaxation strength at elevated temperatures, instead a small *increase* is observed for membrane-bound water. This clearly indicates that upon increasing the temperature, a conversion takes place from slow water to bulk-like water. This is a similar observation as in the case of hydrophobic hydration shells of tetramethylurea, where the fraction of bulk-like water also increased with increasing temperature (see Chapter 9).

10.5.3 FAST WATER

We observe a substantially larger fraction of fast water molecules for hydrated DOPC lipid bilayers, compared to bulk water (see Fig. 10.3). This observation indicates the increased presence of water molecules with very weak or even absent hydrogen bonds in our hydrated bilayers. This interpretation is corroborated by the observation of a clear blue shoulder in the linear infrared spectra in the OH-stretch region (see Fig. 10.1). Furthermore, it is in agreement with fs-IR measurements of DMPC lipid bilayers that were hydrated using D_2O with a low water-lipid ratio ($x = 0.5 - 2$) [174]. In these measurements, it was observed that the anisotropy decay for strongly blue-shifted OD-stretch frequencies includes a large ultrafast (<150 fs) component. This is likely to be associated with rapidly orienting weakly bonded or free OD bonds. Finally, two-dimensional infrared spectroscopy of hydrated 1-palmitoyl-2-linoleyl phosphatidylcholine (PLPC) has shown that $\sim 50\%$ of the water molecules form only one hydrogen bond [173], compared to the coordination number of ~ 4 in bulk water. These singly hydrogen-bonded water molecules can contribute significantly to a fast component in the dielectric relaxation.

The temperature-dependent measurements show that the fast reorientation timescale τ_2 and the relaxation strength S_2 change only slightly as a function

of temperature (see Fig. 10.5B). A similar small effect was observed by recent broadband THz measurements on bulk water [186]. However, the fast timescale that we find in this system is three times faster than in the case of bulk water. This increased reorientation rate could be caused by a lower average number of hydrogen bonds in the system, where perhaps a larger amount of singly hydrogen bonded or free water molecules is present, leaving one or two dangling OH bonds that are free to rotate.

To identify the binding location of these rapidly reorienting OH dipoles is not trivial. In Ref. [191], the water molecules with a blue-shifted OH-stretch vibration have been attributed to water molecules in the hydrophobic hydrocarbon region. However, it seems unlikely that water molecules would reside in this energetically less favorable region, especially in the case of very weak hydration. The largest relative amount of fast water was observed in the DOPC bilayers with hydration at 0% relative humidity, where $x < 1$. It is most likely that the few water molecules that are present in this system, would be bound to either the phosphate, the choline or the carbonyl group [141]. However, these water molecules might be involved in only one hydrogen bond. The water molecule will then have one very slowly reorienting OH group (the one involved in strong hydrogen bonding) and one rapidly reorienting OH group (the one that is not involved in hydrogen bonding). Since our dielectric relaxation measurements are sensitive to fluctuations of the permanent dipole moment of a water molecule, a singly hydrogen-bonded water molecule will show a fast reorientation component. When the hydration level is increased, water molecules can start forming hydrogen bonds with other water molecules, resulting in an increase in the fraction of bulk-like water. This indicates that upon increasing the hydration level, water molecules develop their collective dynamical nature. However, even at high hydration levels, a significant fraction of free or semi-free water molecules persists in the hydrated DOPC bilayers.

10.6 CONCLUSION AND OUTLOOK

Using terahertz time-domain spectroscopy on hydrated lipid bilayers with different hydration levels, we find three distinct types of water molecules in this system. In addition to (i) water molecules reorienting as water molecules in bulk, at low hydration levels the disruption of the hydrogen-bond network results in: (ii) water molecules that have a significantly slower reorientation time than bulk-like water molecules, and (iii) water molecules that are present in very sparse regions of the system, where only a few hydrogen-bond partners are present. These latter water molecules are only partly hydrogen bonded and exhibit very fast reorientation in a restricted direction (leaving their one or two existing hydrogen bonds intact). By changing the hydration level through variation of the relative humidity from very low (RH \sim 0%) to relatively high (RH \sim 93%), we observe how an increasing fraction of water molecules acquires

bulk-like character. We also find that a temperature increase results in the conversion from slow water to bulk-like water behavior. The identification and characterization of water molecules that are slow and water molecules with very fast dynamics could have great implications for the properties of transport of material through membranes and for the functioning of transmembrane proteins. Specifically, since it has been demonstrated that reorientation of water is a key factor in the transfer of protons (see Chapters 7 and 8), the proton mobility around membranes is expected to be strongly affected.

BIBLIOGRAPHY

- [1] N. Agmon. The Grotthuss mechanism. *Chem. Phys. Lett.*, 244:456–462, 1995.
- [2] N. Agmon, D. Huppert, A. Masad, and E. Pines. Excited-state proton-transfer to methanol water mixtures. *J. Phys. Chem.*, 95:10407–10413, 1991.
- [3] N. Agmon, E. Pines, and D. Huppert. Geminate recombination in proton-transfer reactions. 2. Comparison of diffusional and kinetic schemes. *J. Chem. Phys.*, 88:5631–5638, 1988.
- [4] C. Akilan, N. Rohman, R. Buchner, and G. Hefter. Temperature effects on ion association and hydration in MgSO_4 by dielectric spectroscopy. *Chem. Phys. Chem.*, 7:2319–2330, 2006.
- [5] L. Almasy, A. Len, N.K. Szekely, and J. Plestil. Solute aggregation in dilute aqueous solutions of tetramethylurea. *J. Fluid Phase Equilib.*, 257:114–119, 2007.
- [6] B. Bagchi. Water dynamics in the hydration layer around proteins and micelles. *Chem. Rev.*, 105:3197–3219, 2005.
- [7] H.J. Bakker and H.-K. Nienhuys. Delocalization of protons in liquid water. *Science*, 297:587–590, 2002.
- [8] A.A. Bakulin, C. Liang, T. la Cour Jansen, D.A. Wiersma, H.J. Bakker, and M.S. Pshenichnikov. Hydrophobic solvation: A 2D IR spectroscopic inquest. *Acc. Chem. Res.*, 42:1229–1238, 2009.
- [9] P. Ball. Water as an active constituent in cell biology. *Chem. Rev.*, 108:74–108, 2008.
- [10] R. Balu, H. Zhang, E. Zukowski, J.Y. Chen, A.G. Markelz, and S.K. Gregurick. Terahertz spectroscopy of bacteriorhodopsin and rhodopsin: Similarities and differences. *Biophys. J.*, 94:3217–3226, 2008.
- [11] E. Bardez, B.T. Goguillon, E. Keh, and B. Valeur. Dynamics of excited-state reactions in reversed micelles. 1. Proton transfer involving a hydrophilic fluorescent probe. *J. Phys. Chem.*, 88:1909–1913, 1984.
- [12] E. Bardez, E. Monnier, and B. Valeur. Dynamics of excited-state reactions in reversed micelles. 2. Proton transfer involving various fluorescent probes according to their sites of solubilization. *J. Phys. Chem.*, 89:5031–5036, 1985.

- [13] J. Barthel, K. Bachhuber, R. Buchner, H. Hetzenauer, and M. Kleebauer. A computer-controlled system of transmission-lines for the determination of the complex permittivity of lossy liquids between 8.5 GHz and 90 GHz. *Ber. Bunsenges. Physik. Chem.*, 95:853–859, 1991.
- [14] J. Barthel, R. Buchner, C.G. Hözl, and M. Munsterer. Dynamics of benzonitrile, propylene carbonate and butylene carbonate: The influence of molecular shape and flexibility on the dielectric relaxation behaviour of dipolar aprotic liquids. *Z. Phys. Chem. (München)*, 214:1213–1231, 2000.
- [15] J. Barthel, R. Buchner, and B. Wurm. The dynamics of liquid formamide, N-methylformamide, N,N-dimethylformamide, and N,N-dimethylacetamide. A dielectric relaxation study. *J. Mol. Liq.*, 98-99:51–69, 2002.
- [16] J.D. Bernal and R.H. Fowler. A theory of water and ionic solution, with particular reference to hydrogen and hydroxyl ions. *J. Chem. Phys.*, 1:515–548, 1933.
- [17] H. Bianchi, H.R. Corti, and R. Fernández-Prini. The conductivity of dilute aqueous-solutions of magnesium-chloride at 25 °C. *J. Sol. Chem.*, 17:1059–1065, 1988.
- [18] W. Blokzijl and J.B.F.N. Engberts. Hydrophobic effects - opinions and facts. *Angew. Chem., Intl. Ed. Engl.*, 32:1545–1579, 1993.
- [19] C.J.F.B. Böttcher. *Theory of Electrical Polarization Vol. I*. Elsevier (Amsterdam), 1973.
- [20] C.J.F.B. Böttcher and R. Bordewijk. *Theory of Electrical Polarization Vol. II*. Elsevier (Amsterdam), 1978.
- [21] R.W. Boyd. *Nonlinear Optics*. Academic Press, 2003.
- [22] C.L. Braun and S.N. Smirnov. Why is water blue. *J. Chem. Edu.*, 70:612–615, 1993.
- [23] R. Buchner, J. Barthel, and J. Stauber. The dielectric relaxation of water between 0 °C and 35 °C. *Chem. Phys. Lett.*, 306:57–63, 1999.
- [24] R. Buchner, S.G. Capewell, G. Hefter, and P.M. May. Ion-pair and solvent relaxation processes in aqueous Na₂SO₄ solutions. *J. Phys. Chem. B*, 103:1185–1192, 1999.
- [25] R. Buchner, T. Chen, and G. Hefter. Complexity in "simple" electrolyte solutions: Ion pairing in MgSO₄(aq). *J. Phys. Chem. B*, 108:2365–2375, 2004.
- [26] R. Buchner, G. Hefter, and P.M. May. Dielectric relaxation of aqueous NaCl solutions. *J. Phys. Chem. A*, 103:1–9, 1999.

-
- [27] R. Buchner, C. Hölzl, J. Stauber, and J. Barthel. Dielectric spectroscopy of ion-pairing and hydration in aqueous tetra-N-alkylammonium halide solutions. *Phys. Chem. Chem. Phys.*, 4:2169–2179, 2002.
- [28] H. Bursing, S. Kundu, and P. Vöhringer. Solvation dynamics at aqueous lipid-membrane interfaces explored by temperature-dependent 3-pulse-echo peak shifts: Influence of the lipid polymorphism. *J. Phys. Chem. B*, 107:2404–2413, 2003.
- [29] C.D. Cappa, J.D. Smith, B.M. Messer, R.C. Cohen, and R.J. Saykally. Effects of cations on the hydrogen bond network of liquid water: New results from X-ray absorption spectroscopy of liquid microjets. *J. Phys. Chem. B*, 110:5301–5309, 2006.
- [30] G. Caracciolo, D. Pozzi, and R. Caminiti. Hydration effect on the structure of dioleoylphosphatidylcholine bilayers. *Appl. Phys. Lett.*, 90:183901, 2007.
- [31] D. Chandler. Interfaces and the driving force of hydrophobic assembly. *Nature*, 437:640–647, 2005.
- [32] A. Chandra, M.E. Tuckerman, and D. Marx. Connecting solvation shell structure to proton transport kinetics in hydrogen-bonded networks via population correlation functions. *Phys. Rev. Lett.*, 99:145901, 2007.
- [33] M. Chaplin. Anomalous properties of water, April 2010. [Internet URL] <http://www1.lsbu.ac.uk/water/anmlies.html>. Retrieved on 20 July 2010.
- [34] T. Chen, G. Heftner, and R. Buchner. Dielectric spectroscopy of aqueous solutions of KCl and CsCl. *J. Phys. Chem. A*, 107:4025–4031, 2003.
- [35] B. Cohen, D. Huppert, K.M. Solntsev, Y. Tsfadia, E. Nachliel, and M. Gutman. Excited state proton transfer in reverse micelles. *J. Am. Chem. Soc.*, 124:7539–7547, 2002.
- [36] K.D. Collins, G.W. Neilson, and J.E. Enderby. Ions in water: Characterizing the forces that control chemical processes and biological structure. *Biophys. Chem.*, 128:95–104, 2007.
- [37] S. Corcelli and J. Skinner. Infrared and raman line shapes of dilute HOD in liquid H₂O and D₂O from 10 to 90 °C. *J. Phys. Chem. A*, 109:6154–6165, 2005.
- [38] M.J. Cox and H.J. Bakker. Parallel proton transfer pathways in aqueous acid-base reactions. *J. Chem. Phys.*, 128:174501, 2008.
- [39] J.C. Deak, S.T. Rhea, L.K. Iwaki, and D.D. Dlott. Vibrational energy relaxation and spectral diffusion in water and deuterated water. *J. Phys. Chem. A*, 104:4866–4875, 2000.

- [40] A.M. Dokter, S. Woutersen, and H.J. Bakker. Inhomogeneous dynamics in confined water nanodroplets. *Proc. Natl. Acad. Soc. USA*, 103:15355–15358, 2006.
- [41] S. Ebbinghaus, S.J. Kim, M. Heyden, X. Yu, U. Heugen, M. Gruebele, D.M. Leitner, and M. Havenith. An extended dynamical hydration shell around proteins. *Proc. Natl. Acad. Soc. USA*, 104:20749–20752, 2007.
- [42] R.J. Ellis and A.P. Minton. Join the crowd. *Nature*, 425:27–28, 2003.
- [43] C.J. Fecko, J.J. Loparo, S.T. Roberts, and A. Tokmakoff. Local hydrogen bonding dynamics and collective reorganization in water: Ultrafast infrared spectroscopy of HOD/D₂O. *J. Chem. Phys.*, 122:054506, 2005.
- [44] H.S. Frank and M.W. Evans. Free volume and entropy in condensed systems III. Entropy in binary liquid mixtures; Partial molal entropy in dilute solutions; Structure and thermodynamics in aqueous electrolytes. *J. Chem. Phys.*, 13:507–532, 1945.
- [45] F. Franks, editor. *Water: A Comprehensive Treatise*, volume 3. Plenum, London, 1973.
- [46] T. Fukasawa, T. Sato, J. Watanabe, Y. Hama, W. Kunz, and R. Buchner. Relation between dielectric and low-frequency raman spectra of hydrogen-bond liquids. *Phys. Rev. Lett.*, 95:197802, 2005.
- [47] K. Fumino, K. Yukiyasu, A. Shimizu, and Y. Taniguchi. NMR studies on dynamic behavior of water molecules in tetraalkylammonium bromide-D₂O solutions at 5–25 °C. *J. Mol. Liq.*, 75:1–12, 1998.
- [48] S.H. Glarum. Dielectric relaxation of polar liquids. *J. Chem. Phys.*, 33:1371–1375, 1960.
- [49] G. Graziano and B. Lee. On the intactness of hydrogen bonds around nonpolar solutes dissolved in water. *J. Phys. Chem. B*, 109:8103–8107, 2005.
- [50] D.J. Griffiths. *Introduction to Electrodynamics*. Pearson Education, 1999.
- [51] P. Hakizimana, M. Masureel, B. Gbaguidi, J.M. Ruyschaert, and C. Govaerts. Interactions between phosphatidylethanolamine headgroup and LmrP, a multidrug transporter. *J. Biol. Chem.*, 283:9369–9376, 2008.
- [52] K. Hallenga, J.R. Grigera, and H.J.C. Berendsen. Influence of hydrophobic solutes on the dynamic behavior of water. *J. Phys. Chem.*, 84:2381–2390, 1980.
- [53] J.B. Hasted, D.M. Ritson, and C.H. Collie. Dielectric properties of aqueous ionic solutions. parts I and II. *J. Chem. Phys.*, 16:1–21, 1948.

-
- [54] Y. Hayashi, Y. Katsumoto, S. Omori, N. Kishii, and A. Yasuda. Liquid structure of the urea-water system studied by dielectric spectroscopy. *J. Phys. Chem. B*, 111:1076–1080, 2007.
- [55] Y. He, P.I. Ku, J.R. Knab, J.Y. Chen, and A. Markelz. Protein dynamical transition does not require protein structure. *Phys. Rev. Lett.*, 101:178103, 2008.
- [56] U. Heugen, G. Schwaab, E. Brundermann, M. Heyden, X. Yu, D.M. Leitner, and M. Havenith. Solute-induced retardation of water dynamics probed directly by terahertz spectroscopy. *Proc. Natl. Acad. Soc. USA*, 103:12301–12306, 2006.
- [57] F. Hofmeister. Zur Lehre von der Wirkung der Salze. *Arch. Exp. Pathol. Pharmacol.*, 24:247–260, 1888.
- [58] K. Hristova and S.H. White. Determination of the hydrocarbon core structure of fluid dioleoylphosphocholine (DOPC) bilayers by X-ray diffraction using specific bromination of the double-bonds: Effect of hydration. *Biophys. J.*, 74:2419–2433, 1998.
- [59] C.-J. Hsieh and W.-G. Wu. Structure and dynamics of primary hydration shell of phosphatidylcholine bilayers at subzero temperatures. *Biophys. J.*, 71:3278–3287, 1996.
- [60] J.B. Hubbard, L. Onsager, W.M. van Beek, and M. Mandel. Kinetic polarization deficiency in electrolyte solutions. *Proc. Natl. Acad. Soc. USA*, 74:401–404, 1977.
- [61] J. Hunger. PhD thesis, University of Regensburg, 2010.
- [62] J. T. Hynes, T.-H. Tran-Thi, and G. Granucci. Intermolecular photochemical proton transfer in solution: New insights and perspectives. *J. Photochem. Photobiol. A*, 154:3–11, 2002.
- [63] Y. Ishihara, S. Okouchi, and H. Uedaira. Dynamics of hydration of alcohols and diols in aqueous solution. *J. Chem. Soc. Faraday Trans.*, 93:3337–3342, 1997.
- [64] G.L. Jendrasiak and R.L. Smith. The interaction of water with the phospholipid head group and its relationship to the lipid electrical conductivity. *Chem. Phys. Lipids*, 131:183–195, 2004.
- [65] P. Jungwirth and D.J. Tobias. Specific ion effects at the air/water interface. *Chem. Rev.*, 106:1259–1281, 2006.
- [66] U. Kaatze. The dielectric properties of water in its different states of interaction. *J. Sol. Chem.*, 26:1049–1112, 1997.

- [67] U. Kaatzte and A. Rupprecht. Hydrophobic hydration and concentration fluctuations in aqueous solutions of urea derivatives. Evidence from dielectric and ultrasonic spectrometry. *J. Chem. Phys.*, 117:4936–4939, 2002.
- [68] J.T. Kindt and C.A. Schmuttenmaer. Far-infrared dielectric properties of polar liquids probed by femtosecond terahertz pulse spectroscopy. *J. Phys. Chem.*, 100:10373–10379, 1996.
- [69] T. Kinugasa, A. Kondo, S. Nishimura, Y. Miyauchi, Y. Nishii, K. Watanabe, and H. Takeuchi. Estimation for size of reverse micelles formed by AOT and SDEHP based on viscosity measurement. *Colloid Surface A*, 204:193–199, 2002.
- [70] B. Klösgen, C. Reichle, S. Kohlsmann, and K.D. Kramer. Dielectric spectroscopy as a sensor of membrane headgroup mobility and hydration. *Biophys. J.*, 71:3251–3260, 1996.
- [71] J. Knab, J.Y. Chen, and A. Markelz. Hydration dependence of conformational dielectric relaxation of lysozyme. *Biophys. J.*, 90:2576–2581, 2006.
- [72] E. Knoesel, M. Bonn, J. Shan, F. Wang, and T.F. Heinz. Conductivity of solvated electrons in hexane investigated with terahertz time-domain spectroscopy. *J. Chem. Phys.*, 121:394–404, 2004.
- [73] M. Koeberg, C.-C. Wu, D. Kim, and M. Bonn. THz dielectric relaxation of ionic liquid:water mixtures. *Chem. Phys. Lett.*, 439:60–64, 2007.
- [74] S. Koneshan, J.C. Rasaiah, R.M. Lynden-Bell, and S.H. Lee. Solvent structure, dynamics, and ion mobility in aqueous solutions at 25 °C. *J. Phys. Chem. B*, 102:4193–4204, 1998.
- [75] M.F. Kropman, H.K. Nienhuys, S. Woutersen, and H.J. Bakker. Vibrational relaxation and hydrogen-bond dynamics of HDO:H₂O. *J. Phys. Chem. A*, 105:4622–4626, 2001.
- [76] N. Kucerka, J.F. Nagle, J.N. Sachs, S.E. Feller, J. Pencer, A. Jackson, and J. Katsaras. Lipid bilayer structure determined by the simultaneous analysis of neutron and X-ray scattering data. *Biophys. J.*, 95:2356–2367, 2008.
- [77] W. Kunz. Specific ion effects in colloidal and biological systems. *Curr. Opin. Colloid Interface*, 15:34–39, 2010.
- [78] W. Kunz, J. Henle, and B.W. Ninham. 'Zur Lehre von der Wirkung der Salze' (about the science of the effect of salts): Franz Hofmeister's historical papers. *Curr. Opin. Colloid Interface*, 9:19–37, 2004.
- [79] M. Kurylowicz. Gigahertz spectroscopy on hydrated polyunsaturated phospholipid membranes. Master's thesis, University of British Columbia, Vancouver, 2003.

-
- [80] D. Laage and J.T. Hynes. Do more strongly hydrogen-bonded water molecules reorient more slowly? *Chem. Phys. Lett.*, 433:80–85, 2006.
- [81] D. Laage and J.T. Hynes. A molecular jump mechanism of water reorientation. *Science*, 311:832–835, 2006.
- [82] D. Laage and J.T. Hynes. Reorientational dynamics of water molecules in anionic hydration shells. *Proc. Natl. Acad. Soc. USA*, 104:11167–11172, 2007.
- [83] D. Laage and J.T. Hynes. On the molecular mechanism of water reorientation. *J. Phys. Chem. B*, 112:14230–14242, 2008.
- [84] D. Laage, G. Stirnemann, and J.T. Hynes. Why water reorientation slows without iceberg formation around hydrophobic solutes. *J. Phys. Chem. B*, 113:2428–2435, 2009.
- [85] E.W. Lang and H.-D. Lüdemann. Pressure and temperature dependence of the longitudinal proton relaxation times in supercooled water to minus 87 °C and 2500 bar. *J. Chem. Phys.*, 67:718–723, 1977.
- [86] H. Lapid, N. Agmon, M.K. Petersen, and G.A. Voth. A bond-order analysis of the mechanism for hydrated proton mobility in liquid water. *J. Chem. Phys.*, 122:014506, 2005.
- [87] C.P. Lawrence and J.L. Skinner. Vibrational spectroscopy of HOD in liquid D₂O. VII. Temperature and frequency dependence of the OH stretch lifetime. *J. Chem. Phys.*, 119:3840–3848, 2003.
- [88] A.G. Lee. How lipids affect the activities of integral membrane. *Biochim. Biophys. Acta*, 1666:62–87, 2004.
- [89] P. Leiderman, L. Genosar, and D. Huppert. Excited-state proton transfer: Indication of three steps in the dissociation and recombination process. *J. Phys. Chem. A*, 109:5965–5977, 2005.
- [90] N.E. Levinger. Water in confinement. *Science*, 298:1722–1723, 2002.
- [91] A.S. Lileev, D.V. Loginova, and A.K. Lyashenko. Dielectric properties of aqueous hydrochloric acid solutions. *Mendeleev Commun.*, 17:364–365, 2007.
- [92] Y.A. Lin, B.M. Auer, and J.L. Skinner. Water structure, dynamics, and vibrational spectroscopy in sodium bromide solutions. *J. Chem. Phys.*, 131:144511, 2009.
- [93] J. Lindner, P. Vöhringer, M.S. Pshenichnikov, D. Cringus, D.A. Wiersma, and M. Mostovoy. Vibrational relaxation of pure liquid water. *Chem. Phys. Lett.*, 421:329–333, 2006.

- [94] E.R. Lippincott and R. Schröder. One dimensional model of the hydrogen bond. *J. Chem. Phys.*, 23:1099–1106, 1955.
- [95] A.J. Lock and H.J. Bakker. Temperature dependence of vibrational relaxation in liquid H₂O. *J. Chem. Phys.*, 117:1708–1713, 2002.
- [96] A.J. Lock, S. Woutersen, and H.J. Bakker. Ultrafast energy equilibration in hydrogen-bonded liquids. *J. Phys. Chem. A*, 105:1238–1243, 2001.
- [97] R. Ludwig, F. Weinhold, and T.C. Farrar. Experimental and theoretical determination of the temperature-dependence of deuteron and oxygen quadrupole coupling-constants of liquid water. *J. Chem. Phys.*, 103:6941–6950, 1995.
- [98] P.L. Luisi and B.E. Straub, editors. *Reverse Micelles: Biological and Technological Relevance of Amphiphilic Structures in Apolar Media*. Plenum (New York), 1984.
- [99] R.L. Mancera. Computer simulation of the effect of salt on the hydrophobic effect. *J. Chem. Soc. Faraday Trans.*, 94:3549–3559, 1998.
- [100] R. Mancinelli, A. Botti, F. Bruni, M.A. Ricci, and A.K. Soper. Hydration of sodium, potassium, and chloride ions in solution and the concept of structure maker/breaker. *J. Phys. Chem. B*, 111:13570–13577, 2007.
- [101] Y. Marcus. Effect of ions on the structure of water: Structure making and breaking. *Chem. Rev.*, 109:1346–1370, 2009.
- [102] O. Markovitch and N. Agmon. Structure and energetics of the hydronium hydration shells. *J. Phys. Chem. A*, 111:2253–2256, 2007.
- [103] O. Markovitch, H. Chen, S. Izvekov, F. Paesani, G.A. Voth, and N. Agmon. Special pair dance and partner selection: Elementary steps in proton transport in liquid water. *J. Phys. Chem. B*, 112:9456–9466, 2008.
- [104] D. Marx, M. Tuckerman, J. Hutter, and M. Parrinello. The nature of the hydrated excess proton in water. *Nature*, 397:601–604, 1999.
- [105] J. Mittal and G. Hummer. Static and dynamic correlations in water at hydrophobic interfaces. *Proc. Natl. Acad. Soc. USA*, 105:20130–20135, 2008.
- [106] M. Miyazaki, A. Fujii, T. Ebata, and N. Mikami. Infrared spectroscopic evidence for protonated water clusters forming nanoscale cages. *Science*, 304:1134–1137, 2004.
- [107] K. Mizuse, A. Fujii, and N. Mikami. Long range influence of an excess proton on the architecture of the hydrogen bond network in large-sized water clusters. *J. Chem. Phys.*, 126:231101, 2007.

-
- [108] O. Mohammed, A. Pines, J. Dreyer, E. Pines, and E.T.J. Nibbering. Solvent-dependent photoacidity state of pyranine monitored by transient mid-infrared spectroscopy. *Chem. Phys. Chem.*, 6:625–636, 2005.
- [109] D.E. Moilanen, E.E. Fenn, Y. Lin, J.L. Skinner, B. Bagchi, and M.D. Fayer. Water inertial reorientation: Hydrogen bond strength and the angular potential. *Proc. Natl. Acad. Soc. USA*, 105:5295–5300, 2008.
- [110] D.E. Moilanen, N.E. Levinger, D. B. Spry, and M.D. Fayer. Confinement or the nature of the interface? Dynamics of nanoscopic water. *J. Am. Chem. Soc.*, 129:14311–14318, 2007.
- [111] D.E. Moilanen, D.B. Spry, and M.D. Fayer. Water dynamics and proton transfer in nafion fuel cell membranes. *Langmuir*, 24:3690–3698, 2008.
- [112] D.E. Moilanen, D. Wong, D.E. Rosenfeld, E.E. Fenn, and M.D. Fayer. Ion-water hydrogen-bond switching observed with 2D IR vibrational echo chemical exchange spectroscopy. *Proc. Natl. Acad. Soc. USA*, 106:375–380, 2009.
- [113] S. Mukamel. *Principles of nonlinear optical spectroscopy*. Oxford University Press, 1995.
- [114] N. Nandi, K. Bhattacharyya, and B. Bagchi. Dielectric relaxation and solvation dynamics of water in complex chemical and biological systems. *Chem. Rev.*, 100:2013–2045, 2000.
- [115] A. Nitzan and J. Jortner. Vibrational relaxation of a molecule in a dense medium. *Mol. Phys.*, 25:713–734, 1973.
- [116] A. Novak. Hydrogen bonding in solids. correlation of spectroscopic and crystallographic data. *Struct. Bond.*, 18:177–216, 1974.
- [117] H. Ohtaki and T. Radnai. Structure and dynamics of hydrated ions. *Chem. Rev.*, 93:1157–1204, 1993.
- [118] C. Okpala, A. Guiseppi-Elie, and D.M. Maharajh. Several properties of 1,1,3,3-tetramethylurea-water systems. *J. Chem. Eng. Data*, 25:384–386, 1980.
- [119] A.W. Omta, A.M. Kropman, S. Woutersen, and H.J. Bakker. Negligible effect of ions on the hydrogen-bond structure in liquid water. *Science*, 301:347–349, 2003.
- [120] D. Pant and N.E. Levinger. Polar solvation dynamics in nonionic reverse micelles and model polymer solutions. *Langmuir*, 16:10123–10130, 2000.
- [121] S. Park and M.D. Fayer. Hydrogen bond dynamics in aqueous NaBr solutions. *Proc. Natl. Acad. Soc. USA*, 104:16731–16738, 2007.

- [122] C. Petersen, K.-J. Tielrooij, and H.J. Bakker. Strong temperature dependence of water reorientation in hydrophobic hydration shells. *J. Chem. Phys.*, 130:214511, 2009.
- [123] L. Piatkowski, K.B. Eisenthal, and H.J. Bakker. Ultrafast intermolecular energy transfer in heavy water. *Phys. Chem. Chem. Phys.*, 11:9033–9038, 2009.
- [124] J.L. Pickl. PhD thesis, University of Regensburg, 1998.
- [125] I.R. Piletic, D.E. Moilanen, D.B. Spry, N.E. Levinger, and M.D. Fayer. Testing the core/shell model of nanoconfined water in reverse micelles using linear and nonlinear IR spectroscopy. *J. Phys. Chem. A*, 110:4985–4999, 2006.
- [126] E. Pines and D. Huppert. Geminate recombination proton-transfer reactions. *Chem. Phys. Lett.*, 126:88–91, 1986.
- [127] E. Pines and D. Huppert. Observation of geminate recombination in excited state proton transfer. *J. Chem. Phys.*, 84:3576–3577, 1986.
- [128] E. Pines, D. Huppert, and N. Agmon. Geminate recombination in excited-state proton-transfer reactions: Numerical solution of the Debye–Smoluchowski equation with backreaction and comparison with experimental results. *J. Chem. Phys.*, 88:5620–5630, 1988.
- [129] E. Pines, D. Huppert, and N. Agmon. Salt effects on steady-state quantum yields of ultrafast, diffusion-influenced, reversible photoacid dissociation reactions. *J. Phys. Chem.*, 95:666–674, 1991.
- [130] M.J. Politi, O. Brandt, and J.H. Fendler. Ground-and excited-state proton transfers in reversed micelles. Polarity restrictions and isotope effects. *J. Phys. Chem.*, 89:2345–2354, 1985.
- [131] M.J. Politi and H.J. Chaimovich. Water activity in reversed sodium bis (2-ethylhexyl) sulfosuccinate micelles. *J. Phys. Chem.*, 90:282–287, 1986.
- [132] M.J. Politi and J.H. Fendler. Laser pH-jump initiated proton transfer on charged micellar surfaces. *J. Am. Chem. Soc.*, 106:265–273, 1984.
- [133] J. Qvist and B. Halle. Thermal signature of hydrophobic hydration dynamics. *J. Am. Chem. Soc.*, 130:10345–10353, 2008.
- [134] Y.L.A. Rezus and H.J. Bakker. On the orientational relaxation of HDO in liquid water. *J. Chem. Phys.*, 123:114502, 2005.
- [135] Y.L.A. Rezus and H.J. Bakker. Observation of immobilized water molecules around hydrophobic groups. *Phys. Rev. Lett.*, 99:148301, 2007.
- [136] Y.L.A. Rezus and H.J. Bakker. Strong slowing down of water reorientation in mixtures of water and tetramethylurea. *J. Phys. Chem. A*, 112:2355–2361, 2008.

-
- [137] M. Rini, B.-Z. Magnes, E. Pines, and E.T.J. Nibbering. Real-time observation of bimodal proton transfer in acid-base pairs in water. *Science*, 301:349–352, 2003.
- [138] C. Rønne, P.O. Astrand, and S.R. Keiding. THz spectroscopy of liquid H₂O and D₂O. *Phys. Rev. Lett.*, 82:2888–2891, 1999.
- [139] C. Rønne and S.R. Keiding. Low frequency spectroscopy of liquid water using THz-time domain spectroscopy. *J. Mol. Liq.*, 101:199–218, 2002.
- [140] C. Rønne, L. Thrane, P.O. Astrand, A. Wallqvist, K.V. Mikkelsen, and S.R. Keiding. Investigation of the temperature dependence of dielectric relaxation in liquid water by THz reflection spectroscopy and molecular dynamics simulation. *J. Chem. Phys.*, 107:5319–5331, 1997.
- [141] L. Rosso and I.R. Gould. Structure and dynamics of phospholipid bilayers using recently developed general all-atom force fields. *J. Comput. Chem.*, 29:24–37, 2008.
- [142] D. Russo, G. Hura, and T. Head-Gordon. Hydration dynamics near a model protein surface. *Biophys. J.*, 86:1852–1862, 2004.
- [143] S. Schrödle, G. Hefter, W. Kunz, and R. Buchner. Effects of nonionic surfactant C12E5 on the cooperative dynamics of water. *Langmuir*, 22:924–932, 2006.
- [144] J.Q. Searcy and J.B. Fenn. Clustering of water on hydrated protons in a supersonic free jet expansion. *J. Chem. Phys.*, 61:5282–5288, 1974.
- [145] A. Shimizu, K. Fumino, K. Yukiyasu, and Y. Taniguchi. NMR studies on dynamic behavior of water molecule in aqueous denaturant solutions at 25 °C: Effects of guanidine hydrochloride, urea and alkylated ureas. *J. Mol. Liq.*, 85:269–278, 2000.
- [146] J.-W. Shin, N.I. Hammer, E.G. Diken, M.A. Johnson, R.S. Walters, T.D. Jaeger, M.A. Duncan, R.A. Christie, and K.D. Jordan. Infrared signature of structures associated with the H⁺(H₂O)_n (n=6 to 27) clusters. *Science*, 304:1137–1140, 2004.
- [147] P.L. Silvestrelli. Are there immobilized water molecules around hydrophobic groups? Aqueous solvation of methanol from first principles. *J. Phys. Chem. B*, 113:10728–10731, 2009.
- [148] B.J. Siwick and H.J. Bakker. On the role of water in intermolecular proton-transfer reactions. *J. Am. Chem. Soc.*, 129:13412–13420, 2007.
- [149] M. Smiechowski and J. Stangret. Proton hydration in aqueous solution: Fourier transform infrared studies of HDO spectra. *J. Chem. Phys.*, 125:204508, 2006.

- [150] J.D. Smith, R.J. Saykally, and P.L. Geissler. The effects of dissolved halide anions on hydrogen bonding in liquid water. *J. Am. Chem. Soc.*, 129:13847–13856, 2007.
- [151] K.M. Solntsev, D. Huppert, N. Agmon, and L.M. Tolbert. Photochemistry of "super" photoacids. 2. Excited-state proton transfer in methanol/water mixtures. *J. Phys. Chem. A*, 104:4658–4669, 2000.
- [152] A.K. Soper and J.L. Finney. Hydration of methanol in aqueous solution. *Phys. Rev. Lett.*, 71:4346–4349, 1993.
- [153] N.T. Southall, K.A. Dill, and A.D.J. Haymet. A view of the hydrophobic effect. *J. Phys. Chem. B*, 106:521–533, 2002.
- [154] D.B. Spry and M.D. Fayer. Charge redistribution and photoacidity: Neutral versus cationic photoacids. *J. Chem. Phys.*, 128:084508, 2008.
- [155] D.B. Spry, A. Goun, and M.D. Fayer. Deprotonation dynamics and stokes shift of pyranine (HPTS). *J. Phys. Chem. A*, 111:230–237, 2007.
- [156] D.B. Spry, A. Goun, K. Glusac, D.E. Moilanen, and M.D. Fayer. Proton transport and the water environment in nafion fuel cell membranes and AOT reverse micelles. *J. Am. Chem. Soc.*, 111:8122–8130, 2007.
- [157] T. Steinel, J.B. Asbury, J. Zheng, and M.D. Fayer. Watching hydrogen bonds break: A transient absorption study of water. *J. Phys. Chem. A*, 108:10957–10964, 2004.
- [158] G. Stirnemann, J.T. Hynes, and D. Laage. Water hydrogen bond dynamics in aqueous solutions of amphiphiles. *J. Phys. Chem. B*, 114:3052–3059, 2010.
- [159] L. Stryer. *Biochemistry*. W.H. Freeman, 1981.
- [160] J.M.J. Swanson, C.M. Maupin, H.N. Chen, M.K. Petersen, J.C. Xu, Y.J. Wu, and G.A. Voth. *J. Phys. Chem. B*, 111:4300–4314, 2007.
- [161] H.S. Tan, I.R. Piletic, and M.D. Fayer. Orientational dynamics of water confined on a nanometer length scale in reverse micelles. *J. Chem. Phys.*, 122:174501, 2005.
- [162] K.J. Tielrooij, N. Garcia-Araez, M. Bonn, and H.J. Bakker. Cooperativity in ion hydration. *Science*, 328:1006–1009, 2010.
- [163] K.J. Tielrooij, D. Paparo, L. Piatkowski, H.J. Bakker, and M. Bonn. Dielectric relaxation dynamics of water in model membranes probed by terahertz spectroscopy. *Biophys. J.*, 97:2484–2492, 2010.
- [164] K.J. Tielrooij, C. Petersen, Y.L.A. Rezus, and H.J. Bakker. Reorientation of HDO in liquid H₂O at different temperatures: Comparison of first and second order correlation functions. *Chem. Phys. Lett.*, 471:71–74, 2009.

-
- [165] K.J. Tielrooij, R.L.A. Timmer, H.J. Bakker, and M. Bonn. Structure dynamics of the proton in liquid water probed with terahertz time-domain spectroscopy. *Phys. Rev. Lett.*, 102:198303, 2009.
- [166] D.J. Tobias and J.C. Hemminger. Chemistry - getting specific about specific ion effects. *Science*, 319:1197, 2008.
- [167] T.-H. Tran-Thi, C. Gustavsson, C. Prayer, S. Pommeret, and J.T. Hynes. Primary ultrafast events preceding the photoinduced proton transfer from pyranine to water. *Chem. Phys. Lett.*, 329:421–430, 2000.
- [168] M. Tuckerman, K. Laasonen, M. Sprik, and M. Parrinello. Ab-initio molecular-dynamics simulation of the solvation and transport of H_3O^+ and OH^- ions in water. *J. Phys. Chem.*, 99:5749–5752, 1995.
- [169] D.A. Turton, J. Hunger, G. Hefter, R. Buchner, and K. Wynne. Glasslike behavior in aqueous electrolyte solutions. *J. Chem. Phys.*, 128:161102, 2008.
- [170] P. Van Rysselberghe and J.M. McGee. The conductance of aqueous solutions of magnesium perchlorate. *J. Am. Chem. Soc.*, 65:737–738, 1943.
- [171] M. Vasilescu, A. Caragheorgheopol, M. Almgren, W. Brown, J. Alsins, and R. Johannsson. Structure and dynamics of nonionic polyoxyethylene reverse micelles by time-resolved fluorescence quenching. *Langmuir*, 11:2893–2898, 1995.
- [172] D.S. Venables, K. Huang, and C.A. Schmuttenmaer. Effect of reverse micelle size on the librational band of confined water and methanol. *J. Phys. Chem. B*, 105:9132–9138, 2001.
- [173] V.V. Volkov, D.J. Palmer, and R. Righini. Distinct water species confined at the interface of a phospholipid membrane. *Phys. Rev. Lett.*, 99:078302, 2007.
- [174] V.V. Volkov, D.J. Palmer, and R. Righini. Heterogeneity of water at the phospholipid membrane interface. *J. Phys. Chem. B*, 111:1377–1383, 2007.
- [175] W. Wachter, S. Fernandez, R. Buchner, and G. Hefter. Ion association and hydration in aqueous solutions of LiCl and Li_2SO_4 by dielectric spectroscopy. *J. Phys. Chem. B*, 111:9010–9017, 2007.
- [176] W. Wachter, W. Kunz, R. Buchner, and G. Hefter. Is there an anionic Hofmeister effect on water dynamics? Dielectric spectroscopy of aqueous solutions of NaBr , NaI , NaNO_3 , NaClO_4 , and NaSCN . *J. Phys. Chem. A*, 109:8675–8683, 2005.
- [177] A. Wallqvist and B.J. Berne. Effective potentials for liquid water using polarizable and nonpolarizable models. *J. Phys. Chem.*, 97:13841–13851, 1993.

- [178] S.R. Wassall. Pulsed field-gradient-spin echo NMR studies of water diffusion in a phospholipid model membrane. *Biophys. J.*, 71:2724–2732, 1996.
- [179] H. Wei, Y. Fan, and Y.Q. Gao. Effects of urea, tetramethyl urea, and trimethylamine N-oxide on aqueous solution structure and solvation of protein backbones: A molecular dynamics simulation study. *J. Phys. Chem. B*, 114:557–568, 2010.
- [180] A. Weller. Fast reactions of excited molecules. *Progr. React. Kinet.*, 1:189–233, 1961.
- [181] M.C. Wiener and S.H. White. Structure of a fluid dioleoylphosphatidylcholine bilayer determined by joint refinement of X-ray and neutron-diffraction data. *Biophys. J.*, 61:434–447, 1992.
- [182] K. Winkler, J. Lindner, H. Bursing, and P. Vöhringer. Ultrafast Raman-induced Kerr-effect of water: Single molecule versus collective motions. *J. Chem. Phys.*, 113:4674–4682, 2000.
- [183] S. Woutersen and H.J. Bakker. Resonant intermolecular transfer of vibrational energy in liquid water. *Nature*, 402:507–509, 1999.
- [184] S. Woutersen and H.J. Bakker. Ultrafast vibrational and structural dynamics of the proton in liquid water. *Phys. Rev. Lett.*, 96:138305, 2006.
- [185] S. Woutersen, U. Emmerichs, H.-K. Nienhuys, and H.J. Bakker. Anomalous temperature dependence of vibrational lifetimes in water and ice. *Phys. Rev. Lett.*, 81:1106–1109, 1998.
- [186] H. Yada, M. Nagai, and K. Tanaka. Origin of the fast relaxation component of water and heavy water revealed by terahertz time-domain attenuated total reflection spectroscopy. *Chem. Phys. Lett.*, 464:166–170, 2008.
- [187] K. Yoshida, K. Ibuki, and M. Ueno. Pressure and temperature effect on ^2H spin-lattice relaxation times and ^1H chemical shifts in tert-butyl alcohol- and urea D_2O solutions. *J. Chem. Phys.*, 108:1360–1367, 1998.
- [188] B.L. Yu, Y. Yang, F. Zeng, X. Xin, and R.R. Alfano. Reorientation of the H_2O cage studied by terahertz time-domain spectroscopy. *Appl. Phys. Lett.*, 86:061912, 2005.
- [189] A.A. Zavitsas. Properties of water solutions of electrolytes and nonelectrolytes. *J. Phys. Chem. B*, 105:7805–7817, 2001.
- [190] T.A. Zawodzinski, M. Neeman, L.O. Sillerud, and S. Gottesfeld. Determination of water diffusion-coefficients in perfluorosulfonate ionomeric membranes. *J. Phys. Chem.*, 95:6040–6044, 1991.

-
- [191] W. Zhao, D.E. Moilanen, E.E. Fenn, and M.D. Fayer. Water at the surfaces of aligned phospholipid multibilayer model membranes probed with ultrafast vibrational spectroscopy. *J. Am. Chem. Soc.*, 130:13927–13937, 2008.
- [192] M. Zulauf and H.-F. Eicke. Inverted micelles and microemulsions in the ternary system water/aerosol-OT/isooctane as studied by photon correlation spectroscopy. *J. Phys. Chem.*, 83:480–486, 1979.

APPENDIX: *When Scimon met Valery*

This story is based on fictional characters. Any resemblance with actual persons is purely coincidental^a.

Once upon a time, somewhere in the capricious forests that separated Scienceland and Societyland, two people that had never met before were walking around. 'Hi, I'm Valery, from Societyland. Who are you? Are you lost?' said Valery. 'My name is Scimon from Scienceland and yes, it does appear that I am a bit lost.' Although both were far away from home, they were pleasantly surprised by the accidental encounter and decided to take the opportunity to get to know more about each other and their respective lands.

Valery asked what a typical day at work looked like for Scimon and listened with great interest to stories about ultrafast lasers, tweaking mirrors and lenses of optical setups; about measuring optical properties of systems; about using mathematical algorithms to analyze measurement results and relating these to the physics and chemistry of the systems studied; and about scientific publications and conference presentations. Valery summarized: 'So basically, your daily work is to develop tools to generate knowledge - the setup and the analysis software - and to obtain knowledge of the systems studied, which you then communicate.' 'Exactly! Although I must admit that all this rarely happens in the course of one day...' Scimon sulked.

Valery had occasionally seen newspapers that discussed what was going on in Scienceland, but wondered if Societyland and Scienceland could somehow benefit more from each other, in addition to the knowledge that was being communicated from Scienceland. 'The main thing you develop in Scienceland is knowledge, which is an intangible product. But these setups that you develop, they are tangible. Could they be useful in Societyland?' After this question, Scimon thought for a while and answered that it could be possible that the setups or parts of them would be useful in Societyland, but that it takes a lot of effort to develop and build them and that the applications are probably limited. 'That means that the development and production costs are high and the market potential is small,' Valery concluded somewhat disappointed.

'Then what about the software that you use for analysis or modeling? Can this be used by people in my land?' Valery asked. 'That is in fact quite a good idea, especially because it is much easier to reproduce software than technical setups. So very low production costs, as you would say,' replied Scimon. They then discussed different ways in which people in both lands would benefit. The software could, for instance, be sold to Societyland and/or people from Sci-

^aGeschreven in het kader van het "FOM Valorisatiehoofdstuk".

enceland could be paid for providing software support. This would create more resources for Scienceland to do more science, creating mutual benefit. Valery then pointed out an important point: 'Software that analyzes or models a process or system is a knowledge-based product or "knowledge with a wrapping". People in Societyland often need such wrappings to appreciate the value of knowledge.'

Valery decided to try and find a possible wrapping for the knowledge that resulted from Scimon's studies. In order to do so, it was first necessary to connect the knowledge from Scienceland to benefits in Societyland. With Valery listening carefully, Scimon explained his results on reorienting water molecules, proton transport and the influence of charges and hydrophobic groups on water dynamics. After sitting down for a while, Valery and Scimon drew up what they called the S-TEA bridge.

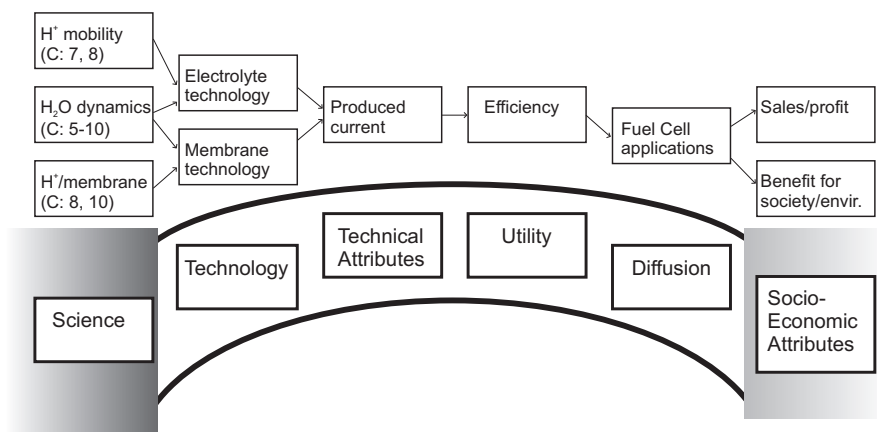


FIGURE A. 1. The Science-Technology Economic Analysis (S-TEA) bridge that links Scienceland (left) to Societyland (right).

'This analysis shows,' said Valery 'that your results are connected to fuel cell applications, which have a very large market potential in Societyland.' 'Then I should start producing fuel cells!' Scimon said somewhat naively. 'Not necessarily. But you should definitely protect the ideas that you have about improved fuel cell systems.' 'Why should I protect this knowledge? If I don't share knowledge, how can people benefit from it?' Valery explained: 'Tangible products have a clear owner, but for intangible products you need to claim ownership. So I am not saying that you should not share your knowledge - I am saying that you should protect your ideas! For instance, in the case of your analysis and modeling software, this knowledge-based intangible product is automatically protected by copyright law. This means that *you* can distribute the software, but others are not allowed to copy it.'

Scimon wanted to know other ways of protecting knowledge, besides copyright protection. Valery summarized: 'First of all, you can publish your results,

by which you claim ownership. This is also called "defensive publishing", because by publishing you make sure that nobody else can claim your knowledge. Secondly, at the other extreme, you can keep your knowledge as a trade secret, like the Coca Cola recipe. Then, thirdly, there are legal systems that can be used to protect your knowledge. The copyright system is one, and another system is the patent system. They both apply only to certain types of knowledge.'

'I don't think I want to create any trade secrets, but this patent system sounds interesting. What is it for?' 'The idea behind the patent system, is to reward inventors for coming up with new ideas and sharing it. The reward is given in the form of a patent, which gives the owner the right to exclude others from making, using or selling the claimed invention in a commercial way.' Scimon commented: 'That actually sounds fair. If I invest resources in developing ideas, I should get some compensation. So with the patent I obtain complete ownership and I can do with the invention as I want?' Valery replied: 'Well, it is a bit more tricky. First of all, patents are only valid in the country where you apply for one. Secondly, if your invention depends on another invention for which someone else owns a patent, you can not use or sell your invention without infringing the patent of that other person, unless that person permits you to do so, i.e. by licensing it to you.'

'Then why would I want to obtain a patent? They are also expensive, right?' Valery explained that the right of using an invention, which is regulated through the patent, can be licensed out, for instance to people in Societyland, who might use it to produce and sell a product. 'These people could buy the entire patent, obtain an exclusive license agreement or a non-exclusive one. Also cross-licenses exist, where people give each other the right to use their respective inventions. As you see, patents are a currency for knowledge and they can be exchanged for other currencies. Through a patent you can benefit from the license agreements; the people that license it from you can produce a product and sell it, so they benefit; and people in Societyland can use the new products. This way everybody in Scienceland and Societyland benefits!'

They returned to the topic of ideas for improved fuel cell systems. 'Do you think I could obtain a patent?' Scimon asked. 'You can not patent material properties, but you can patent a process, machine, article of manufacture, a composition of matter and an improvement of any of these. So, yes, in principle you can patent a system with properties that are useful for fuel cell applications. There are however additional requirements that you need to meet: novelty, non-obviousness, utility and full disclosure. This means that there should be no prior art that already covers your invention; it should be non-obvious for a person skilled in the art; it should have some application; and it should be fully disclosed. This full disclosure means that you should describe in detail how the invention works. As a reward for sharing this knowledge you can obtain the patent.'

To check if the system that Scimon had in mind did not exist yet, they did the prior art search *t1l/(fuel cell\$ and proton\$)* on the website of the United States Patent and Trademark Office (USPTO). This search gave 91 results on Sept. 21st 2010, to which they compared Scimon's idea. They also studied the

results to learn in which direction most of the research was done and which companies were most actively patenting. These companies could be potential licensees or interesting for cooperations.

Valery: 'Now if you want to apply for a patent, it is extremely important that you do not share your knowledge *before* you have filed the patent! After the filing date, you can freely share it, for instance by publishing in a scientific journal. So secrecy is very important, but only in the beginning. Keep in mind that the aim of a patent is to reward you for sharing your knowledge. This is also the reason why patent applications are published, which usually happens eighteen months after the filing date.'

Scimon wondered: 'Then how do I apply for a patent? How does this work in Societyland?' 'The "game of patenting" is played in three arenas: the administrative arena, the legal arena and the business arena. The game starts in the administrative arena. Here you write your patent application and send it to a patent office, where it will be judged. If your patent is granted, you pay (annually increasing) renewal fees to the patent office. It can usually be renewed for a maximum of twenty years after filing date.' said Valery. 'Aha, so if my invention would take more than twenty years of development before it can be produced, the patent will expire before it can be used!' Scimon noted. 'Indeed if the time to market is too long, a patent is not advisable.'

They then talked about the legal arena. Valery explained that that is where, for instance, infringements of patents are discussed. 'If you do not have the resources or the will to defend your patent in court, the patent is not worth anything. Owning a patent also means that you need to actively monitor if nobody is infringing your patent. Often lawsuits about patent infringement result in settlements that involve licensing agreements. Sometimes, however, large fines are to be paid or patents are declared invalid. This is why for you it is probably a good idea to work together with someone from Societyland or to sell your patent to someone who has the financial and human resources to defend it.'

Scimon asked what happens in the business arena. 'The business arena is where you use your patent in a commercial way, for instance to obtain licensing agreements. Or where you sell your patent to someone in Societyland that has the expertise to commercialize your invention. But in fact, you can also use patents as a marketing tool in the business arena: If you show that you have a number of patents, you might obtain additional research funding in Scienceland, because patents are believed to be an indicator for innovativity. Furthermore, it can be helpful if you would like to start your own science-based company, for instance to develop and produce fuel cells. This is because venture capital firms prefer to invest in patent-protected technology.'

Scimon sighed. It was getting late and although Scimon enjoyed the enlightening discussion with Valery, understanding Societyland was still difficult. They decided to return to their respective lands, but agreed to meet each other regularly in between Scienceland and Societyland, in order to learn from each other and help each other. Scimon and Valery met each other more and more often and - of course - they lived happily ever after...

SUMMARY

Aqueous systems and spectroscopy

Water plays an important role in our everyday lives, which we experience for instance when we drink, cook, clean, wash, etc. Its importance is also evident on a microscopic level: almost all biological processes occur in aqueous environments. Therefore investigating the interactions between different solutes and the water solvent is highly relevant.

In this thesis, we have studied *(i)* neat water, and aqueous systems containing three different solutes: *(ii)* ions, *(iii)* protons and *(iv)* amphiphiles. We study the reorientation dynamics of the water molecules in these systems. To this end we have used terahertz time-domain spectroscopy and femtosecond infrared pump-probe spectroscopy. Both measurement techniques are very well suited for studying the ultrafast dynamics in aqueous systems and they are sensitive to the same water reorientation process. Since they probe water reorientation in a different way, these techniques have complimentary advantages.

In terahertz (THz) time-domain spectroscopy, a THz pulse with a duration of ~ 3 ps is created and focused into the sample under investigation. In aqueous systems, the main process that is active at low THz frequencies (< 1 THz) is dielectric relaxation. This is the effect that water molecules are unable to keep up reorienting with an oscillating electric field, when the driving frequency becomes too high. For bulk water, this results in an absorption peak at 20 GHz, corresponding to a reorientation time scale of 8 ps. Terahertz dielectric relaxation measurements were used to determine the fraction of water molecules that are affected by the presence of a solute and as a result no longer participate in the reorientation process, thus leading to a smaller relaxation strength of the 20 GHz peak. This technique also provides information on the fraction of water molecules that is affected by the movement of charged solutes.

In the femtosecond infrared (fs-IR) pump-probe measurements, we used a linearly polarized infrared pump pulse with a duration of ~ 150 fs to resonantly excite the OD-stretch vibration of a subset of HDO molecules in H_2O . With a probe pulse that followed after a variable delay, we monitored these vibrationally excited molecules. This was done for pump and probe pulse mutually parallel and perpendicular. Since the pump pulse excites an anisotropic distribution, the probe signal with parallel polarization is larger than for perpendicular polarization. However, after reorientation of the water molecules, the distribution of excited molecules is isotropic and the parallel and

perpendicular signals are equal. Hence, by examining the difference between the two signals as a function of pump-probe delay, we obtained the reorientation dynamics of the water molecules.

(i) Neat water: the effect of temperature

We have studied the temperature dependence of the molecular reorientation of HDO molecules in H₂O with fs-IR spectroscopy. This resulted in the second order microscopic reorientation time, which changes from 4.8 ± 0.3 ps at 1 °C to 0.97 ± 0.05 ps at 70 °C. These measurements were compared with literature results of THz time-domain spectroscopy, where the first order macroscopic reorientation time is obtained. From this comparison, we extracted the ratio between the macroscopic first order reorientation time and the second order microscopic reorientation time. It turned out that this ratio does not depend on temperature, confirming that the same reorientation process is probed, using the two different techniques.

(ii) Ions: semi-rigid hydration and cooperativity

We have studied the effect of ions on the dynamics of water molecules using fs-IR and THz spectroscopy. These techniques are sensitive to the dynamics of different vectors of the water molecule: the dipole vector (THz) and the transition dipole moment (fs-IR). The measurement of these two different molecular vectors revealed that ions with a weakly hydrated counterion are surrounded by a semi-rigid hydration shell. Cations are surrounded by a semi-rigid hydration shell, where water molecules move in a propeller-like fashion with the two hydrogen atoms acting as the rotor blades. In the case of anions, one hydrogen atom points towards the ion and the other hydrogen atom forms the blade of the propeller. Surprisingly, if strongly hydrated cations and anions are combined (as in a MgSO₄ solution), the effect of the ions on water is strongly interdependent and non-additive, and extends well beyond the first solvation shell of water molecules directly surrounding the ion.

(iii) Protons: mobility and the role of water reorientation

The high mobility of protons in water is usually attributed to the Grotthuss mechanism, where the interconversion of covalent bonds and hydrogen bonds leads to highly efficient charge transport with limited mass transport. So far, this process was mainly investigated theoretically. We have used THz dielectric relaxation measurements to study the properties of the proton in water. These measurements showed that a small fraction of water molecules no longer participates in the reorientation process, corresponding to ~ 4 water molecules per proton, i.e. the Eigen complex $[\text{H}_9\text{O}_4]^+$. We furthermore found that the equivalent of ~ 15 water molecules was affected by the moving proton charge. This means that the proton mobility involves a large number of reorienting water molecules.

To assess the connection between proton transfer and the ability of the surrounding water molecules to reorient, we studied proton transfer in water nanopools, in which water reorientation is known to be slower. In this pump-probe experiment, we used a visible pump pulse to electronically excite a photoacid, which is a molecule that becomes highly acidic upon electronic excitation. With the probe pulse (either in the infrared or in the visible regime) that followed after a variable delay, we monitored the dynamics of different modes (either electronic or vibrational) that correspond to the photoacid with or without the proton. This allowed us to follow the dynamics of proton transfer. This experiment was performed for solvated photoacids in reverse micelles with diameters between ~ 1.6 and ~ 5.5 nm. The measurements showed that the proton transfer slows down upon decreasing the diameter of the micelle. This result confirms that water reorientation forms the limiting factor for proton mobility.

(iv) Amphiphiles: effects of hydration level and temperature

In biology, the interaction between hydrophobic groups and water plays a crucial role, for instance for the functioning of proteins. We have studied the reorientation dynamics of water molecules around tetrametyurea (TMU), a molecule with four hydrophobic (methyl) groups. This was done for different hydration levels, i.e. TMU concentrations. We performed dielectric relaxation spectroscopy in the GHz^b and THz range and compared the results with existing fs-IR measurements of aqueous TMU solutions. We found the reorientation dynamics of water molecules in the hydration shell of TMU to be between 3 and 10 times slower than the dynamics of bulk water, depending on the concentration of TMU in water. The data were in good agreement with previous fs-IR measurements, and indicated that the effect of hydrophobic groups on water is strong but relatively short-ranged. We also found that with increasing temperature, the fraction of water contained in the hydrophobic hydration shell decreases, which implies that the overall effect of hydrophobic groups on water becomes smaller.

Finally, we have examined the dynamics of water reorientation in hydrated model membranes, consisting of stacked layers of DOPC lipid bilayers^c. By controlling the number of water molecules per lipid molecule in the system, we studied the interplay between the model membrane and water molecules and its effect on the water dynamics. For decreasing hydration levels, we observed that the collective bulk-like dynamics becomes less pronounced, and that there is an increase of both very slowly reorienting and very rapidly reorienting water molecules. Temperature-dependent measurements revealed the interconversion between these three types of water.

^bThe GHz measurements were conducted in the group of prof. R. Buchner at the University of Regensburg (Germany) using electronically created and detected guided waves.

^cDOPC = 1,2-Dioleoyl-sn-Glycero-3-Phosphocholine

SAMENVATTING

Water is de meest voorkomende stof op onze planeet en speelt een zeer belangrijke rol in ons dagelijks leven. Ook op moleculair niveau is water onlosmakelijk verbonden met leven: de belangrijkste biologische processen vinden plaats in waterige oplossingen. Water komt echter zelden voor in pure vorm, maar vooral als zeewater en in het cytoplasma van cellen, waar zich per honderd watermoleculen enkele ionen of macromoleculen (bijvoorbeeld eiwitten) bevinden. Begrip van de interactie tussen water en opgeloste stoffen is belangrijk voor de vele processen die zich afspelen in water. Daarom hebben we in dit proefschrift onderzocht hoe de beweeglijkheid van water op moleculair niveau wordt beïnvloed door de aanwezigheid van bepaalde stoffen, met name ionen, protonen en hydrofobe moleculaire groepen. Hierbij hebben we gebruikgemaakt van twee ultrasnelle lasertechnieken, waarmee we specifiek naar de draaibeweging van de watermoleculen kunnen kijken.

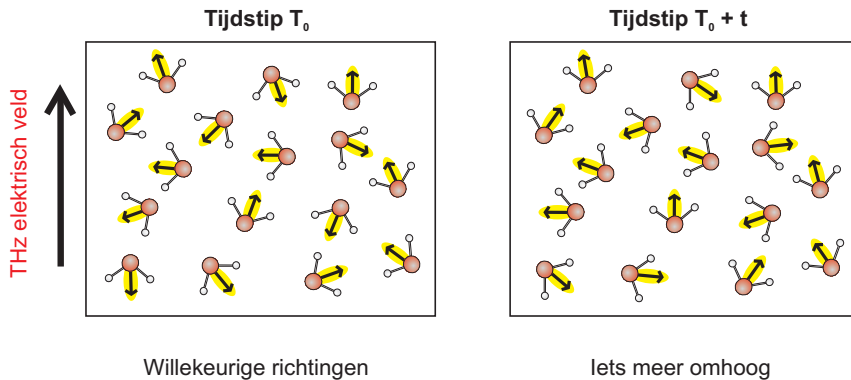
Draaiend water

Water bestaat uit een netwerk van watermoleculen dat met waterstofbruggen bijeen wordt gehouden. Door het verbreken en het opnieuw vormen van waterstofbruggen kunnen watermoleculen draaien. Bij kamertemperatuur reoriënteert een watermolecuul in bulk water met een tijdschaal van een picoseconde (1 ps is 10^{-12} s, oftewel een miljoenste van een miljoenste van een seconde). De watermoleculen in vloeibaar water zijn dus bijzonder beweeglijk. De snelheid waarmee een watermolecuul kan draaien wordt bepaald door de directe omgeving van het watermolecuul. Zodoende kan het bestuderen van deze dynamica in verschillende waterige oplossingen ons iets leren over de interactie tussen watermoleculen en de hierin opgeloste stoffen.

Aangezien watermoleculen zo bijzonder snel draaien, zijn speciale technieken nodig om deze bewegingen te kunnen volgen. Deze technieken zijn gebaseerd op lasers, die zeer korte pulsen (van ongeveer 100 fs oftewel 0.1 ps) genereren. In dit proefschrift zijn de volgende twee meettechnieken gebruikt: fasegevoelige terahertz spectroscopie (THz) en femtoseconde polarisatiegevoelige infrarood pomp-probe spectroscopie (fs-IR). Deze technieken zijn allebei gevoelig voor de reoriëntatie van watermoleculen en kunnen beide gebruikt worden om te bepalen hoeveel watermoleculen normale dynamica en hoeveel moleculen langzamere of snellere dynamica vertonen. Eerst wordt in deze samenvatting uitgelegd hoe deze technieken werken; daarna worden vier resultaten (*i-iv*), die in detail beschreven zijn in dit proefschrift, uitgelegd.

Het meten van reoriëntatie met THz spectroscopie

Een watermolecuul bestaat uit een negatief geladen zuurstofatoom O en twee positief geladen waterstofatomen H. Omdat het watermolecuul H–O–H een knik heeft (zie de watermoleculen in Fig. 1) ligt het centrum van de positieve ladingen niet op het centrum van de negatieve lading: het molecuul heeft een dipoolmoment (de pijltjes in Fig. 1). Dit betekent dat watermoleculen zich zullen richten naar een extern aangebracht elektrisch veld. Dit is schematisch weergegeven in Fig. 1, waar het linkerplaatje een aantal watermoleculen weergeeft op het moment dat er net een elektrisch veld is aangebracht. Op dat moment hebben de moleculen nog een willekeurige oriëntatie. Na een tijd t hebben de watermoleculen zich een beetje gericht naar het elektrische veld. In onze terahertzmetingen, is het elektrische veld een lichtpuls met frequentiecomponenten in het terahertzgebied (1 THz is 10^{12} Hz) en meten we hoeveel van dit ver-infrarode licht wordt geabsorbeerd in de wateroplossingen die we bestuderen. Als er minder absorptie is in een bepaalde oplossing dan in bulk water, betekent dit dat sommige watermoleculen zich niet goed kunnen reoriënteren.

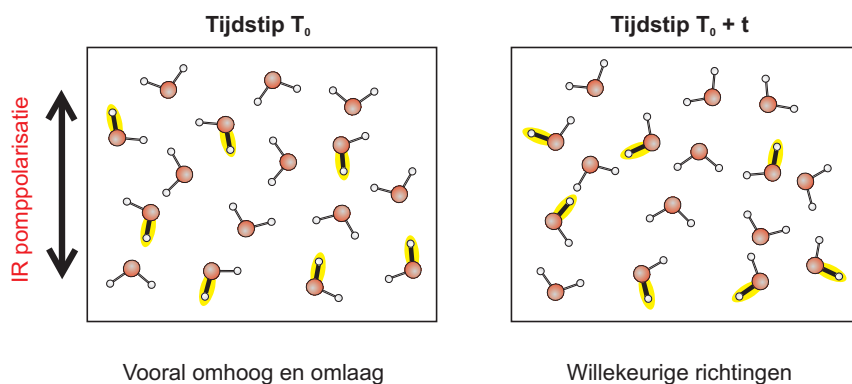


FIGUUR 1. *Terahertzspectroscopie*. Door het aanbrengen van een elektrisch veld op tijdstip T_0 oriënteren de watermoleculen (zuurstofatoom O is rood en waterstofatoom H is wit) zich dusdanig dat de dipoolassen (de zwarte pijltjes) iets meer meewijzen met het elektrische veld, zoals te zien is in het rechterplaatje.

Het meten van reoriëntatie met fs-IR spectroscopie

Bij de infraroodmetingen bepalen we niet hoeveel licht er geabsorbeerd wordt van één lichtpuls, maar gebruiken we twee lichtpulsen. Deze lichtpulsen hebben een duur van minder dan 0.2 ps en hebben een frequentie in het infraroodgebied. Het licht in deze pulsen heeft de juiste golflengte om watermoleculen aan het trillen te brengen. Deze trilling is de strekvibratie van één van de OH-groepen van een watermolecuul. Wij gebruiken pomp-probe

spectroscopie, waarbij de eerste puls, de pomppuls, watermoleculen aan het trillen brengt en de tweede puls, de probepuls, de watermoleculen meet die nog aan het trillen zijn. De tijd tussen deze twee pulsen kan met hele kleine stapjes gevarieerd worden. We meten het signaal voor een polarisatie (de trillingsrichting van het elektrische veld van de infraroodpulsen) van de probe parallel aan de pomppolarisatie en voor een polarisatie loodrecht op de pomppolarisatie. De pomppuls brengt vooral watermoleculen aan het trillen, waarvan de OH-groep wijst in de richting van de polarisatie van de pomppuls (linkerplaatje in Fig. 2). Daardoor zijn in die richting meer watermoleculen aan het trillen, zodat het signaal voor parallelle probepolarisatie groter is dan voor loodrechte polarisatie. Echter door het draaien van de watermoleculen zullen er uiteindelijk evenveel watermoleculen trillen in alle richtingen en worden de signalen voor parallelle en loodrechte polarisatie evengroot (rechterplaatje in Fig. 2). Het verschil tussen het parallelle en het loodrechte signaal vervalt dus van een bepaalde waarde op tijdstip T_0 naar nul. De snelheid waarmee dit verschilsignaal vervalt geeft dus aan hoe snel de watermoleculen draaien.

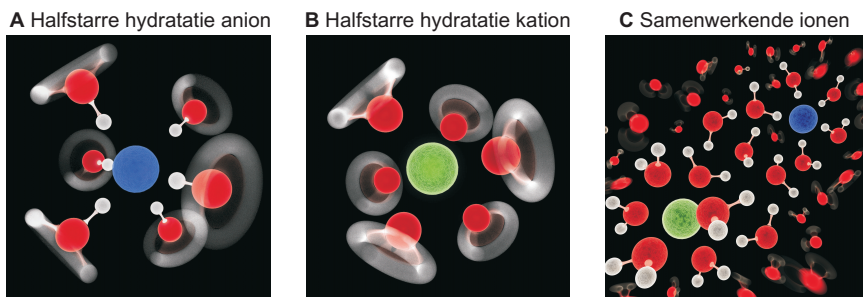


FIGUUR 2. *Infraroodspectroscopie*. Op tijdstip T_0 worden enkele OH-groepen van watermoleculen aan het trillen gebracht door een infraroodpuls met een bepaalde polarisatie (de pomppuls). Op dit moment zijn er meer OH-groepen aan het trillen in de verticale richting dan in andere richtingen. Naar verloop van tijd (op tijdstip $T_0 + t$) reoriënteren de watermoleculen zich, en zijn er evenveel trillende OH-groepen zowel in de verticale als in de horizontale richting. Door het meten van de hoeveelheid trillende OH-groepen in beide richtingen (met de probepuls) kan dus de reoriëntatietijd van de watermoleculen bepaald worden.

(i) Waterdynamica

De eerste metingen zijn gedaan aan zuiver water, dus zonder opgeloste stoffen. Wij hebben voor verschillende temperaturen tussen 1 en 70 °C met femtoseconde infraroodspectroscopie gemeten hoe snel waterreoriëntatie plaatsvindt. Het blijkt dat water sneller draait bij hogere temperaturen. Dit

komt doordat bij hogere temperaturen, watermoleculen gemiddeld minder waterstofbruggen vormen en zodoende makkelijker kunnen reoriënteren. Wij hebben onze meetresultaten vergeleken met THz metingen uit de literatuur en concluderen dat de tijdschaal die we meten met fs-IR spectroscopie hetzelfde is – op een constante factor na – als de tijdschaal die gemeten wordt met THz spectroscopie. Deze factor, waarvan de herkomst bekend is, is niet afhankelijk van de temperatuur.



FIGUUR 3. *Waterdynamica rondom ionen.* (A) Grafische weergave van de propellorachtige beweging van watermoleculen rondom een negatief geladen ion: van elk watermolecuul wijst één OH-groep naar het ion, terwijl de andere OH-groep vrij kan bewegen. Dit wordt veroorzaakt door een waterstofbrug tussen het ion en het waterstofatoom van de OH-groep die naar het ion wijst. (B) Grafische weergave van de propellorachtige beweging van watermoleculen rondom een positief geladen ion: nu vormen de twee OH-groepen de twee rotorbladen van de propellor en wijst de dipoolas weg van het ion. Dit komt doordat deze watermoleculen hun dipoolas mee laten wijzen met het elektrische veld rondom de ionen. (C) Grafische weergave van het effect van sterk gehydrateerde ionen op de waterdynamica, waarbij grote, geheel starre structuren worden gevormd tussen de ionen. Illustraties gemaakt door XKP.

(ii) Waterdynamica rondom ionen

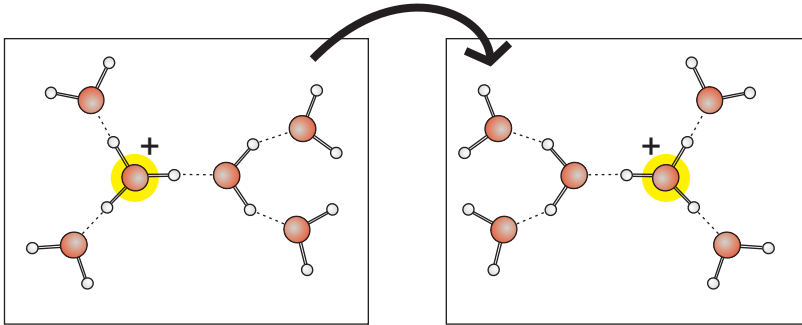
Als een zout, bijvoorbeeld keukenzout (NaCl), wordt opgelost in water, splitst het zich in geladen ionen (voor keukenzout: Na^+ en Cl^-). Het effect van deze geladen ionen op de structuur en dynamica van het omringende water is van belang in o.a. biologische systemen. Zo is bekend, dat de oplosbaarheid van eiwitten afhangt van de ionen die zich in de oplossing bevinden. Het effect van ionen op waterdynamica hebben wij onderzocht met THz en fs-IR metingen. Wij hebben gevonden dat ionen vooral een effect hebben op de dynamica van de watermoleculen die zich direct om het ion heen bevinden. Dit effect is echter anders voor positieve dan voor negatieve ionen, zoals geïllustreerd in Fig. 3A en B. De watermoleculen rondom de ionen voeren een propellorbeweging uit: watermoleculen naast een negatief ion (anion) hebben één OH-groep die star is en naar het ion wijst en één OH-groep die ronddraait als rotorblad van de propellor; bij watermoleculen naast een positief ion (kation) fungeren beide OH-groepen als rotorbladen. Ionen worden dus omgeven door een 'halfstarre

hydratieschil', waar de dynamica van een bepaalde as van de watermoleculen langzaam is, terwijl de andere as vrij kan bewegen. Dit hebben wij kunnen vaststellen, doordat de twee gebruikte meettechnieken elk de dynamica van een andere as volgen: THz spectroscopie de dynamica van de dipoolas en fs-IR spectroscopie de dynamica van OH-groepen.

In bepaalde gevallen, bijvoorbeeld voor MgSO_4 , gebeurt er iets verassends. Het ion Mg^{2+} en het ion SO_4^{2-} hebben allebei een sterk effect op de dynamica van de omringende watermoleculen. Als deze ionen worden gecombineerd, werken de ionen samen om een groter aantal watermoleculen te beïnvloeden en wordt de dynamica van de watermoleculen in het geheel langzamer. In dit geval is de hydratieschil dus geheel star. Er ontstaan dan grote, geheel starre structuren van watermoleculen tussen de ionen van tegengestelde lading, zoals te zien in Fig. 3C. Hierbij kunnen tot wel achttien watermoleculen bij betrokken zijn per opgelost MgSO_4 zoutmolecuul. Dit laat zien dat het effect van ionen op de dynamica van watermoleculen, in sommige gevallen, niet-additief is en verder kan reiken dan de eerste schil van watermoleculen direct rondom een ion.

(iii) Waterdynamica rondom protonen

De overdracht van protonen (H^+) vormt de basis van de generatie en opslag van energie in levende organismen, en ligt ten grondslag aan de werking van brandstofcellen. Daarnaast is bekend dat de mobiliteit van protonen in vloeibaar water vele malen hoger is dan de mobiliteit van andere positief geladen deeltjes, zoals natriumionen. Wij hebben met THz en fs-IR metingen gekeken, welke rol de dynamica van water speelt bij de overdracht van protonen. Het blijkt dat een proton een complex vormt met een hydroniumion (H_3O^+) met daaromheen drie watermoleculen waarvan de dipoolassen wegwijzen van het positief geladen hydroniumion. De dipoolassen van deze watermoleculen vertonen langzame dynamica, net als in het geval van kationen, zoals hierboven beschreven. Bij protonoverdracht verandert een covalente binding van een OH-groep in een waterstofbrug, terwijl de waterstofbrug tussen het H-atoom van deze OH-groep en een zuurstofatoom van een aangrenzend watermolecuul in een covalente binding wordt omgezet. Deze omzetting van een covalente binding in een waterstofbrug en vice versa leidt tot een verplaatsing van de positieve lading. Dit proces is geïllustreerd in Fig. 4. Uit de metingen volgt dat een groot aantal watermoleculen, ongeveer vijftien moleculen, zich moeten reorganiseren om het transport van het proton mogelijk te maken. De reoriëntatiedynamica van watermoleculen speelt dus een cruciale rol bij protonoverdracht. Dit hebben wij verder bevestigd door protonoverdracht te meten in nanodruppeltjes water (in "reverse micelles"), waarvan bekend is dat de waterdynamica langzamer is. Voor deze systemen hebben wij inderdaad gevonden dat protonoverdracht langzamer wordt.



FIGUUR 4. *Protonoverdracht en waterdynamica*. Bij protonoverdracht wordt een covalente binding (dubbele lijn tussen waterstofatoom en zuurstofatoom) omgewisseld met een waterstofbrug (gestreepte lijn), zodat de lading verplaatst naar het aangrenzende watermolecuul. Bij dit proces vindt vooral ladingsverplaatsing plaats i.p.v. massaverplaatsing, zodat het zeer efficiënt is. Het is echter wel noodzakelijk dat vele watermoleculen rondom de lading zich reorganiseren, zodat protonoverdracht wordt gefaciliteerd.

(iv) Waterdynamica rondom hydrofoben

In de biologie heeft water vaak interactie met moleculen die deels hydrofoob zijn en deels hydrofiel. Een voorbeeld hiervan zijn lipidemoleculen, die een hydrofiële kop en een hydrofobe staart hebben. Deze moleculen kunnen zodoende een dubbellaag rondom het water in een cel vormen: het celmembraan. De interactie tussen water en hydrofobe groepen speelt verder een belangrijke rol bij het vouwen en dus het functioneren van eiwitten, die allerlei belangrijke processen reguleren. Wij hebben onderzocht hoe water zich gedraagt, wanneer het zich naast hydrofobe groepen bevindt. Het blijkt dat een aantal watermoleculen in dit geval veel langzamere reoriëntatie heeft. Dit komt waarschijnlijk doordat het netwerk van watermoleculen, die met elkaar verbonden zijn via waterstofbruggen, zich om hydrofobe groepen heenvouwt, zodat de dynamica van bepaalde watermoleculen lokaal gefrustreerd is. Dit wordt bevestigd door de waarneming, dat er bij het verhogen van de temperatuur minder watermoleculen met langzamere dynamica zijn. Bij een hogere temperatuur zijn er gemiddeld minder waterstofbruggen en is het dus makkelijker voor het waternetwerk om zich om de hydrofobe groepen heen te vouwen, zonder frustratie van de dynamica. Dit hebben we waargenomen zowel voor wateroplossingen van kleine moleculen met hydrofobe groepen als voor dubbele lagen van gehydrateerde lipidemoleculen.

DANKWOORD/ACKNOWLEDGEMENTS

Geachte lezer, hartelijk dank voor het openen van dit proefschrift en het nemen van de tijd om het te lezen – of in ieder geval dit gedeelte!

Bij de totstandkoming van dit proefschrift zijn twee mensen in het bijzonder onmisbaar geweest, namelijk mijn begeleiders Huib en Mischa. Ik heb ontzettend veel van jullie geleerd, op wetenschappelijk gebied en ook zeker daarbuiten. Daarnaast was de samenwerking ook heel plezierig, dankzij jullie gevoel voor humor en gezonde relativiseringsvermogen. Ik heb vanaf dag één veel vrijheid en daarmee vertrouwen gekregen, maar kon altijd bij jullie langskomen voor advies. Huib, ik heb zeer genoten van je scherpe en creatieve kijk op meetresultaten en onze discussies over de interpretatie hiervan (menigmaal ook op vrijdagavond). Mischa, je hebt een bijzonder goede neus voor interessante onderzoeksrichtingen en weet altijd op een constructieve manier de sterktes en zwaktes aan te wijzen van een meting, analyse, artikel of presentatie. Ik ben verder blij dat jullie met mij de proef zijn aangegaan van een promovendus die "gedelocaliseerd" is over twee onderzoeksgroepen – dit is goed uitpakkt vooral doordat jullie samen een goed team vormen. Kortom, ik ben zeer dankbaar dat ik in allebei jullie onderzoeksgroepen en met jullie heb mogen werken en wens jullie alle succes in de toekomst.

I would like to thank prof. Richard Buchner at the University of Regensburg (Germany) for his hospitality and the nice and successful collaboration that we had. Thanks for making it possible for me to perform measurements in your laboratory that has such a rich history in the field of dielectric relaxation spectroscopy.

I also would like to thank prof. Noam Agmon from the Hebrew University in Jerusalem (Israel) for his critical reading of the manuscript and his constructive comments, questions and suggestions. Thanks also for the great conference at the Sea of Galilee and the nice historical and cultural activities that were organized around the conference.

Het leven van een promovendus gaat niet altijd over rozen – er zijn altijd apparaten die kapot gaan, meetresultaten die in eerste instantie onbegrijpelijk zijn of die later artefacten blijken. Hier staat echter tegenover dat het altijd veel leuker is als iets lukt, wanneer dat eerst niet lukte. Daarnaast sta je er als promovendus nooit alleen voor en kun je altijd bij je lotgenoten terecht voor steun. De afgelopen vier jaar heb ik heel veel fijne collega's om me heen gehad, waarvan ik er een aantal in het bijzonder wil bedanken – overigens in een volgorde, die in willekeurige mate willekeurig is.

Rutger, tijdens de nachtelijke meeturen van het 'zure zult'-project was er gelukkig altijd jouw droge humor. Verder was het altijd nuttig om met je te discussiëren over natuurkunde of het analyseren van data – bedankt ook voor je softwarematige nalatenschap aan de groep. Jocelyn, thanks for teaching me some tricks in the lab (such as actually putting the chopper *in* the beam path) and for the chats that were not necessarily science-related. Lukasz, thanks for all the fun and for helping me out after my little snowboarding accident at the winter school in Switzerland; good luck with finishing your thesis! A big thanks to my Terahertz buddies Joep and Ronald for the constructive way in which we shared the setup and our THz experiences and for the great West Coast road trip. Domenico, thanks for our nice collaboration on the 'hydrated lipid bilayers' project and for your camera work in Romania. Johannes, thanks for making me feel very welcome in Regensburg, for helping me out in the lab there and later for joining us in Amsterdam and continuing some of my work. Ellen, bedankt voor al het proeflezen en voor de samenwerking op het illustere IR-THz project – ooit gaat het werken. Thanks to the seniors in the Bakker and Bonn groups that were always willing to share their knowledge and experiences, in particular Yves, Euan, Han-Kwang and Christian Petersen. Hincó, je bent van grote waarde voor de groep en dankzij jouw mooie shaker kon ik mijn THz metingen mooi calibreren; bedankt ook voor het mooie boottripje op de Kaag! Henk Dekker, bedankt voor de hulp bij problemen van elektronische aard. Then there were the nice people with whom I shared offices: Adriaan, Pavol, Ellen, Katrin and Wing-Kiu and those who accompanied me on conferences: Joep and Ronald (US), Lukasz (Switzerland), Maria (US) and Ymkje (Russia). Finally, I would like to acknowledge all the members of the Bakker and Bonn groups that were there over the past years and made life more fun: the Bakker people Yves, Adriaan, Rutger, Lukasz, Jocelyn, Christian P., Christian W., Nuria, Ellen, Sietse, Janneke, Johannes, Liyuan and Stephan; and the Bonn groupies Avi, Maria, Sjors, Ronald, Joep, Susumu, Jens, Gianluca, Katrin, Kramer, James, Maaïke, Ruben, Steven, Søren, Simon, Enrique, Marc-Jan, Cho-Shuen, Zheng, Puck, Jan, ... Thanks and I wish you all the best in the future!

During my thesis work in the Quantum Transport group in Delft, I got a taste of what it would be like to work in science. I would like to thank the people there for showing me their enthusiasm and joy, in particular Frank, Christo, Tristan, Lieven, Katja, Leo, Laurens, Ivo and Floris.

De wetenschap is ontzettend mooi, maar het leven daarbuiten ook. Voor de nodige ontspanning en afleiding ben ik zeer veel dank verschuldigd aan mijn lieve vriendjes en vriendinnetjes, die allemaal hebben bijgedragen aan mooie momenten, een hoop gezelligheid en af en toe wat brakheid de afgelopen jaren! Thanks also to my friends abroad: I'm sure we will meet again somewhere someday! P. tack för den mysiga tid när vi bodde in Göteborg och i Amsterdam.

Ten slotte wil ik graag mijn ouders en mijn zus bedanken voor hun financiële en emotionele steun, interesse en betrokkenheid, die ik vanaf mijn geboorte heb mogen ontvangen. Dat is altijd een heel belangrijke drijfveer voor mij geweest...

CURRICULUM VITAE

Klaas-Jan Tielrooij was born in Eindhoven on December 1st 1981. He obtained his 'Gymnasium' diploma in 1999 from the Lorentz Casimir Lyceum in Eindhoven. In September 1999, he started his studies of Applied Physics at Delft University of Technology and finished his Master's degree in March 2006. In the meanwhile, he passed the Propaedeutic exam in Business Administration at the Erasmus University Rotterdam. Furthermore, between September 2003 and February 2005, he studied at Chalmers University of Technology in Gothenburg (Sweden), where he obtained his Master's degree in Management of Innovation and Entrepreneurship. For his studies in Delft, he conducted a research project at the Cavendish Laboratory, University of Cambridge (United Kingdom) on the *Morphology of Silicon Nanopillars*. His Master thesis on *Relaxation and Manipulation of Electron Spins in a Lateral Quantum Dot* was supervised by prof. dr. L.M.K. Vandersypen and prof. dr. L.P. Kouwenhoven. In the summer of 2006, he started his Ph.D. research at the FOM institute AMOLF in Amsterdam, as a shared member of the Ultrafast Spectroscopy group of prof. dr. H.J. Bakker and the Biosurface Spectroscopy group of prof. dr. M. Bonn.